8-2018

Atomistic Simulations and Microscopic Experiments to Understand Nanoscale Composition Control

Changeun Kim
Purdue University

ATOMISTIC SIMULATIONS AND MICROSCOPIC EXPERIMENTS TO UNDERSTAND NANOSCALE COMPOSITION CONTROL

A Dissertation

Submitted to the Faculty

of

Purdue University

by

Changeun Kim

In Partial Fulfillment of the

Requirements for the Degree

of

Doctor of Philosophy

August 2018

Purdue University

West Lafayette, Indiana

THE PURDUE UNIVERSITY GRADUATE SCHOOL
STATEMENT OF DISSERTATION APPROVAL

Dr. David F. Bahr, Chair

School of Materials Engineering

Dr. Anter El-Azab

School of Materials Engineering

Dr. Michael D. Sangid

School of Aeronautics and Astronautics

Dr. Alejandro H. Strachan

School of Materials Engineering

Approved by:

Dr. David F. Bahr

Head of the School Graduate Program

To Hyunkyung

ACKNOWLEDGMENTS

I would like to express my gratitude to the great people who made it possible to complete this dissertation. Professor David F. Bahr has been an amazing advisor and a bright inspiration through my Ph.D. research. His knowledgeable comment nudged my research to the right direction, he found the right person to work with, and provided me an wide open access to the cutting-edge experimental tools and competitive supercomputing system of Purdue. I did not have in-depth experimental research experience when I joined his group, but now I can confidently carry on a number of advanced characterizations on challenging materials problem. This great learning experience has been made possible by his endless support. His advices on professional relationship and collaboration will continue to be a guiding light in my career onward.

It is a great honor to have Profs. Michael Sangid, Anter El-Azab, and Alejandro Strachan in my Ph.D. committee. They have been wonderful teachers who have brought my understanding of materials science to a next level through elaborative courseworks and critical advices. Their teaching on numerous topics including materials defect, mathematical modeling, simulations, fundamentals of quantum mechanics and molecular dynamics, will continue to be the great leverages to lift up many challenging problems in materials science research.

I am sincerely thankful for the great colleagues in my research group. It is my pleasure to mention Raheleh's professional help on the nano-indentation testings.

For electron microscopies, I acknowledge the Life Science Microscopy Laboratory led by Dr. Chris Gilpin and his team Laurie Mueller and Robert Seiler. This exceptionally well-maintained laboratory is, I believe, something worth to be a subject of a research paper. Moreover their pedagogy during the popular user training is indeed

brilliant and effective. It is by their training when I learned how to perfect sample insertion to a TEM.

The Summer internships at Lawrence Livermore National Laboratory has been great opportunity to work with and learn from professional scientists working in cutting-edge materials challenge. Special thanks to Dr. Vincenzo Lordi for his encouraging advices, and elaborative review on the MgB_2 study that is accepted to journal publication recently and also included in this dissertation. I really enjoyed a number of productive discussions with Dr. Keith Ray and Nick. I sincerely acknowledge the generous support through the Computational Chemistry and Materials Science (CCMS 2016,2017) institute fellowship, and the director of the program Dr. Eric Schwegler, and yet another thanks to Prof. Bahr for his encouraging comment on my application.

I would like to thank Prof. Jeffrey Youngblood for sharing his electrospinning tools with us, Prof. John Balk and Tyler Maxwell for their amazing help on multilayer sputtering synthesis, Qiang Li, Sichuang Xue, Rosa Diaz and Sunghwan Hwang for their technical advices on TEM operation, Prof. Peilin Liao for her thoughtful comment on density functional theory results, Sam Reeve for his advices on molecular dynamics simulation, and Jameson Root for his hard work on managing so many laboratories of the department and teaching me many useful tools. I must thank Prof. David Johnson for he saved my sample on a Sunday night as I locked myself out of the heat treatment room.

All those amazing learning experiences were ultimately made possible by caring and loving family and friends. My beloved wife Hyunkyung who endured a lot and my son Sean who enjoyed a lot, my mother who used to call me a 'Tree of dream' when I was young, my father who exemplifies the true learner's attitude even at his age, my caring sister and her great family, and my wife's family in Korea who have shared the hope and joy together. They know I truly appreciate their presence, and I acknowledge them with my utmost love and respect.

TABLE OF CONTENTS

Page

LIST OF TABLES

LIST OF FIGURES

Figure Page

Figure Page

Figure Page

Figure Page

ABSTRACT

Kim, C.-E. PhD, Purdue University, August 2018. Atomistic Simulations and Microscopic Experiments to Understand Nanoscale Composition Control . Major Professor: David F. Bahr.

In this dissertation, the possibility of using the quantum mechanics calculation in combination with experimental result is explored, in order to explain experimentally observed phenomena in materials science problems. A series of published works in this theory-experiment combinatory approach will be introduced. The topics include the phase stability of Sb_2O_4, surface instability of MgB_2, the interplay of diffusion and mechanical strengthening effect in multilayer, and latest findings of the syntheses of metallic nano-foams. The theory-experiment combinatory approach has proven to be useful in various materials science problems. The phase transformation trajectory of the Sb_2O_4 polymorphs, the surface reconstruction pathways of $MgB_2(0001)$, and diffusion kinetics of Cr-Cu dilute alloy system are calculated by the density functional theory coupled with the nudged elastic band method. Finally, the syntheses of Cu and Cu-Ni alloy nano-foams are reported, detailing their microstructure and morphology characterized by electron microscopies. The potential application of the theory-experiment combinatory approaches in the nano-foam synthesis is further discussed toward better understanding of the structure-property relations of the metallic nano-foams.

1. INTRODUCTION

The dissertation is a collection of my Ph.D. research for the last three years. An overarching theme is to acquire microscopic understanding of materials, using both experimental and theoretical tools. The idea of this combinatory approach, to use both state-of-art experiments along with quantum mechanics calculation is originally inspired by the Nobel laureate Dr. Martin Karplus in 2013, quote "Experimentalists use simulations as a tool like any other" from his lecture.

I chose the density functional theory (DFT) as a primary tool to support my experimental study as well as to analyze other experimental reports. The DFT has been recognized as a great tool for materials research, being a first-principles calculation that does not necessitate adjustable parameters, it finds a great use in predicting property of materials based on the atomic structure of the materials without empirical fitting parameters. The dissertation has complete DFT studies on bulk phases (chapter 2), surfaces (chapter 3), and diffusion of defect (chapter 4), in addition to my experimental studies on synthesis of metallic nano-foams. The former two chapters demonstrate how the DFT calculations can provide useful information of the energy and electronic structure, answering some critical questions that are not completely understood based on the reported experimental observations. In chapter 4, I used the DFT calculations to support my own experimental observation. A great benefit of using DFT in one's own experimental study is the fact that I understand the critical questions that will benefit from theoretical calculations in the first place. Ideally, one can design an experiment in which the corresponding theoretical calculations can make more convincing analyses. Likewise, one can design the theoretical modeling such that the the analysis can be more relevant to the experimental considerations. The last two chapters 5 and 6 report the latest experimental progress on the syntheses of metallic nano-foams.

The chapter 2 investigates the phase stability of the antimony tetroxide polymorphs. The orthorhombic phase α-Sb_2O_4 has been known to be the stable form of the antimony tetroxide. However, a credible experimental measurement from other research group showed that monoclinic β-Sb_2O_4 phase is considerably stable, exhibiting an irreversible transformation from the orthorhombic phase. The determination of the stable phase of material has a greater fundamental interest in materials science. Also, the theoretical understanding of the removal of Jahn-Teller distortion and the origin of irreversible transformation have a widely applicable implication for other mixed oxide materials. In the previous study, a classic rule suggested by Keve and Skapski suggests the monoclinic phase should be considered the stable phase, based on the lower spacegroup symmetry. However, the DFT calculation of the chemical bonding structure has shown that the electronic structure of the orthorhombic phase, actually can be less symmetric than that of the monoclinic phase Sb_2O_4. In addition, the transition state calculations show the irreversibility of monoclinic transformation maybe due to kinetic origins, based on the calculated transition state energy. Finally, the origin of the removal of octahedral distortion of the orthorhombic phase is discussed based on the electronic structure of antimony oxides and chalcogenides. What is clear here is that we can access the ground state electronic structure of materials using DFT, which in turn provide new idea of the mechanisms, chemical bondings, and phase stability problems to work in parallel with experimental observations.

The chapter 3 presents a theoretical study on MgB_2 surface. MgB_2 is an interesting binary superconductor. It has a complex chemical structure due to ionic inter-plane bonding and covalent/metallic mixed in-plane bonding, being known to have a complex Fermi surface. The asymmetric coupling between the electronic structure and phonon mode is known to be responsible for the relatively high superconductor transition temperature. The structure-property relation of MgB_2 has drawn much attention and the bulk property of MgB_2 is well understood, however, the surfaces of MgB_2 are known for difficulties in obtaining consistent characterization. For this case, having theoretical prediction of ideal surface model or representative structure of non-ideal

surface can be useful for identifying the role of different variables that may create the discrepancy. It turns out, a considerable instability of the MgB_2 surface is predicted upon oxygen adsorption. A diverse range of theoretical tools, including crystalline symmetry reduction, surface potential energy mapping, nudged elastic band, hybrid functional method, and *ab-initio* molecular dynamics, are employed to identify and characterize the surface instability of MgB_2.

In chapter 4, I applied DFT calculations for my own experimental study. From experimental result I found the mechanical property of metallic multilayer showed an interesting modulation with respect to the heat treatment temperature. The nanoscale multilayer sample annealed at T=100°C showed decreased mechanical strength, however, another sample annealed at T=300°C showed significant increase of the strength. These strikingly different response may be related to the precipitation of the dilute Cr solute in the Cu matrix. It can be challenging to experimentally compare the diffusion mechanism of the dilute Cr solute in Cu matrix versus the Cu diffusion involved in low temperature grain growth process. We can use idealized models to qualitatively compare the diffusion barrier of Cr in Cu matrix versus their self diffusion. Using relatively simple models and standard transition state calculations, it was possible to answer the questions from my experiment. This chapter aims to practice the idea of using 'the simulation as a tool like any other' in an experimental study. Based on the optimistic progress, we moved on to more sophisticated experimental studies, exploring the synthesis of metallic nano-foams.

The chapter 5 and 6 report the syntheses of metallic nano-foams, including the latest progress of the microstructural characterization of the nano-foams using transmission electron microscopy. These chapters show how far an experimental characterization can get complicated. This is where the theory-experiment combinatory approaches are needed to harness more insight on the structure-property relation of the metallic nano-foam. In this dissertation, the experimental progress up to date is presented, offering a number of interesting problem to investigate using theoretical modeling approach in the future.

In the following sections, some important technical considerations related to the theoretical methods used in the dissertation are discussed.

1.1 Modeling materials structure in periodic boundaries

In order to study materials property using density functional theory (DFT), first we need to build a model of the material of interest. In this section, important technical concepts related to the model structures used in the dissertation are discussed.

In a DFT calculation, we solve the electronic system of materials, finding variational solution of the energy and the electronic states. We are interested in the ground state total energy of the system. The mathematical uniqueness and existence of the ground state energy is proved by the Hohenberg-Kohn theorem. We use efficient numerical minimization algorithm (e.g. conjugate gradient method) to find the electronic states that minimized the total energy to a convergence criterion. Although the uniqueness and existence of this variational solution is guaranteed, however, it is not always guaranteed to find a converged solution. That is why it is important to test the convergence variables so that a reproducible variational solution can be obtained. In this context, a useful DFT calculation result for a materials model means the converged total energy and electronic structure of the model structure. In addition to the minimization for the electronic structure, we are interested in the atomic coordinates that gives the lowest possible total energy of the model. In typical DFT calculations for structural analysis, both the electronic minimization and ionic minimization proceed alternatively until the final converged structure and energy are obtained.

An atom in a model used for DFT calculation is described by the spatial coordinates and the atomic potential. The atomic potentials act as an external potential to the electronic density. The occupancies of the electrons at the atomic potentials are varied such that it minimizes the total energy. For example, if an atomic potential of Na $3s$ state overlaps with an atomic potential of Cl $3p$ state, then the valence elec-

tron of Na occupies Cl $3p$ state instead of Na $3s$ state in order to minimize the total energy. This simple example underlines how the interaction between atoms are different in DFT compared to the molecular dynamics (MD). DFT solves the electronic structure, while MD directly solves the atomic structure based on the parameterized functions and additional order parameters. Typically, the atomic potentials in DFT are determined by solving quantum mechanical equations (Kohn-Sham-Dirac equations) with additional corrections. The development of atomic potential is well described by a textbook of Richard Martin. [1] When it comes to using the atomic potentials in materials modeling, the rule of thumb is to maintain consistency for all element in your calculation within a scientific study. Comparing a result from one type of potential to another result from different type of potential has little meaning other than benchmarking those potentials.

Throughout my Ph.D. research, I mainly used the Vienna *ab-initio* simulation package (VASP). The VASP is known for providing a consistent set of atomic potentials over the entire element table. There are many excellent DFT calculation softwares with different types of basis sets and programming language, but basically solving the same theory. For the case of VASP, the periodic boundary conditions are mandated. The combination of planewave basis with the periodic boundary has a great merit in terms of simplifying mathematical derivation and increasing numerical efficiency. The planewave basis naturally fits to the efficient use of Bloch theorem and Fourier transform. Bloch theorem enables to calculate the property of wavefunction of a translated periodic images based on the property of the actual unitcell. The current implementation of DFT can be more efficiently handled when fast Fourier transform is available. The electron density is computed in the real space, and the electron occupancy of the atomic states with respect to the band index (n) and k-points is more efficiently handled in reciprocal space. For this reason, the fast Fourier transform is actively used to improve the numerical efficiency. But there are some drawbacks of using periodic boundaries for example, when modeling surfaces or isolated molecules.

In chapter 3, the surface model of $MgB_2(0001)$ is created by making a slab model that is periodic over the in-plane axes, but should be non-periodic along the z axis. The non-periodic model is created by introducing vacuum spacing above the surface. The length of the vacuum distance is carefully chosen that the fictitious interaction between one surface to the other surface across the periodic boundary of the unitcell is negligible. Too large vacuum distance can significantly increase the size of the charge density array that will consume large memory. When the unitcell is very asymmetric, a charge-sloshing error can deteriorate the stability of the self-consistent cycle. When such technical error is observed, one should manipulate the mixing parameter to stabilize the convergence process, or increase lateral dimension of the unitcell. In order to model a diatomic oxygen molecule whose total energy is needed to calculate the oxygen adsorption energy, the periodicity along all three directions should be effectively discontinued, by introducing enough vacuum distances in all three axes.

When it comes to modeling the surface of multi-component compounds such as $MgB_2(0001)$, it is important to consider the polarity of the surface. When the surface has significant polarization, the Coulombic repulsion between periodic images can be erroneously taken into the total energy result. Such interaction across the vacuum spacing must be removed by using sufficiently large vacuum gap. Another brute-force method is to use the dipole correction developed by Neugebauer and Scheffler. [2] But for instance when calculating high coverage adsorption models, such interaction across lateral periodic boundaries can be used to simulate the high coverage adsorption condition. Occasionally the local chemical composition of the surface Sometimes, the surface chemical composition is manipulated in order to satisfy the charge neutrality, [3] however it is important to fully examine the thermodynamic stability of the manipulated surface among various possible configurations.

In chapter 4, an isolated vacancy in a close packed metal lattice is modeled in order to calculate the diffusion property mediated by vacancy along the shortest diffusion path. The Cu fcc and Cr bcc models are created by calculating the optimized bulk structure. Both the total energy and atomic forces (Hellmann-Feynman force [4, 5])

are minimized to obtain the variational solution. After creating a vacancy, the force-relaxation optimization is carried out again in order to relax the structures around the vacancy, but without allowing any variation of the cell parameters. This constraint is necessary in order to model an isolated vacancy in an ideal, perfect bulk material. Once relaxed the cell parameters in the latter stage of optimization, we no longer look at the isolated vacancy model, but instead a bulk model with singular vacancy concentration is obtained instead.

1.2 The choice of exchange-correlation approximations

The success of DFT is due to mathematically exact mapping of the many-body Schrödinger equation to a uni-body (electron density) Kohn-Sham equation. The exchange-correlation term in the Kohn-Sham equation broadly embraces all the remaining consequences due to the mapping besides all the known terms. There are still active ongoing effort to find the exact or more accurate form of the exchange-correlation term. In this section, I would like to introduce the exchange-correlation approximations used in the present dissertation.

The name "exchange-correlation" implies where the unknown errors originate from. In the electronic density space, an electron is not described as a particulate point, instead, its spatial probability is spread over the space. When iterating over the grid points of the electron density space, any pair-wise calculation can include the interaction between an electron and itself. This is called the self-interaction error. The correlation effect addresses the manybody interaction, however, the other electrons are also spread over the density space. Thus the exchange-correlation term embraces the consequences of mapping many-body discrete electronic system to a continuous electronic density space. Since the exact solution of the exchange-correlation term is still unknown, various approximations has been proposed. When using DFT to study materials it is important to know the merit and limitations of the exchange-correlation approximation used in the calculation.

The simplest approximation is local density approximation (LDA). Since the energy of the ground state ideal electron gas is well defined, [6] the exchange-correlation term can be accurately obtained from the case of ideal electron gas. In LDA, this ideal gas derived exchange-correlation energy is used for a given electron density. The LDA is most useful for a system that is closer to free-electrons system, such as a metallic material. However, LDA is known to poorly describe more electronically localized systems such as molecules and ionic materials.

Recognizing the discrepancy from ideal homogeneous electron gas, the next logical step is to introduce corrections based on the spatial variations of the electron density. When the gradient of electron density is used to further improve accuracy of the calculation, it is called generalized gradient approximation (GGA). [7–9] There are ongoing effort to include the correction due to second derivatives of the electron density, frequently called as meta-GGA (m-GGA).

Next logical step is to address the self-interaction errors. The correction can be introduced by calculating discrete and explicit exchange calculation. When an explicit exact exchange calculation is used along with conventional semi-local (e.g. LDA, GGA), then it is called a hybrid approach. However, performing the exchange calculation over large domain consumes considerable computational resource. Instead, Heyd, Scuseria, and Ernzerhof developed the screened hybrid approach based on the idea that the electron-electron interaction is most significant at a short range, but can be screened in a long range, introducing a screening parameter to the hybrid approach. The use of exact exchange and screening parameters introduced two adjustable parameters. The mixing parameter α determines the fraction of the exact exchange. The screening parameter μ determines the strength of the charge screening effect. However, it is important to avoid an inductive approach to empirically determine the parameters. It was shown that when the $\alpha = 0.25$, the value, slope, and second derivative of using the functional matches to the semi-local cases (i.e. LDA or GGA). [10] The screening parameter μ determines the cutoff range. This parameter was revised once, [11] and was suggested as a material-dependent parameter. [12]

However, to use an arbitrarily adjustable parameter in DFT calculation works against the benefit of using a first-principles approach. We want as little empiricism as possible when it comes to use a first-principles method to predict materials property. One possible solution is suggested to fit μ to achieve the best fit of the electronic band structure to that of the quasi-particle GW calculation. [12] Instead of fitting to an experimental measurement, it still relies on first-principles calculation. This approach, namely HSE(GW) method, is used in chapter 3 along with other types of exchange-correlation functionals. Despite these incredible advances in the various exchange-correlation approximations, it is important to test different types of approximations for the specific problem at hand, comparing to relevant experimental data or result from more advanced theory.

2. UNCOVERING THE THERMO-KINETIC ORIGINS OF PHASE ORDERING IN MIXED-VALENCE ANTIMONY TETROXIDE BY FIRST-PRINCIPLES MODELING

*The contents of this chapter is appeared on the journal Inorganic Chemistry (Kim et al., *Inorg. Chem.* **56**, 6545 (2017))

Phase ordering in the mixed-valence oxide Sb_2O_4 has been examined by density-functional theory (DFT) calculations. We find that the ground state total energies of the two phases (α and β) are almost degenerate, highly sensitive to the choice of the approximation to the exchange correlation (xc) functional used in our calculations. Interestingly, with the inclusion of the zero point energy corrections, the α phase is then consistently the predicted ground state polymorph regardless of the choice of xc functional used. We also illustrate the pronounced stereochemical activity of Sb in these polymorphs of Sb_2O_4, setting an exception to the Keve and Skapski rule. Here, we find that the actual bonding in the α phase is more asymmetric while the anomalous stability of the β phase could be rationalized from kinetic considerations. We find a non-negligible activation barrier for this α–β phase transition, and the presence of saddle point (β phase) supports the separation of Sb(III) over a continuous phase transition, as observed in experiments.

2.1 Introduction

Since the first identification of antimony tetroxide, Sb_2O_4, from a natural mineral [13], two types of its polymorphs, cervantite and clinocervantite have been identified [14]. Cervantite, the orthorhombic α phase ($Pna2_1$) was the first observation of the mixed oxide of antimony, found in Cervantes (Lugo, Spain) in 1845 [13], and clinocervantite, the monoclinic β phase ($C2/c$) was found in Cetinemine (Tuscany,

Italy) in 1964 [15]. In syntheses, the α phase can be obtained by heating antimony trioxide (Sb_2O_3) in air [16,17], indicating it is the ground state of antimony tetroxide, and the β phase can be synthesized by heating the α phase in vacuum (10^{-3} mmHg) followed by rapid quenching [14], or heating the α phase under high pressure at an elevated temperature [18]. Interestingly, once the β phase is formed, it rarely transforms back to the α phase [18]. Some previous studies have offered explanations for the origin of the "abnormal stability" of the β phase [18, 19] and even suggested that the α phase may be a metastable modification of the β phase. Orosel and coworkers determined the pressure-temperature phase diagram of these mixed states experimentally [18].

Keve and Skapski [19] provided a basis for explaining the stability of the β phase in terms of the crystalline symmetry. The basic idea is, for mixed oxides with $A^{III}B^{V}O_4$, the centrosymmetric β phase has a lower crystal symmetry (compared to the orthorhombic α phase), and this phase can always be stable (where A = Sb or Bi, and B = Nb, Sb or Ta). This rule has been used to explain the abnormal stability of the β phase [18]. Indeed the β phase of antimony tetroxide has a higher packing density and is seemingly more stable than the α phase according to the previous study. This idea may explain the unexpected stability of the β phase, however, this rule alone does not explain why the α phase can be comparably stable.

Indeed, antimony tetroxide is not a simple material. Antimony, an element with five valence electrons, can have either a (nominally) +3 oxidation state as in Sb_2O_3, or +5 as in Sb_2O_5. In the mixed state, Sb_2O_4, there is an equal proportion of +3 and +5 oxidation states of antimony. Thus, antimony tetroxides are found to exhibit complex behavior, primarily due to stereochemical activity of Sb, as indicated by the presence of lone-pair electrons [20]. Various physical properties of the other polymorphs of tri-, and penta-oxides are discussed in detail elsewhere [20, 21].

It is evident that a clear atomistic understanding of the phase transition between the α and β phases, and the associated irreversibility is still lacking and calls for an investigation into the kinetics of the phase transition, in addition to thermodynamic

considerations. In the present paper, using first-principles density-functional theory calculations, we thus investigate the relative stabilities of these two phases, as well as the energetics and kinetics of the atomic phase transition between them in an attempt to rationalize the competing structural and electronic origins of the unresolved phase ordering in Sb_2O_4. In addition to predicting which phase is the ground state, our findings challenge the current understanding of the structure-property relation in these materials and may also provide useful insights into understanding the phase stability of other such complex (mixed) heavy metal oxides [20, 22, 23].

2.2 Methodology

We perform density functional theory (DFT) calculations as implemented in the Vienna *ab-initio* simulation package (VASP) [24,25]. The kinetic energy cutoff for the planewave basis set is 500 eV and the electron-ion interactions are represented using the projector augmented wave (PAW) potentials [26, 27]. The crystalline structures of the polymorphs of Sb_2O_4 are calculated using various exchange-correlation (xc) functionals and compared to experimental results. The HSE06 [28–31], PBE [32], RPA@PBE [33, 34], PBE-D2 [35], PBEsol [36], and LDA [37] functionals are considered in this study. The RPA@PBE method by Kresse and coworkers, has been shown to improve total energies for both surfaces as well as bulk materials [33]. This method takes the optimized geometry at the PBE level, followed by self-consistent calculations with the random phase approximation (RPA).

For the PBE, PBE-D2, PBEsol, and LDA calculations in the present work, a Monkhorst-Pack [38] k-point grid of $8 \times 8 \times 4$ is used for geometric optimization of α–Sb_2O_4, and $4 \times 8 \times 8$ is used for β–Sb_2O_4. For the HSE06 and RPA@PBE calculations, $4 \times 4 \times 2$ and $2 \times 4 \times 4$ k-point grids are used for α–Sb_2O_4 and β–Sb_2O_4, respectively. For HSE06 density-of-states calculations, a slightly denser Γ-centered grid of $6 \times 6 \times 3$ is used for α–Sb_2O_4, and $3 \times 6 \times 6$ is used for β–Sb_2O_4.

For the reference states (rhombohedral Sb and O_2 molecule), a Monkhorst-Pack type $9 \times 9 \times 3$ grid was used for Sb, and a Γ-centered single point was used for O_2 with a $20 \times 20 \times 20\,\text{Å}^3$ supercell. The zero point energy (ZPE) corrections are calculated by density-functional perturbation theory (DFPT) [39–41], except for PBE-D2 and PBE-D3. The finite difference method is used for PBE-D2 and PBE-D3, instead. The total energy convergence criterion is $10^{-5}\,\text{eV}$ for self-consistent electronic minimization steps, and $10^{-4}\,\text{eV}$ for ionic displacement steps.

We calculate the formation energy (E_f) using the aforementioned various *xc*, as,

$$E_\text{f} = E^\text{tot}_{\text{Sb}_2\text{O}_4} - n_\text{Sb} E^\text{tot}_\text{Sb} - \frac{n_\text{O}}{2} E^\text{tot}_{\text{O}_2} \quad , \tag{2.1}$$

where $E^\text{tot}_{\text{Sb}_2\text{O}_4}$ denotes the ground state total energy of Sb_2O_4 of respective bulk phase (per formula unit), n_Sb the number of Sb in the bulk unit cell, E^tot_Sb the total energy of a Sb atom in the reference state Sb bulk, n_O the number of oxygen ions in the bulk Sb_2O_4 unit cell, and $E^\text{tot}_{\text{O}_2}$ the total energy of the oxygen molecule.

To investigate the differences between the atomic and electronic properties of the two phases, we first introduce a structural analyses taking non-local neighboring oxygen ions of Sb(III) into account, which confirms the idea suggested by Amador *et al.* in 1988 [14]. We calculate the radial distribution function (RDF) and bonding angle distribution (BAD) to discuss the structural differences between the two phases of antimony tetroxides [20, 42]. In these analyses the Sb(III) and Sb(V) atoms are treated as separated species.

Next, we perform electron localization function (ELF) calculations to explicitly define the chemical bonding between Sb(III) and the non-local neighboring oxygens [43]. ELF provides a non-empirical basis for the identification of chemical bonds. In order to obtain a quantitative comparison, we have projected the volumetric ELF data to a linear bonding path that directly connects the Sb ion to a neighboring oxygen by shortest distance, highlighting the different bonding natures around Sb(III) between the α and the β phases.

To evaluate the energy barrier for the phase transition between the α and the β phases, we have performed the climbing image nudged-elastic band method (CI-NEB)

using the PBE xc functional. The calculations are performed in two steps. Firstly as an initial guess, nine atomistic structures are modeled by interpolating the atomic positions as well as the translation vectors of the two phases. Next, we take the saddle point structure and perform a geometry optimization. Now, the two separate CI-NEB calculations are then performed using the optimized saddle point structure as the constraint image in the middle of the pathway. The three optimized structures (α phase, optimized saddle point structure, and β phase atomic geometries) are now used as constrained images, and two separate CI-NEB calculations for both half paths are then performed (from the α phase to the saddle point, and from the saddle point to the β phase). We note that the consequences due to grain boundaries or surfaces are not taken into account, making the interpretation of the result relevant to only single crystalline Sb_2O_4.

2.3 Results and discussion

2.3.1 Structures and energies of Sb_2O_4

Table 2.1.
Bulk parameters of the calculated atomic structures of α–Sb_2O_4, using various exchange-correlation (xc) functionals. The theoretical results are compared to experiment data [44]. Percentage differences are shown in parentheses (in %).

xc	a (Å)	b (Å)	c (Å)
HSE06	5.44 (−0.2)	4.83 (+0.4)	11.79 (+0.1)
PBE	5.56 (+1.9)	4.90 (+2.0)	11.94 (+1.4)
PBEsol	5.47 (+0.3)	4.84 (+0.6)	11.77 (−0.1)
PBE-D2	5.49 (+0.8)	4.86 (+1.1)	11.86 (+0.7)
LDA	5.41 (−0.7)	4.80 (−0.3)	11.67 (−1.0)

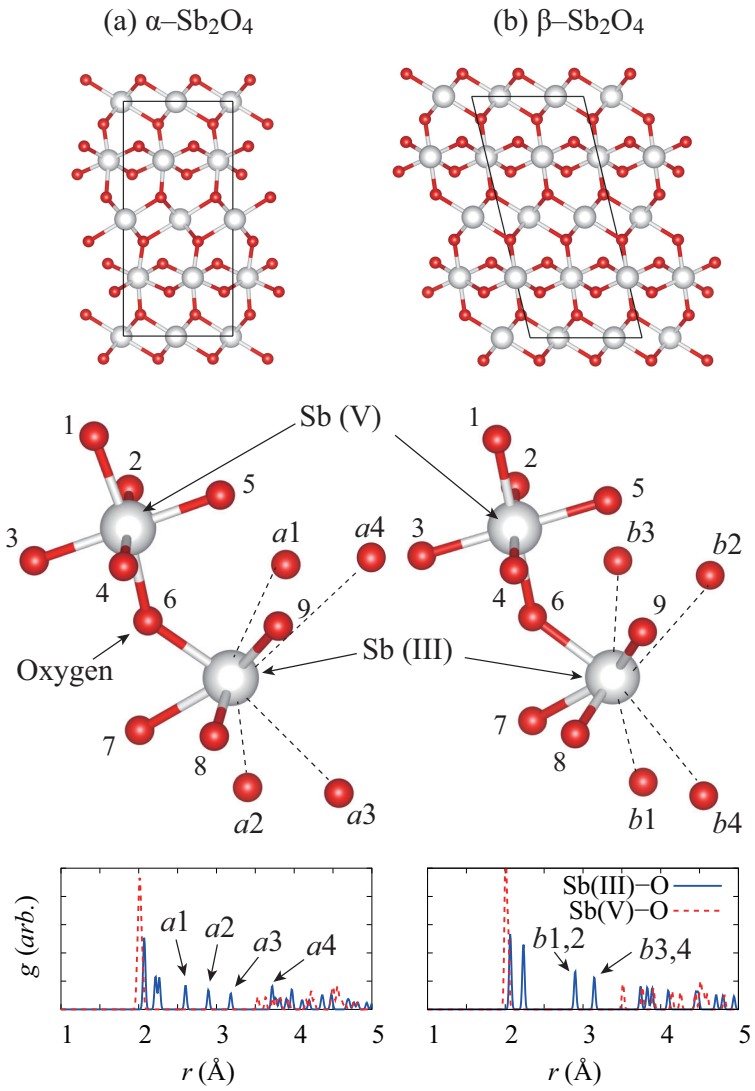

Fig. 2.1. Optimized atomic structures of (a) α–Sb_2O_4 and (b) β–Sb_2O_4. The α–Sb_2O_4 phase has an orthorhombic crystalline unit cell, while the β–Sb_2O_4 phase has a monoclinic unit cell. Antimony with different oxidation states – Sb(V) for Sb^{5+} and Sb(III) for Sb^{3+}, comprise the repetitive structural units. A distinct difference between the two phases comes from non-local Sb–O bonding around Sb(III). The difference is clearly captured by the radial distribution function (RDF), given below in the lower panels of the figure.

The calculated structural parameters of α–Sb_2O_4 and β–Sb_2O_4 phases are listed in Tables 2.1 and 2.2. α–Sb_2O_4 has an orthorhombic structure, while β–Sb_2O_4 crys-

Table 2.2.
Bulk parameters of the calculated atomic structures of β–Sb_2O_4, using various exchange-correlation (xc) functionals. The theoretical results are compared to experiment data [45]. Percentage differences are shown in parentheses (in %).

xc	a (Å)	b (Å)	c (Å)	β (°)
HSE06	12.06 (−0.0)	4.85 (+0.4)	5.39 (+0.3)	103.9 (−0.7)
PBE	12.20 (+1.2)	4.93 (+2.0)	5.51 (+2.4)	103.7 (−0.9)
PBEsol	12.05 (−0.1)	4.87 (+0.9)	5.39 (+0.2)	105.0 (+0.4)
PBE-D2	12.20 (+1.2)	4.91 (+1.6)	5.41 (+0.5)	105.7 (+1.0)
LDA	11.94 (−1.0)	4.84 (+0.2)	5.33 (−1.0)	105.7 (+1.0)

talizes in a monoclinic structure. Despite the difference in unit cell symmetry, the atomic arrangements of these two phases are rather similar (see Figure 2.1). Due to this structural similarity, we propose that the atomic structure of α–Sb_2O_4 may be transformed to that of β–Sb_2O_4 by merely a shear deformation in the $a-b$ plane, with the longest c axis of the orthorhombic α phase now acting as the a axis of the monoclinic β phase.

The formation energies, E_f of both phases are given in Table 2.3. The E_f of the α and the β phases are so close that the differences, ΔE_f are only a couple of meV per formula unit. Therefore, it could be expected that a small correction to the formation energies (e.g. by taking the weak van der Waals force interaction as included in PBE-D2) may reverse the ordering. Allen *et al.* [21] reported the formation energy of α–Sb_2O_4 and β–Sb_2O_4 to be −8.31 and −8.30 eV, respectively, and is in close agreement with the present work.

The zero point energy (ZPE) corrections are calculated for the two phases with respect to various xc functionals (in Table 2.3). The ZPE results show that the

Table 2.3.
Calculated formation energy, E_f (and selected zero point energy, E_{ZPE} in brackets) of the α and β phases of Sb_2O_4, using various exchange-correlation (xc) functionals. Here, ΔE_f and ΔE_{ZPE} are calculated by subtracting the corresponding E_f and E_{ZPE} of the β phase from that of the α phase, respectively. Here, a negative ΔE_f value will indicate that the α phase is more thermodynamically stable that its β form. The energies are expressed in eV/formula unit.

xc	α–Sb_2O_4, E_f (E_{ZPE})	β–Sb_2O_4, E_f (E_{ZPE})	ΔE_f	ΔE_{ZPE}
RPA@PBE	−10.445	−10.434	−0.011	–
HSE06	−8.452	−8.449	−0.003	–
PBE	−8.275 (0.776)	−8.263 (0.782)	−0.012	−0.006
PBEsol	−8.939 (0.803)	−8.940 (0.813)	+0.001	−0.010
PBE-D2	−8.892 (0.759)	−8.914 (0.765)	+0.022	−0.006
LDA	−10.565 (0.828)	−10.578 (0.834)	+0.012	−0.006

contribution to the formation energy differences between the α and β phase is about 6 to 10 meV/formula unit, favouring the α phase.

Using the RPA@PBE approach [33, 34], in which many-body perturbation theory at the random phase approximation level is used to correct bulk energies [34], we find that the RPA@PBE also favors the α phase by 11 meV/formula unit (without ZPE corrections).

However, such small energy differences may well indicate that conclusions cannot be drawn purely based on total energies. These results, nevertheless, suggest that the two polymorphs of Sb_2O_4 could be a pair of useful candidates for benchmarking the accuracy of common xc approximations used for solid-state calculations.

Taking a closer look at the structural factors in these two phases of Sb_2O_4, we find that the actual interatomic bondings in the α phase are less symmetric, with a notable octahedral distortion of Sb(V) as well as the asymmetric interactions around

Sb(III). As the β phase is stabilized by the lower structural symmetry of the unit cell, the α phase, on the other hand, has less symmetric interatomic bonding arising from its unique electronic structure (as detailed below).

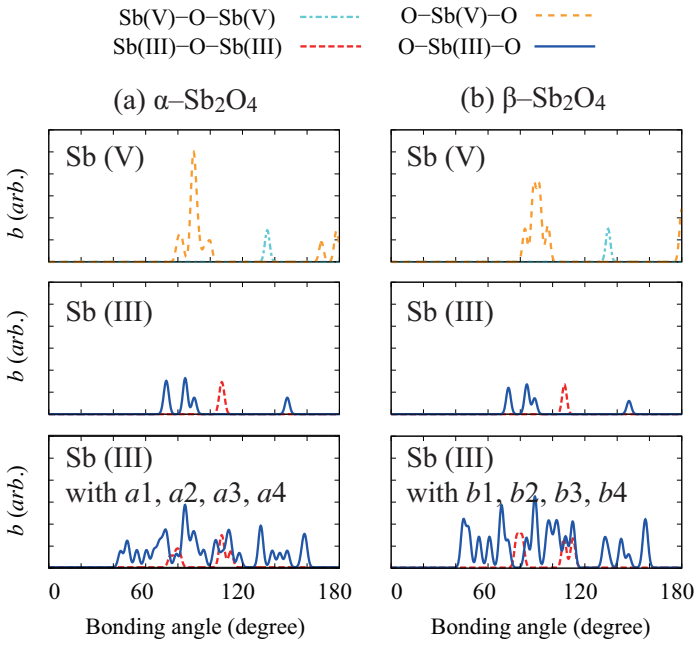

Fig. 2.2. (Color online) Calculated bond angle distribution for (a) α–Sb_2O_4 and (b) β–Sb_2O_4. Bond angles of Sb–O–Sb and O–Sb–O are separately calculated for Sb(III) and Sb(V). Note that the α–Sb_2O_4 phase has a distorted octahedral arrangement around Sb(V). The two phases do not show clear differences when only local neighbor oxygens are considered, however, a drastic difference can be seen when non-local neighbors ($a1$, $a2$, $a3$, $a4$, $b1$, $b2$, $b3$, and $b4$) are included in the calculation. See Figure 2.1 of the main text for the assignment of these labels used in the bond angle distribution.

The α phase exhibits a Jahn-Teller distortion of the octahedral coordinations around Sb(V). A Jahn-Teller distortion occurs when a distorted structure is favored over an ideal coordination due to the asymmetric electronic structure of the system [46]. From the structural differences, we can already see that there may be a pronounced role of the lone-pair electrons of Sb in both the octahedral distortion around Sb(V), as well as in the non-local bondings around Sb(III). The octahedral distortion is captured in bonding angle distribution (BAD) shown in Figure 2.2. The

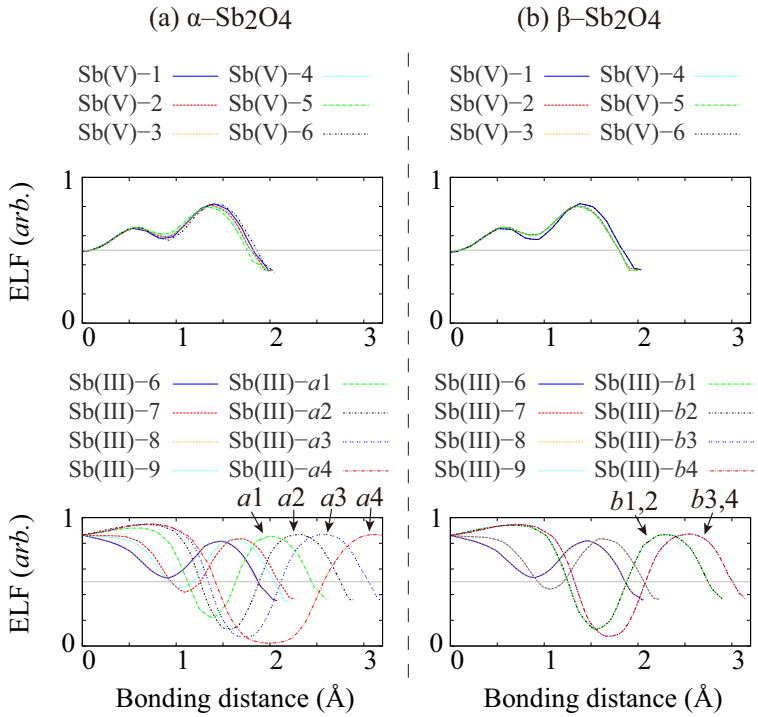

Fig. 2.3. Electron localization function (ELF) projected along the bonding path between Sb and O atoms for (a) α–Sb_2O_4 and (b) β–Sb_2O_4. The ELF spans from 0 to 1, where 1 denotes maximum localization of the electronic density, and the value of 0.5 (gray horizontal lines) represents an approximate covalent nature of the bonding. The ELFs projected between Sb(III) ions and its local (O6, O7, O8, and O9) and non-local ($a1$, $a2$, $a3$, $a4$, $b1$, $b2$, $b3$, and $b4$) oxygen neighbors show different bonding characteristics. See Figure 2.1 for the assignment of these labels used for the ELF projections.

O–Sb(V)–O is significantly distorted from 180° in the α phase, compared to that of β phase.

2.3.2 Electronic structure of Sb_2O_4

We next proceed to study the electronic structure of these two phases of Sb_2O_4 via the electron localization function (ELF), projected density-of-states (pDOS), and Bader charge analysis. The electron localization function (ELF) ranges from 0 to 1, where a value of 0.5 corresponds to covalent bonding. This analysis gives a non-

empirical characterization of the bonding nature based on calculated electronic density.

With the ELF analysis, we find there are non-local bondings between Sb(III) and neighboring oxygen ions. It is unusual to find Sb–O bondings extending to about 3 Å (see Figures 2.1 and 2.3). This indicates there are significant stereochemical interactions between lone-pair electrons of Sb and O. The ELF curves in Figure 2.3 clearly show that there are still significant chemical bonding at these distances.

In fact, this has been suggested by Amador *et al.* in 1988 [14]. Based on the empirical bond-valence model, the authors calculated the oxidation number of Sb(III). Without taking the non-local oxygen neighbors into account, the bond valence of Sb(III) was only 2.5, not reaching to an ideal oxidation state of 3.0. Only by considering two more of the non-local oxygen neighbors, they found 2.9. Yet this empirical calculation did not address the difference between the α and β phases. In our ELF result, a pronounced asymmetry in Sb(III)-O bondings can be observed (Figure 2.1). We notice the bonding around the Sb(III) atom of the α phase are asymmetric, while those of the β phase are degenerate in a pairwise manner.

With regards to phase stability, this observation raises a question about a previous idea based on the rule of Keve and Skapski [18, 19]. Although the centrosymmetric β phase has a lower crystal lattice symmetry, the electronic structure and the interatomic bonding are the opposite. These two different competing scenarios – low lattice symmetry of the monoclinic β phase versus the actual asymmetry of the interatomic bondings in the α phase, complicate the problem significantly.

A study of the structural evolution of antimony chalcogenides by Carey *et al.* have shown that the local coordination around Sb(V) can be significantly manipulated by the electronic property of anions [47]. In the cited work, a series of antimony chalcogenides: oxide, sulfide, and telluride were studied, which suggested that the energy level of the anion valence state has a strong correlation with the distorted structures around Sb. Those anions, O, S, Te have different valence state energies,

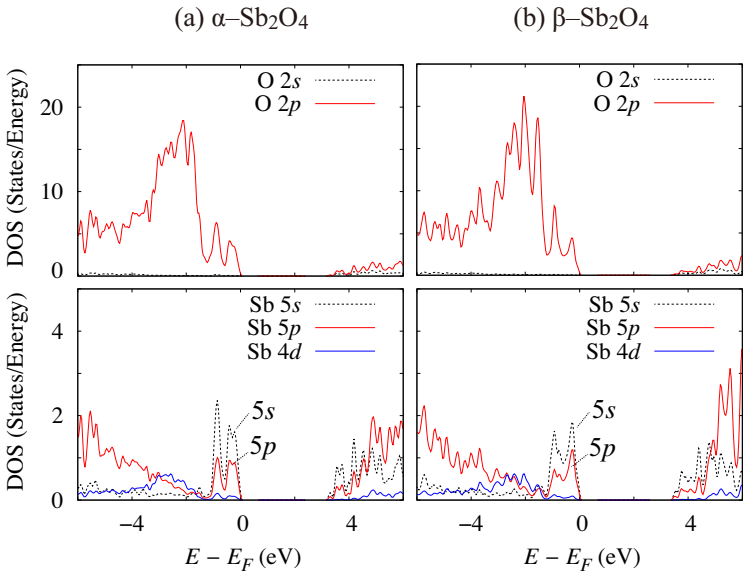

Fig. 2.4. Calculated electronic projected density-of-states with the HSE06 *xc* functional for (a) α–Sb_2O_4 and (b) β–Sb_2O_4. The electronic structure of α–Sb_2O_4 exhibit separate peaks in the vicinity of the Fermi level, indicating the more asymmetric bonding structure of the α phase. Here, the top of the valence band is set to 0 eV.

with O the lowest and Te the highest. The lone-pair electrons can be stabilized when the energy levels of anion p orbitals, Sb $5s$, and Sb $5p$ states are in a delicate balance.

The significant change from the distorted octahedral coordination in the α phase to a perfect octahedral in the β phase can be rationalized by considering the up-shifting in the energy of valence electrons of the O anions during the transformation process (under elevated temperatures and under high pressures). Here, the more energetic valence electrons in the O anions then play a similar role to that in the electron-rich anions in antimony chalcogenides [47].

Some agreement may be drawn from the pDOS shown in Figure 2.4, as calculated using the HSE06 *xc* functional. The oxygen pDOS of the β phase captures this removal of the asymmetric bonding structure in the α phase by presenting slightly more broadened peaks near the valence band maximum, while the merging of the Sb $5s/5p$ peaks lends support to a more symmetric bonding in the β phase. The elevated

energy states of O $2p$ in β phase coincides with the trend found in Carey *et al.* where the energy levels of the anions are found to close correlate with the stabilization of octahedral arrangement around Sb in the chalcogenide series.

In addition, we use Bader charge analysis to quantify the differences in the anionic property of the two phases. Bader charge analysis calculates the electronic density allocated to adjacent ions based on charge-flux neutrality. It is found that there are small but non-negligible changes to the electronic charges in the oxygen anions, where the oxygen anions in the β phase are indeed more negatively charged than those in the α phase and suggesting that the molecular orbital energy levels of the the β phase may then be higher that those of the α phase.

2.3.3 α–β phase transformation in Sb_2O_4

We now proceed to examine and discuss the irreversibility of the phase transition reported in experiments. Orosel and coworkers [18], carefully surveyed the stability of antimony tetroxide spanning through a range of temperatures and pressures. A list of important findings are summarized here: (i) Starting from pure α–Sb_2O_4, it smoothly transforms to β–Sb_2O_4 under elevated temperature (375 °C) and high pressure (6 GPa); (ii) At ambient temperature (23 °C), the α phase transform to the β phase when the pressure reaches as high as 20 GPa; (iii) The high purity β phase is stable within a narrow range of temperatures ($350\,^{\circ}\mathrm{C} < T < 400\,^{\circ}\mathrm{C}$); (iv) Upon removing the external pressure and heating, the β phase **does not** transform back to the α phase. If the β phase was truly a metastable phase, the reverse reaction should have proceeded when the external driving forces (i.e. the heating and pressure) were removed. However, the β phase remained unchanged even upon providing thermal energy in an attempt to overcome the activation energy barrier. Surprisingly, the material rather decomposes into Sb_2O_3, which we believe, raises an interesting point of discussion.

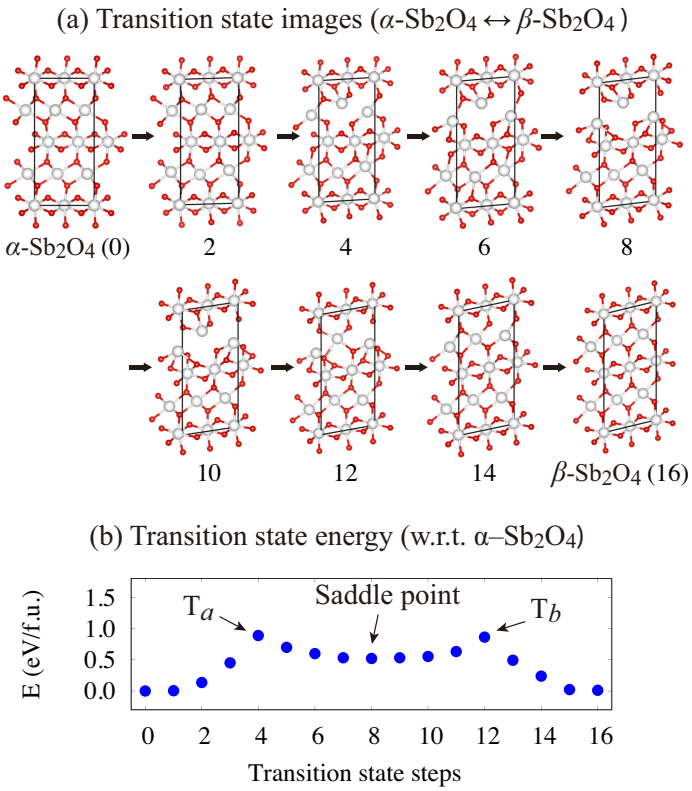

Fig. 2.5. (a) Transition state images and (b) the associated energy differences calculated by the climbing image nudged elastic band (CI-NEB) method. The initial atomic structures are approximated by taking the shortest translation path between ions in α–Sb_2O_4 and their counterparts in β–Sb_2O_4. The CI-NEB finds a saddle point amidst the direct transformation.

The irreversible transformation to the β phase has been the crucial evidence of the stability of the β phase. The abnormal stability of this high temperature phase has been explained by the rule of Keve and Skapski [18,19]. Though the centrosymmetric β phase can have the lower symmetry on the crystalline lattice level, the electronic structure and the interatomic chemical bonding support the opposite. Our ELF results (as discussed above) clearly demonstrate that the actual interatomic chemical bonding can be more asymmetric in the α phase. These competing structural origins on different scales complicate the problem significantly.

Besides arguing from an electronic structure point-of-view, we speculate that the β phase may, in fact, be further stabilized by kinetic origins. As a starting point, we performed a series of climbing image nudged elastic band (CI-NEB) calculations (in Figure 2.5). Taking the advantage of the structural similarity in the two phases, we correlate each ionic position in both phases that requires the smallest displacement. In this way, we attempt to find the lowest energy barrier for the most probable phase transition pathway. In order for the α phase to smoothly transform to the β phase, the layer consisting of Sb(V) and in-plane O ions should be shifted along the a–b plane. This intuitively favours and involves the rearrangement of the minimal number of Sb-O bonds.

The transition barrier energy is found to be 0.9 eV/formula unit at the highest point. This high energy barrier is associated with the shear deformation along the a–b plane, and the corresponding rearrangement of O ions. The calculated saddle point trajectory shows a prevailing instability during the phase transformation, where the separation of Sb(III) is preferred over the breaking and (re)formation of Sb-O bonds. This coincides with the observed decomposition of the β phase into Sb_2O_3 in the previous work [18].

2.4 Summary and conclusions

In perspective, while some of the most advanced DFT (and many-body physics) approximations used in this work favor the thermodynamic stability of the α phase (see Table 2.3), this alone does not explain the unusual stability of the β phase. The peculiar stability of the β phase can indeed be rationalized from kinetic considerations, supported by our calculated transition barrier of as high as 0.9 eV/formula unit. We also argue that the initial transformation may be triggered by a change in the oxygen electronic orbital energy levels during the process, which involves the removal of the Jahn-Teller distortion in the α phase, in analogy to the structural evolution of the antimony chalcogenides series.

3. ELECTRONIC STRUCTURE AND SURFACE PROPERTIES OF MAGNESIUM DIBORIDE UPON OXYGEN ADSORPTION

*The contents of this chapter is featured on the journal Physical Review B (Kim et al., *Phys. Rev. B* **97**, 195416 (2018))

We use density-functional theory to investigate the bulk and surface properties of MgB_2. The unique bonding structure of MgB_2 is investigated by Bader's atoms-in-molecules, charge density difference, and occupancy projected band structure analyses. Oxygen adsorption on the charge-depleted surfaces of MgB_2 is studied by a surface potential energy mapping method, reporting a complete map including low-symmetry binding sites. The B-terminated $MgB_2(0001)$ demonstrates reconstruction of the graphene-like B layer and the reconstructed geometry exposes a three-fold site of the sub-surface Mg, making it accessible from the surface. Detailed reconstruction mechanisms are studied by simulated annealing method based on *ab-initio* molecular dynamics and nudged elastic band calculations. The surface clustering of B atoms significantly modifies the B $2p$ states to occupy low energy valence states. The present work emphasizes that a thorough understanding of the surface phase may explain an apparent inconsistency in the experimental surface characterization of MgB_2. Furthermore, these results suggest that the surface passivation can be an important technical challenge when it comes to development of a superconducting device using MgB_2.

3.1 Introduction

MgB_2 is an interesting superconductor with high T_c, [48, 49] in which a two-gap superconductivity originates from its anisotropic bonding structure. MgB_2 has

an AlB_2 type crystal structure, where close packed Mg layers and graphene-like B layers alternate along the c axis of the hexagonal unit cell. MgB_2 shows a complex bonding structure consisting of ionic inter-layer bonding and covalent/metallic mixed in-plane bonding. The B and Mg are stabilized in the layered structure by ionic charge transfer: B in MgB_2 exhibits a graphene-like hexagonal layer, while bulk B is stable in a rhombohedral phase; [50] also, the Mg–Mg distance within the Mg layer of MgB_2 is considerably smaller than that of bulk Mg. Mg transfers most of its valence electrons to B layers, filling B $2p_z$ orbitals while reducing the Mg–Mg bonding distances due to the emptying of the outer shell. The surface of this binary compound can exhibit unique properties and structures, since this fundamental interlayer charge transfer mechanism that stabilizes the layers in bulk MgB_2 does not persist at the surface.

MgB_2 has displayed a uniquely disordered superconducting vortex structure. [51] To fully understand the observed disorder, it is important to address any potential surface phases in order to credibly attribute the observation to a bulk property of MgB_2. MgB_2 is also known for difficulties in obtaining consistent surface-sensitive spectra from scanning tunneling spectroscopy and Auger methods. [52–55] It is suggested that an unstable surface construction could be a reason for such measurement inconsistencies. [48, 56, 57] As bulk properties are further studied, it is equally important to work toward a better understanding of the surface, which often stands between the physical probe and the bulk domain of interest. [56]

A frequently observed impurity in MgB_2 is oxygen, and the surfaces and grain boundaries of MgB_2 are commonly under the influence of oxygen impurities in one form or another. [58, 59] $MgB_2(0001)$ is a stable low-energy facet occurring in crystalline MgB_2 synthesis, [60] which experimentally exhibits trace oxygen despite vacuum conditions encountered during the pre-synthesis stage. To better understand the MgB_2 surface and further investigate any possible surface reconstructions, we consider B- and Mg-terminated MgB_2 surfaces in both the pristine case and under the influence of adsorbed oxygen. A stable low-energy surface orientation is more thermodynamically probable and experimentally relevant, [60] therefore, we focus on the

$MgB_2(0001)$ surface as a first step. Interestingly, calculations show the Mg-terminated $MgB_2(0001)$ is more thermodynamically stable in terms of surface energy, [61] but experimental studies reported in several cases that boron-rich surface phase is observed in MgB_2, as well. [52,62,63] The present work explores a possible reconstruction pathway of the B-terminated surface triggered by surface-adsorbate interaction, causing formation of complex surface oxide phase.

We begin with the electronic structure of the bulk, explain how the unique layered structure is stabilized, and show that the electrophilic B-terminated surface suffers a spontaneous reconstruction under the influence of adsorbed oxygen. The calculated ionicity of bulk MgB_2 coincides with a previous study based on Phillips-van Vechten-Levine (PVL) dielectric theory, [64] where 96.8% ionicity of Mg–B bonding was reported. We compute the oxygen adsorption potential energy surface map for both Mg- and B-terminated surfaces of $MgB_2(0001)$ and further detail their electronic structures as well as oxygen diffusion transition state geometries. Simulated annealing based on *ab-initio* molecular dynamics (*ai*MD) is used to explore a possible reconstruction pathway in the vicinity of the adsorbed oxygen. Based on the simulated annealing, we develop a two-step reconstruction model of B-terminated $MgB_2(0001)$ with adsorbed oxygen and calculate the transition state energy barriers.

The results raise an interesting question of whether the surface of MgB_2 retains its high T_c superconductivity. The high-T_c property of MgB_2 is known to originate from strong electron-phonon coupling, where in-plane $2p_{x,y}$ orbitals strongly couple to the in-plane E_{2g} phonon modes. [65, 66] However, the present work shows that the E_{2g} mode does not exist in a reconstructed boron layer. Thus, the consequences of surface oxidation of MgB_2 can be more fundamental in destroying the superconductivity than mere dielectric formation.

3.2 Methodology

We perform density-functional theory calculations [67] using the Vienna *ab-initio* simulation package (VASP). [68, 69] The kinetic energy cutoff for the planewave basis set is 500 eV and the electron-ion interactions are represented using the projector augmented wave (PAW) potentials. [70, 71] The total energy convergence criterion is 10^{-5} eV for electronic minimization steps, and 10^{-4} eV for ionic displacement steps, which result in convergence of the Hellmann-Feynman forces to smaller than 10^{-4} eV/Å.

Various exchange-correlation functionals are tested, including LDA, [67] PBE, [72] PBEsol, [73] RPBE, [74] HSE06, [75–78] and PBE-D3. [79] We also used HSE(GW) method, where the HSE screening parameter is determined from quasiparticle GW calculation of the electronic structure of MgB_2. [12]

In regards to HSE(GW), the screened hybrid exchange-correlation functional allows two adjustable parameters to introduce and optimize the hybridization approach. [10] The two parameters α and μ respectively dictate the proportion of exact-exchange (Fock exchange calculated from DFT electron density) and the Coulombic screening parameter. The value α=0.25 is chosen such that the value, slope, and second derivative of the hybrid functional matches the semi-local functional in the non-interacting limit. [10] The μ parameter has been revised once, [75, 77] and even suggested to be a material-specific parameter. [12] For MgB_2, the value μ=0.6 has been determined by fitting the electronic band structure and occupancies to quasiparticle GW calculations and resulted in significantly improved description of the structural, electronic, optical and vibronic properties. [12] There can be different ways to adjust the parameters in HSE functional, but we use α=0.25 and μ=0.6 in this study, and use a name HSE(GW) throughout the remaining text in order to underline the rationale of these so chosen parameters.

The theoretical lattice parameters of bulk MgB_2 are compared to experimental values. [80] The generalized-gradient approximation devised by Perdew, Burke and

Ernzerhof (PBE) [72] is chosen for most of the calculations in this study, since it best reproduces the experimental structure and lattice constants. The choice of functional and comparison of theoretical and experimental structural parameters are discussed further in the Results and Discussion section. A Γ-centered 12×12×10 **k**-point grid is used for bulk structure relaxation, and 6×6×1 is used for surface and adsorption calculation for all the exchange-correlation functionals except HSE06 and HSE(GW). For HSE, we used a Γ-centered 6×6×3 for the bulk calculations, and 2×2×1 for $p(2 \times 2)$ supercell for the adsorption energy at high symmetry points. We use the HSE06 and HSE(GW) result to validate the PBE result, since the PBE functional is used in more computationally intensive calculations such as potential energy surface mapping, transition state calculations, and *ab initio* molecular dynamics. When not explicitly mentioned, the result is calculated using the PBE functional.

Occupancy-weighted, projected band structures are calculated in two steps. First, the ground state electronic density is calculated using a dense grid of 19×19×15 Γ-centered **k**-points. The band structures are then computed by keeping the charge density from the former step fixed and evaluating the eigenvalues on high-symmetry paths within the Brillouin zone.

The electronic charge density difference, $\Delta\rho$, is calculated by

$$\Delta\rho = \rho_{\mathrm{MgB_2}} - \rho_{\mathrm{Mg}} - \rho_{\mathrm{B}}, \tag{3.1}$$

where $\rho_{\mathrm{MgB_2}}$ denotes the charge density of MgB_2 bulk, and ρ_{Mg} and ρ_{B} denote the charge density of Mg and B layers in the MgB_2 structure, respectively. The ρ_{Mg} and ρ_{B} terms are obtained by removing the other ions from the unit cell and calculating the corresponding ground state electronic charge densities. Visualization of Eq. (3.1) emphasizes the static charge transfer due to the interaction between Mg and B layers, where we use red and blue, respectively, to represent accumulation and depletion of electronic charge density.

The oxygen adsorption potential energy surface (PES) is obtained by computing the adsorption energy of O for a dense grid of points (about 20 points per Å^2) on the MgB_2(0001) surface, allowing local relaxations, but constraining the in-plane

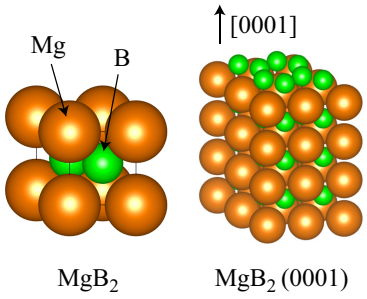

Fig. 3.1. (left) Schematic representation of the MgB_2 bulk structure and (right) $MgB_2(0001)$ $p(2 \times 2)$ surface slab model. The vacuum distance in the $MgB_2(0001)$ slab model is about 16 Å.

coordinates of the O atom. A $p(2 \times 2)$ supercell is used (Fig. 3.1) for one adsorbed O atom, which corresponds to surface coverages $\theta = 0.125$ ML for the B-terminated surface and $\theta = 0.25$ ML for the Mg-terminated surface, while the areal density of oxygen is equal in both cases. Due to the hexagonal symmetry of the surfaces, only 1/12 of the area needs to be scanned in the actual calculation, enabling a dense sampling at an affordable computational cost.

The oxygen adsorption energy, E^{ad}, is calculated by

$$E^{\mathrm{ad}} = E^{\mathrm{tot}}_{\mathrm{O:MgB_2}} - E^{\mathrm{tot}}_{\mathrm{MgB_2}} - n_{\mathrm{O}}\mu_{\mathrm{O}}, \tag{3.2}$$

where $E^{\mathrm{tot}}_{\mathrm{O:MgB_2}}$ denotes the total energy of oxygen adsorbed on $MgB_2(0001)$, $E^{\mathrm{tot}}_{\mathrm{MgB_2}}$ is the total energy of $MgB_2(0001)$, n_{O} is the number of adsorbed oxygen atoms, and μ_{O} denotes the chemical potential of oxygen. The parameter μ_{O} is a variable property of the oxygen that reflects the chemical environment. By using the ground state total energy of an oxygen molecule, i.e., $\mu_{\mathrm{O}} = 1/2E^{\mathrm{tot}}_{\mathrm{O_2}}$, we can obtain a first-principles prediction for the adsorption energy. However it is known that semi-local approximations suffer sizable self-interaction error, which can be improved by using hybrid functionals. [81] For this reason, the oxygen adsorption energy on the MgB_2 surface is calculated and compared with respect to different exchange-correlation functionals.

As will be discussed later, a severe reconstruction of the B-terminated surface is observed during the PES calculation. To further clarify the reconstruction mechanism, we investigate the oxygen-induced reconstruction of the B-terminated surface by using both *ab initio* molecular dynamics (*ai*MD) [82] simulations, as well as transition state calculations using the nudged elastic band (NEB) method. A $p(3 \times 3)$ supercell is used to explore a possible longer-range reconstruction pathway. The *ai*MD is performed in the canonical ensemble, based on the Nosé algorithm. [83] A time step of 1 fs, a kinetic energy cutoff of 400 eV, and a Γ-centered 2×2×1 **k**-point grid are used for the simulation, which was run for over 3 ps. The temperature control is set to 600 K with a Nosè period of 80 steps, providing sufficient thermal activation to capture the surface reconstruction within the limited duration.

We further explore the transition state energies using the nudged elastic band (NEB) method, where force-relaxed reconstructed snapshots are taken as the constraint configurations. Ten intermediate images are used for the transforming configurations between two constraints. A Γ-centered 4×4×1 **k**-point grid, kinetic energy cutoff of 400 eV, and dipole-corrections along the c axis are used with the $p(3 \times 3)$ supercell. A series of density-of-states calculations are performed for each transition state snapshot to examine the evolution of the electronic structure.

3.3 Results and Discussion

The bulk lattice parameters of MgB_2, calculated using different exchange-correlation functionals, are listed in Table 3.1. The generalized gradient approximation as formulated by Perdew, Burke, and Ernzerhof (PBE) is found to yield the closest agreement with experimental values. Although bulk MgB_2 has an alternating layered structure, the nature of the interlayer interaction is significantly different than van der Waals bonding. [84] While van der Waals layered materials typically exhibit strong covalent bonding in-plane and relatively weak interlayer coupling, in contrast, the interlayer interaction of MgB_2 is found to be ionic. [85] In fact, when we introduce weak-force

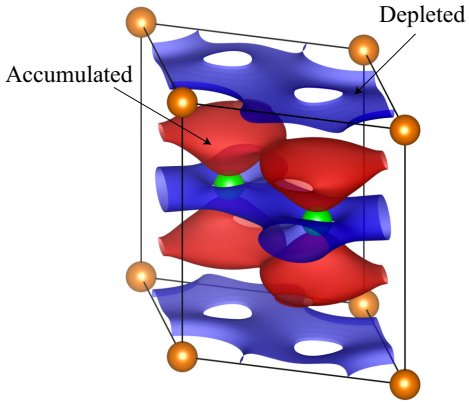

Fig. 3.2. Electronic charge density difference plot of bulk MgB_2, as defined by Eq.3.1. An isosurface level of $0.034\,e/\text{Å}^3$ is shown. Electronic charge density accumulation is expressed in red color, the depletion is in blue color. The B $2p$ orbitals are filled with electrons transferred from Mg layer and also from in-plane σ bondings of B layer. Orange and green colored spheres represent Mg and B atoms, respectively.

corrections using the GGA-D3 scheme by Grimme, [79] the theoretical results deviate further from the experimental measurements, as seen in Table 3.1. [80]

The ionic character of interlayer interaction of MgB_2 is evident from Bader's atoms-in-molecules charge analysis [87,88] of the charge transfer. In MgB_2, Mg transfers most of its valence charge ($\Delta\rho = -1.94e$/atom) to B ($\Delta\rho = +0.97e$/atom). The transferred charge leads to filling of B $2p_z$ orbitals as indicated by the plot of charge density difference, $\Delta\rho$, depicted in Fig. 3.2. In experiments, a refined x-ray diffraction study coupled with maximum entropy analysis [89] showed that the electron charge density is highly localized around the B layers. [90] The interesting electronic structure of this ionic layered material gives fundamental insight on how the anisotropic superconducting gap is established in MgB_2. In a graphene-like structure, elemental boron has insufficient valence electrons available to form π bonding states, since all 3 valence electrons occupy in-plane σ bonds. However, in MgB_2, filling of the B $2p_z$ orbital by the valence charge transferred from Mg causes the boron layer to develop

Table 3.1.
Lattice parameters of MgB_2 with respect to various exchange-correlation (xc) functionals. The percentage differences to the experimental measurement in Ref. [80] are shown in the parentheses.

xc	a	c
PBE	3.077 (−0.09)	3.509 (−0.02)
PBE-D3	3.054 (−0.86)	3.470 (−1.15)
PBEsol	3.067 (−0.41)	3.485 (−0.71)
RPBE	3.096 (+0.53)	3.544 (+0.98)
HSE06	3.055 (−0.81)	3.545 (+1.01)
HSE(GW)	3.060 (−0.65)	3.547 (+1.04)
LDA	3.036 (−1.43)	3.436 (−2.10)
Exp.(T=298 K) [80]	3.081	3.518
Exp.(T=37 K) [86]	3.082	3.515

both σ bonding states and π bonding states, leading to the extraordinary two-gap superconducting gap states. [66]

It has been shown previously that the partially occupied σ bonding orbitals of the boron layer are strongly coupled with in-plane phonons. [66,91] The $\Delta\rho$ reported in this work shows further that the electron density of the boron σ bonds is slightly depleted as the interlayer charge transfer leads to formation of π bonding states (Fig. 3.2).

The occupancy resolved, projected electronic band structure of MgB_2 is shown in Fig. 3.3. Here the thickness of the lines conveys additional information of the occupancy and the colors indicate angular momentum of the Kohn-Sham eigenstates. Again, we find the B $2p$ states are filled, while Mg $3s$ state is empty in agreement with a previous DFT result using a different level of approximation. [92] This indicates ionic charge transfer from Mg $3s$ states to B $2p$, where the charge density difference result (Fig.3.2) suggests that the B $2p_z$ states are occupied. We also find the B $2s$ and B

$2p$ states are smoothly mixed in the valence states, suggesting the presence of the sp^2 hybridization. The curvature of the band structure indicates both heavy ($\Gamma \rightarrow A$) and light ($H \rightarrow A$) effective masses of charge carriers at the Fermi level, which is suggestive of the complex Fermi surface. [66] In the MgB_2 unit cell, the path $\Gamma \rightarrow A$ corresponds to the momentum vector aligned with the layer-plane normal. The flat curvature of the eigenstates along that path indicates that the electron states are localized either on a Mg or B layer, further illustrating the ionic chemical interaction between the two elements. On the other hand, the highly-dispersive $H \rightarrow A$ path corresponds to an in-plane direction in the unit cell, revealing that the metallic in-plane bonding has free-electron-like character. The MgB_2 structure is sometimes described as an analogy of intercalated graphite. [90] Indeed, the addition of a Mg layer between B layers produces the unique electronic structure that resembles the sp^2 bonding network of graphene with a σ in-plane covalent bonding network and delocalized π bondings.

MgB_2 is a unique and interesting material in terms of the nature of its atomic bonding. The nearly complete charge transfer of valence electrons from Mg to B indicates ionic bonding character, as reflected by the Bader charge analysis, charge density differences, and band structure decompositions presented in this work, which is further consistent with previous PVL dielectric theory analysis. [64] However, the in-plane chemical interaction of the B layer is found to be covalent, while the out-of-plane interaction is mildly metallic. [93] These unique properties of bulk MgB_2 present important fundamental issues related to the surface properties of the material. Since the graphene-like structure of the B layer in MgB_2 is stabilized by charge transfer from the Mg layer, a question arises of whether the bare B-terminated $MgB_2(0001)$ surface exhibits an instability. Furthermore, the Mg layer in MgB_2 has significantly reduced interatomic distances compared to the pure Mg hexagonal closed packed (HCP) structure. Thus, detailed understanding of both B- and Mg-terminated $MgB_2(0001)$ surfaces is fundamentally important.

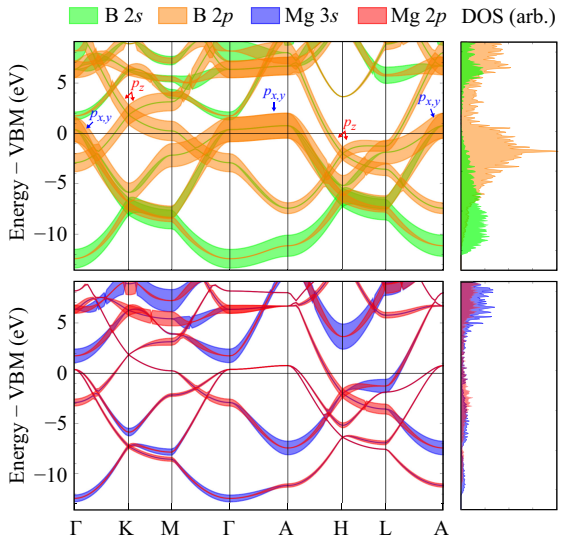

Fig. 3.3. Projected electronic band structure of MgB_2 bulk. The thickness of each band indicates the occupancy weight of the eigenstates.

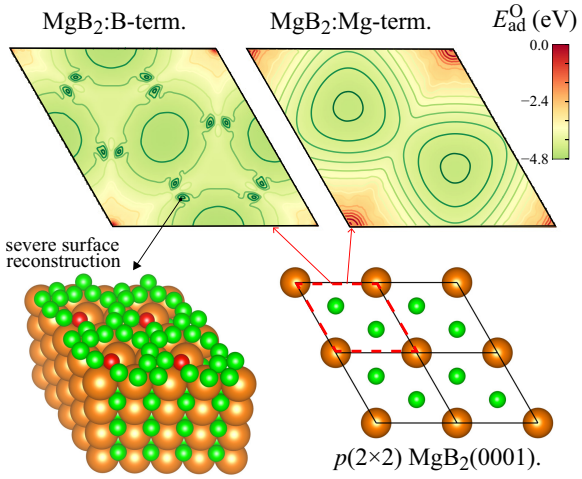

Fig. 3.4. Calculated oxygen adsorption potential energy surface of $MgB_2(0001)$.

$MgB_2(0001)$ is a stable facet observed experimentally in synthesized MgB_2 single crystals. [60] In a previous experimental study, Auger spectroscopy of polycrystalline MgB_2 revealed both Mg-rich and B-rich phases of the MgB_2 surface. [52] Soft-x-ray spectroscopy of polycrystalline films showed evidence of surface boron oxides. [62] Yet another study on large-area deposited polycrystalline MgB_2 film reported both Mg

and B oxides present on the surface. [63] A series of oxidation tests on MgB_2 showed that annealing at 400 °C under oxygen flow resulted in formation of metastable surface oxide phase, substantially lowering the superconducting transition temperature of MgB_2. [94] These experimental observations offer useful insight and further motivate to investigate a probable metastable oxide phase of B-terminated surface, despite the Mg-terminated surface is found to have lower surface energy in its pristine phase. [61]

In our study, we use DFT to investigate the oxygen adsorption on both B- and Mg-terminated surfaces. We performed a full evaluation of the potential energy surface (PES) for oxygen adsorption across the entire unit cell of $MgB_2(0001)$, as opposed to evaluating the adsorption energy at only a few most-stable sites. The PES result is shown in Fig. 3.4. The oxygen adsorption on $MgB_2(0001)$ is in general exothermic, consistent with the experimental observation of oxygen surface contamination. The most stable oxygen adsorption sites are found to be the bridge sites of boron for the B-terminated surface and the three-fold sites of magnesium for the Mg-terminated surface. Note that the stability of B- or Mg-terminated surfaces is a function of the chemical potentials μ_{B} and μ_{Mg}. A previous DFT study suggested that Mg-terminated $MgB_2(0001)$ may be more stable than the B-terminated surface for a wide range of μ space, however, the result also shows that there exists a B-rich phase domain where B-terminated $MgB_2(0001)$ can be more stable. [85] The theoretical surface stability calculation assumes a homogeneous and ideal surface structure, and does not explain why mixed surface phases are found in experimental studies. Interestingly, later we show that a certain surface reconstruction of the B-terminated surface might be responsible for making the Mg sub-layer accessible from the surface, leading to both B- and Mg- mixed termination.

The DFT results of this study suggest two important phenomena: (i) both B- and Mg-terminated surfaces are prone to direct oxidation; and (ii) the B-terminated surface can exhibit severe reconstruction due to the absence of the Mg valence charge-transfer capping layer, as well as due to the intrinsic polymorphism of boron. [95, 96] The Mg capping layer plays a crucial role in stabilizing the B-terminated surface. We

Table 3.2.
Oxygen adsorption energy, E_{ad}, in eV, computed using various exchange-correlation functionals for the different binding sites defined in Fig. 3.5 for both Mg- and B-terminated MgB_2. Here, we set $\mu_O = 1/2E^{tot}_{O_2}$. See the text for a description of the HSE(GW) functional.

Site	HSE06	HSE(GW)	LDA	PBED3	PBE	PBEsol	RPBE
A	-3.51	-4.30	-4.64	-4.29	-4.20	-4.25	-3.99
B	-0.56	-1.39	-1.77	-1.67	-1.56	-1.52	-1.44
C	-2.96	-3.70	-4.05	-3.75	-3.65	-3.69	-3.46
D	-2.80	-2.93	-2.85	-3.10	-2.66	-2.69	-2.54
E	-4.22	-3.34	-3.50	-3.36	-3.31	-3.29	-3.19
F	0.40	0.73	-0.24	0.09	0.21	-0.01	0.43
G	-4.76	-4.15	-4.54	-4.14	-4.08	-4.23	-3.85
H	-5.00	-4.42	-4.83	-4.40	-4.34	-4.50	-4.11

find the Wigner-Seitz radii integration of electronic charge gives 1.925 e for B atoms covered under a Mg capping layer, however, this value decreases to 1.841 e for surface B atoms of the B-terminated surface, indicating that the presence of Mg capping layer plays a significant role in determining the charge state of B layers.

For the B-terminated surface, there exist a number of binding sites that initiate reconstruction of the surface boron structures. Boron is known to exhibit a number of energetically degenerate atomic arrangements. [95, 96] The presence of such instabilities and complexity propose a possible reason why obtaining a consistent surface characterization of MgB_2 can be challenging. [53–55]

The precise reconstructed geometry reported in this study can be one of several various possible reconstruction modes, since the search for reconstructed geometry is constrained by the size and symmetry of the periodic supercell used; in fact, it is well known that pure B phases can exhibit very large primitive unit cells with more than 200 atoms. [98,99] For this reason, we may expect a wide variety of surface

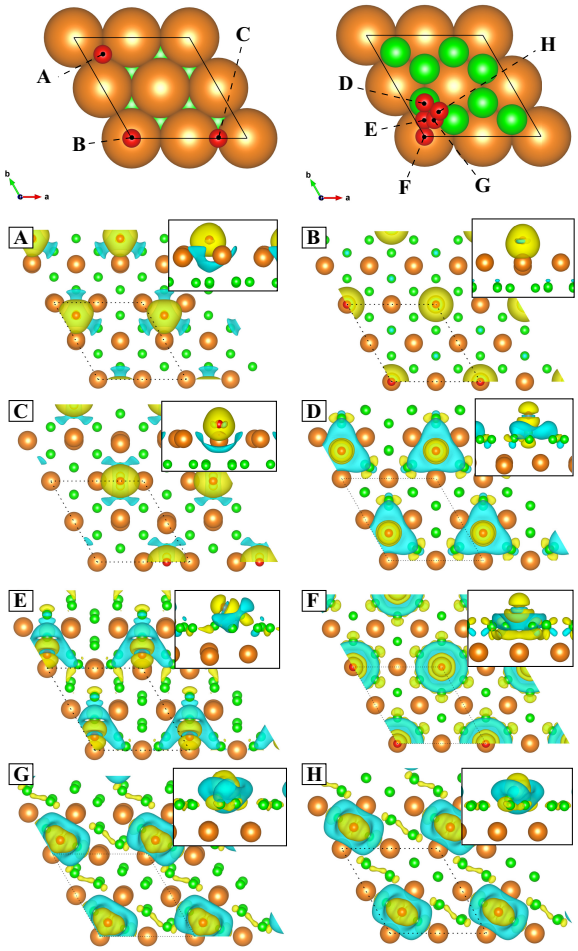

Fig. 3.5. The high symmetry binding sites on Mg-terminated (upper-left) and B-terminated (upper-right) surfaces. The calculated oxygen adsorption energies with respect to various exchange-correlation functionals are listed in Table 3.1. Corresponding charge density differences calculated at the PBE level for each binding site are shown in the lower plots. A constant isosurface level of $0.024\,e/\text{Å}^3$ is used to generate each of the volumetric representations of charge density. Top views are shown along with side views in the insets. Visualization software VESTA was used to create the images. [97] Yellow color represents electronic charge accumulation, cyan color represents depletion. For discussions in the text, we name the chosen binding sites as following: **A** Mg 3-fold, **B** Mg top, **C** Mg bridge, **D** B top, **E** B-Mg, **F** B 6-fold, **G** 2B-Mg, and **H** B bridge sites.

crystalline structure will be observed when the exposed Mg subsurface layer is oxidized and therefore chemical binding to the boron atoms on the top surface is weakened.

We use *ai*MD simulated annealing and the NEB method to identify and characterize the key reconstruction steps involved in oxygen adsorption at the surface. From the observed reconstruction reported in this study, we find generally that the surface boron atoms increase their coordination number substantially and deviate from the honeycomb graphene-like geometry upon oxygen adsorption. On the other hand, no significant reconstruction is found in Mg-terminated $MgB_2(0001)$ for the oxygen coverage considered in this study ($\theta = 0.25$). The Mg atoms in the Mg-terminated surface have a significantly reduced Mg–Mg bonding distance (3.08 Å) compared to pure Mg, therefore the close-packed Mg layer in MgB_2 is stabilized by the B layer, which depletes the outer-shell electrons of Mg and reduces the effective radii of the ionized Mg atoms.

The calculated oxygen adsorption energies of high symmetry binding sites on B- and Mg-terminated $MgB_2(0001)$ are listed in Table 3.2. The atomistic representation of the high symmetry binding sites are shown in Fig. 3.5, along with corresponding charge density difference plots. Overall, the oxygen adsorption is most favorable at Mg three-fold centers and B bridge sites. Comparison between HSE06 and HSE(GW) result is interesting because it demonstrates how the screening parameter, μ, can significantly influence the oxygen binding energy prediction. Note that the difference in the oxygen binding energy between the two functional is only 0.06 eV, which means the correction made by improving the screening parameter comes from the total energy of MgB_2 substrate. This observation underlines the significance of using optimized parameters for the hybrid functional. The binding energy calculated by HSE(GW) agrees well with other semi-local approximation, except for the B six-fold site that is not a stable adsorption site. We further observe that the PBE results are in close agreement with HSE(GW), further validating the use of PBE to describe structure, energetics, and charge transfer effects in MgB_2.

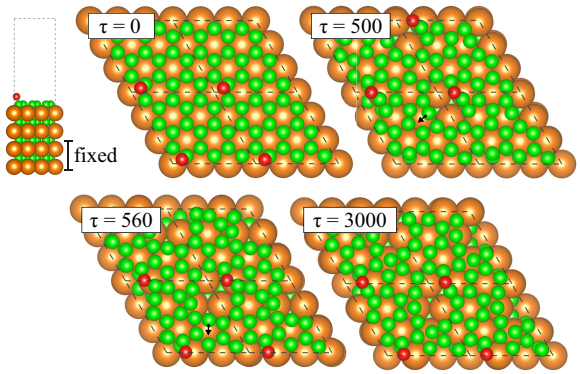

Fig. 3.6. Simulated annealing representative snapshots with respect to the timesteps preceded. The control temperature, T=600 K, is used for this simulation to enhance kinetics. Oxygen adsorption at the B bridge site and reconstruction of the graphene-like B layers are clearly shown. The final configuration remained stable and did not fall back to the original configuration over the course of the simulation.

The spatial distribution of charge transfer between the substrate and oxygen is captured by charge density difference analysis on the PBE level (Fig. 3.5). The result reveals interesting surface-adsorbate interaction. For the Mg-terminated surface, the surface electronic density changes only in the vicinity of the adsorbed oxygen, involving only a few surface Mg atoms in direct contact with the oxygen. On the contrary, for the B-terminated case, the valence charge density is disrupted by the adsorbed oxygen atom beyond the range of the first neighbors, demonstrating that the oxidation of the B-terminated surface weakens the honeycomb structure of the surface B layer by disrupting the partially filled σ bonds (see **H** of Fig. 3.5), providing reasons to understand the oxygen induced reconstruction of the B terminated surface.

The representative snapshots of the surface reconstruction modes described by *aiMD* are shown in Fig. 3.6. The depicted disruption of the graphene-like B layer is found at a specific adsorption site from the PES result shown above in Fig. 3.4. The particular adsorption site is in the vicinity of the B bridge site, but with slightly off-centered coordination. To identify the details of the reconstruction process, we performed simulated annealing as well as NEB calculations. It turns out, it is not

the specific site that produces the reconstruction, but rather the distortion of B–O–B angle that allows the local adsorbate–substrate pairs to overcome the shallow transition state energy. We found that oxygen adsorbed on the stable bridge site can also lead to surface reconstruction when a sufficient thermal energy is provided, demonstrated by the simulated annealing result. To identify the primary steps of the reconstruction, we use a $p(3 \times 3)$ B-terminated $MgB_2(0001)$ slab supercell to explore the thermally activated trajectory of the surface borons. The trajectory calculated at T=600 K reveals a key transition process of the reconstruction, from which we determine a series of static configurations and perform NEB calculations to estimate the transition state energies.

Based on the *ai*MD trajectories, we construct model structures that represent the key stages of reconstruction, followed by high-precision geometric optimizations. Once the ground state geometry is obtained, we perform NEB calculations to estimate the transition energy barrier of each boron migration process. The NEB results, obtained by using force-relaxed geometries of the static configurations, are shown in Fig. 3.7. The activation energy is found to be the range of 0.1-0.2 eV. The thermodynamic driving force behind the migration process mainly originates from the changes in electronic structure of B $2p$ states. A series of density-of-state (DOS) calculations are performed for each configuration along the transition pathways (see Fig. 3.7). These results show a decrease in the DOS corresponding to σ bonding in the B plane, *i.e.*, B $2p$ states with energies near and just below the Fermi level, for nearly all boron atoms involved in both migration pathways, (a) to (b) and (b) to (c). Notably, the DOS for the Mg $3s$ states increases during the migration, showing that the increased coordination of the B atoms is associated with a smaller charge transfer from the Mg atoms.

The NEB result indicates that the surface migration of B is a downhill process with an exothermic energy difference of -0.8 eV. The NEB results are consistent with the *aiMD* results presented above, where thermal activation was needed to trigger the reconstruction and the reconstructed geometry remained stable. In a more general

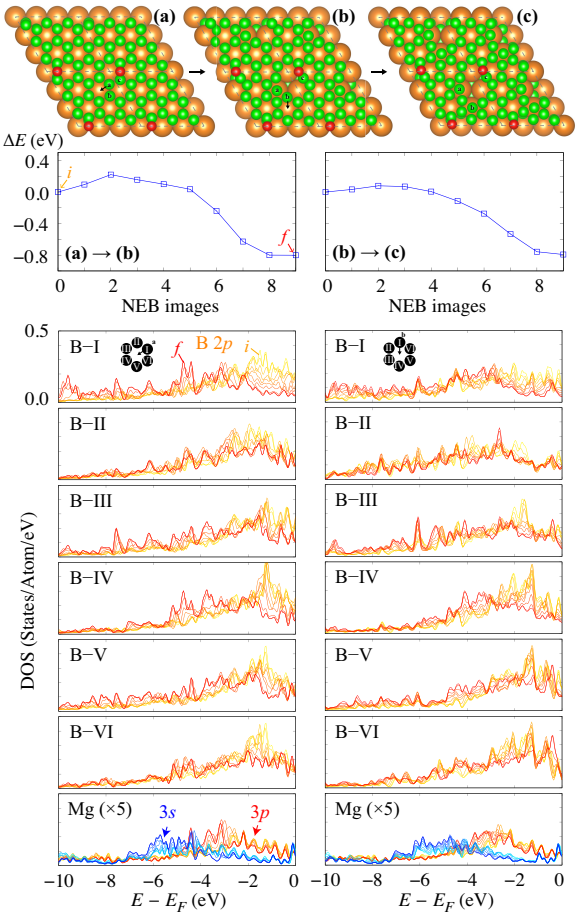

Fig. 3.7. Nudged elastic band (NEB) result showing the energy and electronic structures associated with the key transition stages of the oxygen-induced reconstruction of B-terminated $MgB_2(0001)$.

context, the reconstruction also can be triggered by other impurities that weaken the B–B partially filled σ bonds, since the migration of surface B atoms is a rapid downhill process. The HSE(GW) calculations for the reconstruction model qualitatively agree with the PBE result, showing $-1.0\,\text{eV}$ and $-0.5\,\text{eV}$ energy differences for the transition from (a) to (b) and (b) to (c), respectively.

The theoretical results in the present work suggest that the consequences of oxidation of MgB_2 are not limited to a simple formation of a dielectric layer. Instead, a significant reconstruction of the surface termination layer can occur even at relatively low O adsorbate coverages. The reconstruction disrupts the graphene-like

structure of the B layer, rendering the key process that enables high T_c superconductivity in MgB_2—namely, E_{2g} phonon mode coupling to the in-plane electronic states—no longer available. A potential consequence of having a spontaneous reconstruction pathway in this binary layer compound is that the disrupted phase may not be localized to the surface, making the surface disordering more substantial. The relatively small-scale simulation reported in this work already shows that such a reconstruction of B-terminated layer can expose the three-fold site of Mg sub-layer, as shown in Fig. 3.7, and further complexity is likely over longer distance scales of the surface. It is important to investigate further how this subtle phase disordering can influence surface-sensitive characterization experiments, such as scanning tunneling spectroscopy [53–55] or magnetic spectroscopy of the vortex structure. [51] Previous experimental study on nanoscale MgB_2 thin film (reported thickness of about 400 nm) showed that removal of surface layer of $MgB_2(0001)$ by chemical etching led to increase of the superconductivity gap energy by 25 % as measured by scanning tunneling spectroscopy. [100] A series of ultrathin film study showed the transition temperature (T_c) decreases with respect to increasing surface-to-bulk ratio of the thin MgB_2 films, [101] in agreement with the suggested idea in the present work. A surface modification strategy may be necessary in order to improve surface stability of MgB_2 thin films. [102]

Much effort has been focused on understanding the relation between the surface states and the superconductivity of thin film MgB_2. [102–105] A hypothesis has been presented that ultrathin film MgB_2 can have different T_c than bulk material, due to interaction between the surface electronic structure and the surface phonons of MgB_2 ultrathin film. Those theoretical results are mainly based on non-reconstructed pristine $MgB_2(0001)$ surfaces. The present work suggests a new possibility where surface reconstruction can play an important role in the thin film superconductivity of MgB_2. For example, a prior theoretical work showed the B-terminated surface can introduce significantly increased electronic density of states (DOS) at the Fermi level, $N(E_F)$. [104] The increase of $N(E_F)$ could be interpreted as to potentially enhance the

surface superconductivity within the view of the quasielastic approximation. However, the present work shows that $N(E_{\mathrm{F}})$ can actually decrease by reconstruction of the B-terminated MgB_2 surface (Fig. 3.7). The electron-phonon coupling of the surface states and the surface phonons might deviate from the pristine case due to the absence of E_{2g} modes in the reconstructed surface, as well. We hope the present work provides useful clues to understand the role of oxygen adsorption on introducing any discrepancies in the experimental measurements compared to the theoretical prediction based on pristine MgB_2 surface models.

3.4 Conclusions

The surface stability of $MgB_2(0001)$ under the influence of adsorbed oxygen is investigated by density-functional theory calculations. The B-terminated $MgB_2(0001)$ surface is found to undergo significant reconstruction in the present of even small amounts of oxygen. An oxygen adsorbed at the B bridge site can weaken the surface B–B σ bondings, leading to a series of B migrations that result in lowering the total energy by 0.8 eV. Low transition state energies in the range of 0.1-0.2 eV are found for this process. The opening of B-terminated layer during reconstruction results in the exposure of a three-fold site of the sub-surface Mg. The present work identifies a reconstruction mechanism of B-terminated MgB_2 that makes its subsurface layer more prone to contaminates and potential reconstruction once chemical and thermal perturbations are introduced. The present work also suggests a proper interpretation of any surface-sensitive characterization experiment may require a rigorous surface structural/chemical characterization in order to guarantee the consistency of the measurement. In addition, we conclude that surface passivation can be an important technical challenge for successful development of high T_c superconducting devices made from MgB_2.

4. AGE-HARDENING IN A TWO COMPONENT IMMISCIBLE NANOLAMINATE METAL SYSTEM

*The contents of this chapter is appeared on the journal Scripta Materialia (Kim et al., *Scr. Mater.* **136**, 33 (2017))

Density functional theory was used to predict the diffusion and precipitation of Cr in a Cu matrix. The nudged elastic band method was used to calculate the energy barrier of Cr diffusion in Cu, which is comparable to the self-diffusion of Cr, and higher than the energy barrier of Cu self-diffusion. The simulations were used to explain the experimentally measured hardness of 30nm thick nanolaminate layers of Cr/Cu-3.4%Cr. As-deposited films had a hardness of 6.25 GPa; annealing at 373K caused a decrease in hardness to 5.95 GPa, while annealing at 573K increased the hardness to 6.6 GPa. Transmission electron microscopy of the cross-section Cu-3.4%Cr layer indicate there is significant local strain due to precipitation, in agreement with theoretical predictions.

4.1 Introduction

Precipitation hardening is widely used to optimize the mechanical properties of materials. [106] While more commonly used for bulk alloys, thin films can also benefit from this hardening mechanism. A recent example of co-deposition of 5%Cr-Cu in a nanolaminate metallic multilayer (NMM) architecture showed evidence of increased hardness after annealing. [107] The Cu-Cr binary system is immiscible at low Cr compositions for temperature below 1075 °C. [108] Many examples of high strength metallic thin films have been reported by using immiscible metals to form NMMs, such as the Cu-Nb system. [109] The NMM architecture provides strengthening through layer thickness control and the subsequent interaction between interfaces

and dislocations [110], and these films are often formed via sequential sputtering. Since sputtering allows non-equilibrium and amorphous structures to be formed in thin film form [111], it is amicable to forming films that can then be precipitated by controlling the kinetics of the reaction. Other immiscible systems, such as Ti-Ni [112], and Nb-Ni-Cu [113] have been shown to increase hardness upon low temperature annealing, even when the layers were nominally pure; in these cases precipitation after possible interdiffusion at the layer interfaces has been ascribed as one possible hardening mechanism. The thermodynamic driving force behind the irreversible process of precipitation from non-equilibrium structures can be anticipated from the binary phase diagram, however, quantifying strains and the resulting impact of precipitation in a confined layer system is not easily predicted from the phase diagram. The current study utilized the Cr-Cu system as a model for precipitation hardening in NMMs. Density-functional theory (DFT) was used to examine the electronic structure of Cr in Cu using a solid solution and precipitated condition for 3.7 at.% Cr in Cu to understand the differences between solvated and precipitated alloys. These conditions were then compared to the measured hardness for as deposited and annealed samples. Transmission electron microscopy (TEM) of those samples indicates that the annealing increased local strain, without disrupting the multilayer interface structures.

4.2 Methodology

Cu-Cr 3.7 at.% alloys in solid solution (S) and precipitated as a Cr4 cluster (P) were modeled with a Cu face-centered cubic (FCC) conventional unit cell expanded to a 3×3×3 supercell. The supercell has 108 Cu atoms; the length of the edge is 10.89 Å. For reciprocal space integration, a gamma-centered 3×3×3 k-points grid is used for geometrical optimization of the supercell. A gamma-centered 5×5×5 grid is used for the electronic density-of-state calculation. The DFT calculations were performed within the generalized gradient approximation (GGA) for exchange-correlation (xc)

functional developed by Perdew, Burke, and Ernzerhof (PBE) [72, 114], as implemented in the Vienna ab initio simulation package (VASP) [115, 116]. The kinetic energy cutoff for the planewave basis is set to 500 eV, and the electron-ion interactions are represented by the projector augmented wave (PAW) method [117,118]. For the solid solution model, four Cu atoms were chosen equidistantly across the periodic boundaries of the supercell, and substituted with Cr. This model represents a homogeneous solid solution of Cu-Cr 3.7 at.%. Experimentally the non-equilibrium FCC phase of Cu-Cr alloy can be made by thin film deposition. [119] For the precipitation model, four Cu atoms at the center of the supercell were substituted with Cr. After the substitution, the alloy models underwent interatomic force relaxation.

4.3 Results and discussion

The electronic density-of-states indicates the stabilization of Cr 3d states is closely related to the precipitation. The Laue diffraction pattern shown in Figure 4.1 and measured interlayer spacing (Table 4.1) indicate that the annealed structure underwent significant changes in terms of the local strain. The localized interatomic strain induced by the clustering of Cr atoms (changing from solid solution to precipitated Cr) was determined by DFT with respect to an ideal Cu FCC structure. In Figure 4.1, the calculated result shows there can be small but significant expansive strain caused by precipitation, which agrees with the measured selected area electron diffraction result.

The substituted Cr atoms introduce local strain to the matrix is shown in a 3D quiver plot in Figure 4.1.

The diffusion of Cr and Cu was studied using the climbing image nudged elastic band (CI-NEB) method. [120] The image configurations were chosen by linear interpolation along the common slip direction, e.g. [110] since the slip directions give the shortest possible diffusion pathway between an atom and an adjacent vacancy. The transition energy pathway of the Cr atom translating to an adjacent vacancy in the

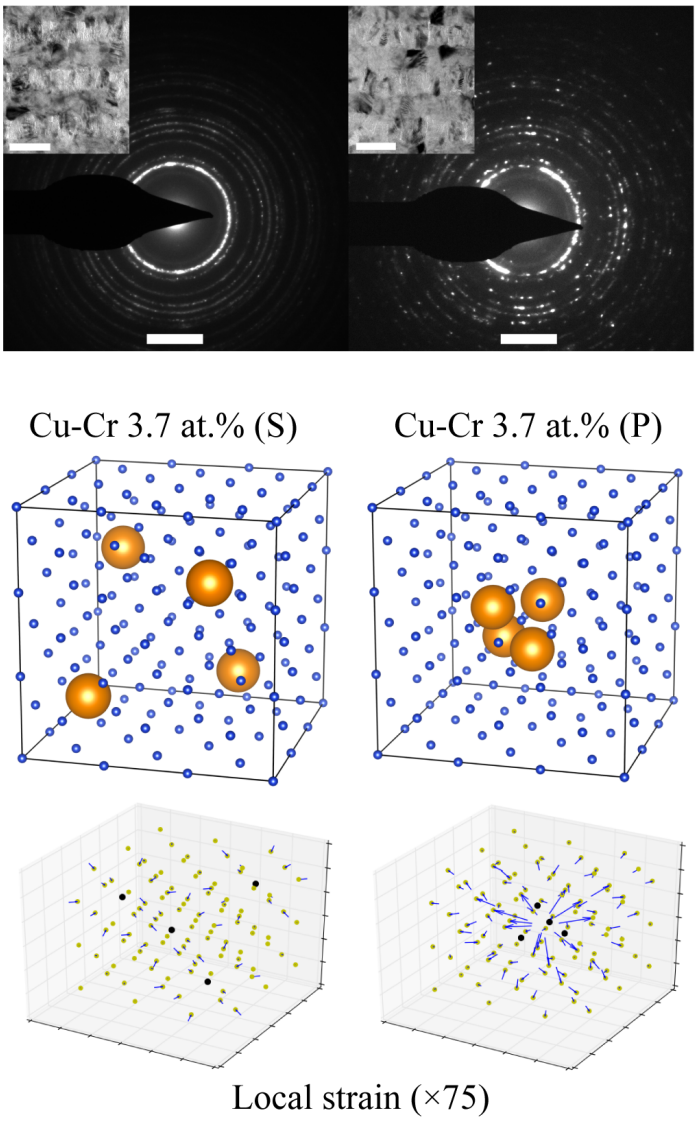

Fig. 4.1. Selected area electron diffraction (SAED) and the dark-field images of as-deposited and annealed samples are shown above. Corresponding solid solution (S) and precipitated (P) models used for DFT calculations are shown in the middle. The local strains due to precipitation are shown by quiver plot below.

Cu matrix is higher than that of Cu self-diffusion, which indicates that there can be an interesting temperature dependence of diffusion process in the alloy film, i.e. Cu diffusion can be relatively more active at lower temperature, while Cr diffusion can be

Table 4.1.
Measurement from the selected area electron diffraction shown in Figure 4.1.

As-prepared (Å)	Annealed 300° (Å)	hkl
2.089 (± 0.04)	2.101 (± 0.08)	Cu(111) / Cr(110)
1.835 (± 0.04)	1.847 (± 0.04)	Cu(200)
1.454 (± 0.02)	1.465 (± 0.02)	Cr(200)
1.300 (± 0.01)	1.301 (± 0.02)	Cu(220)
1.197 (± 0.01)	1.195 (± 0.01)	Cr(211)
1.105 (± 0.01)	1.115 (± 0.02)	Cu(311)

triggered at a higher temperature. precipitation of Cr will be temperature dependent. The image configurations were chosen by linear interpolation along the common slip direction, e.g. [110] since the slip directions give the shortest possible diffusion pathway between an atom and an adjacent vacancy. In order to show the precipitation of Cr is driven by large formation energy due to strong chemical affinity, another Cr precipitated model was constructed where three of the Cr atoms are clustered but adjacent Cr and Cu are competing to fill a vacant space of the Cr cluster. The formation of Cr4 is highly exothermic compared to the formation of a Cr3Cu cluster. This comparison corroborates that the Cr precipitation is thermodynamically driven, and originates from the electronic structure of Cr in the Cu matrix. A nanometallic multilayer (NMM) sample was deposited on a (001)-oriented, phosphorous-doped silicon wafer (368 μm thick, Virginia Semiconductor) using magnetron sputtering (ORION system, AJA International Inc.). The base pressure of the system before sputtering was 1.33×10^{-5} Pa (1.0×10^{-7} torr). A corona discharge was used to clean the silicon substrate before film deposition, using 35W with a radio frequency (RF) power supply in argon at 3.33 Pa (2.5×10^{-2} torr). After cleaning, the film was deposited onto the rotating substrate (22 rpm) in an atmosphere of argon at a pressure of 0.867 Pa ($6.5\times10^{-}3$ torr). The NMM contained 17 layers, where each layer consisted of 2 lamellae that were each 30 nm thick (i.e. 1020 nm thick). The deposition rate

was determined by measuring cross-sections created using focused ion-beam (FIB) milling. The multilayer film samples were tested in either the as-deposited condition, or after annealing at 373 K for 30 minutes, or 573 K for 30 minutes in an Ar gas environment.

The cross-section sample used for the transmission electron microscopy (TEM) was prepared by FIB milling. (NEED SOME INPUT FROM UK) The Laue diffraction pattern was taken from selected area electron diffraction (SAED) method using circular aperture (d = *** nm). (NEED SOME INPUT FROM PROF. ZHANGS GROUP)

The mechanical properties of the NMMs were investigated using nanoindentation [120]. A Hysitron Triboindenter 950 with a Berkovich indenter tip with an effective radius of 900 nm was used to produce indentations using a load-controlled, partial loading-unloading sequence. Each indentation was defined with unloading fraction of 0.5 and maximum load of 10 mN. The load function was applied in 7 cycles, and each cycle took 15 seconds for a total of 105 seconds. The testing pattern for each sample included 20 indentations with 5m spacing (4x5 arrays). The hardness was measured at contact depths ranging between 90 nm to 170 nm, about 10% of the film thickness; deep enough to be deeper than the spherical tip asperity and shallow enough to avoid significant substrate effects. [121]

From the DFT calculations, we first can compare the total energy of Cr (S) and Cr (P), The Cr4 cluster may be analogous to an embryonic stage of precipitation. The total energy of Cr (P) is lower than that of Cr (S), by 47 meV/atom (4.5 kJ/mol), since the precipitated configuration is thermodynamically more favorable than a Cu-Cr solid solution at this composition this matches the expectations of the phase diagram. [108] The local strain of Cu-Cr 3.7 at.% with the two configurations can be compared to a reference of a perfect Cu FCC structure. The Cr precipitation introduces more local strain in the matrix than Cr in the solid solution phase. The thermodynamics driving Cr precipitation are strong enough to overcome the lattice distortion required to reach the optimized local minimum. This result shows that a

very small precipitate can introduce a large local strain to the matrix material. The optimized atomic structure and calculated local strain are shown in Figure 4.1. The total displacement of all atoms in the supercell of the solid solution is 0.36 Å, while in the precipitate model it is 0.96 Å. By comparing the electronic density-of-states of the Cu-Cr 3.7 at.% (P) and (S), we find a plausible answer to explain the origin of such significant thermodynamic driving in terms of the electronic structure (see Figure 4.2). When Cr is homogeneously dispersed in Cu matrix, the 3d states are localized in the vicinity of the Fermi level. However, when Cr atoms form a precipitate, it enables the Cr 3d states to split and stabilize, shifting the peaks of the occupied states to those lower in energy. The Bader charge analysis [122] defines the extent of electronic charge transferred to or from each atom. In Cu-Cr 3.7 at.% (S), each Cr atom transfers about 0.52 valence electronic charge off to the rest of the Cu matrix. However, this number reduces to about 0.4 when Cr atoms form a Cr4 cluster. When a Cr atom is in solution, Cr loses a part of the valence electrons, however, when Cr is near/contacting other Cr atoms then Cr recovers some of the lost valence charge filling the Cr 3d states, with the peak in density-of-states shifting to lower energy with respect to the Fermi level. The electronic structure of Pd-Al alloy system was used to explain the stability of the B2 phase. [123] For Cu-Cr alloy systems, Liebscher et al. [124] reported that the electronic structure of the local Cu-Cr alloy phase can be significantly different than that of pure Cu, in agreement with the present work..

In order to form precipitates, Cr atoms have to diffuse through the Cu matrix. This diffusion process can be facilitated by vacancy-mediated mechanism since the size of the two atoms are similar. We use climbing-image nudged elastic band (CI-NEB) method to calculate the saddle point pathway to present a qualitative comparison of the diffusion barriers. We compare three ideal cases: self-diffusion of Cr in BCC Cr matrix, self-diffusion of Cu in FCC Cu matrix, and diffusion of Cr in FCC Cu matrix. The transition state energy results are shown in Figure 4.3.

The Cr in Cu matrix experiences a larger diffusion barrier than Cu in pure FCC (compare Cr V_{Cu} and Cu V_{Cu} in Figure 4.3). The magnitude of the highest transi-

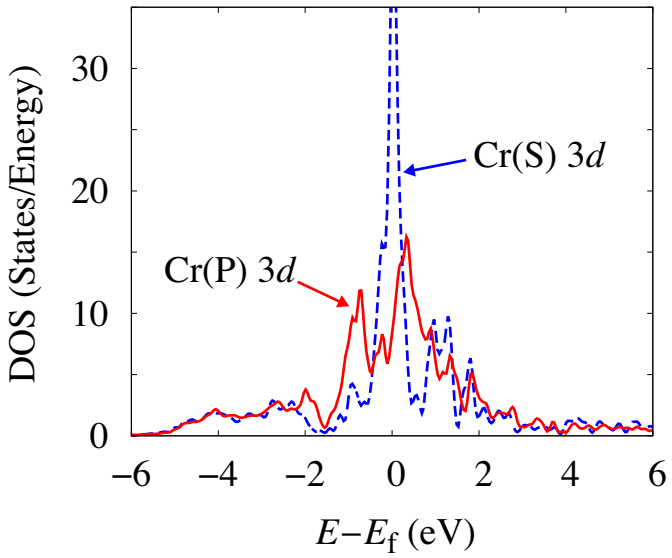

Fig. 4.2. Electronic density-of-states of Cr atoms in the two different alloy system. Note that the electronic structure of the precipitated (P) model is significantly different to that in a solid solution model (S).

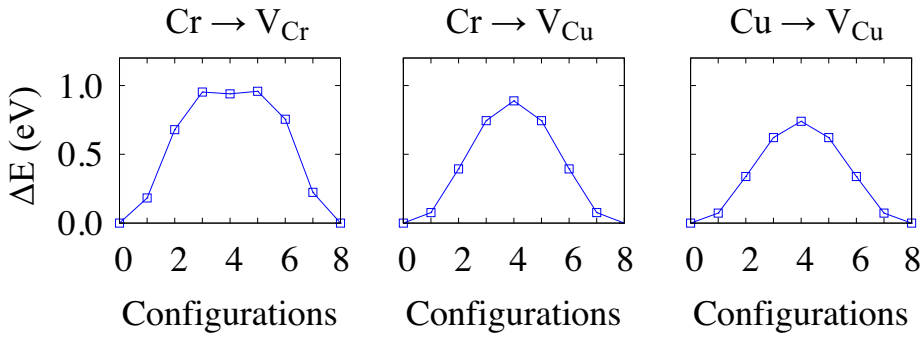

Fig. 4.3. Transition state energy of diffusion process, calculated by climbing image nudged elastic band (CI-NEB) method.

tion state energy of the diffusion model can be considered the diffusion barrier. DFT calculations coupled with CI-NEB method have been successfully used to define the diffusion barrier of carbon dissolved in iron. [125] For Cu-Cr 3.7 at.% alloy system, the diffusion barrier of Cr moving into an adjacent vacancy of Cu FCC lattice is 0.89 eV, compared to 0.74 eV for Cu in the Cu FCC lattice. To estimate the im-

pact on diffusion we can use the empirical Arrhenius form, $D = D_0 \exp(-E_a/k_B T)$, where the calculated diffusion barrier from CI-NEB is the activation energy barrier, E_a, and the preexponential term can be calculated as a function of lattice vibration frequency. [125] Since both the Cu atom in pure Cu and the Cr atom dissolved in Cu matrix assume the same FCC lattice structure and the effective mass is similar, it is reasonable to assume the most significant difference will be in the exponential term. The exponential term of Cr diffusivity is only 0.9% of the exponential term of Cu self-diffusivity at 373 K. At 573 K the relative magnitude increases to about 5%. Therefore one may expect precipitation to occur significantly faster when annealed at 573K.

To assess the influence of precipitation of Cr on the hardness of the films the NMMs were annealed at 373K and 573K for 30 minutes. Since Wo et al., [107] confirmed the precipitation of Cr using transmission electron microscopy (TEM) in a Cu-Cr 5 at.% alloy under similar annealing conditions we expect a similar type of precipitation occurs in this study. As shown in Figure 4.4, annealing at 373K results in a slight decrease in strength, while annealing at 573K resulted in an increase in strength. This annealing assisted hardening has not been observed in pure multilayers of Cu/Cr, [126] where stress assisted Cu diffusion and softening of the overall mechanical strength was observed instead. Cu diffusion may enhance grain growth, increase dislocation annihilation, and lessen some of the interlayer stress from the deposition process. At temperature increases, Cr diffusion and precipitation processes should begin, which will subsequently increase the strength of the multilayer despite the possible grain-growth. The strength does appear to increase more Cr precipitation than solid solution strengthening, matching the DFT results of total lattice distortion being greater in the precipitate Cr case.

In summary, DFT finds Cr strongly favors precipitation in accordance with experimental Cu-Cr binary phase diagrams. It is also found that the precipitation results in an increase in local strain to Cu matrix. The Laue diffraction by cross-section TEM confirmed a significant changes of local strain is found after annealing. The electronic

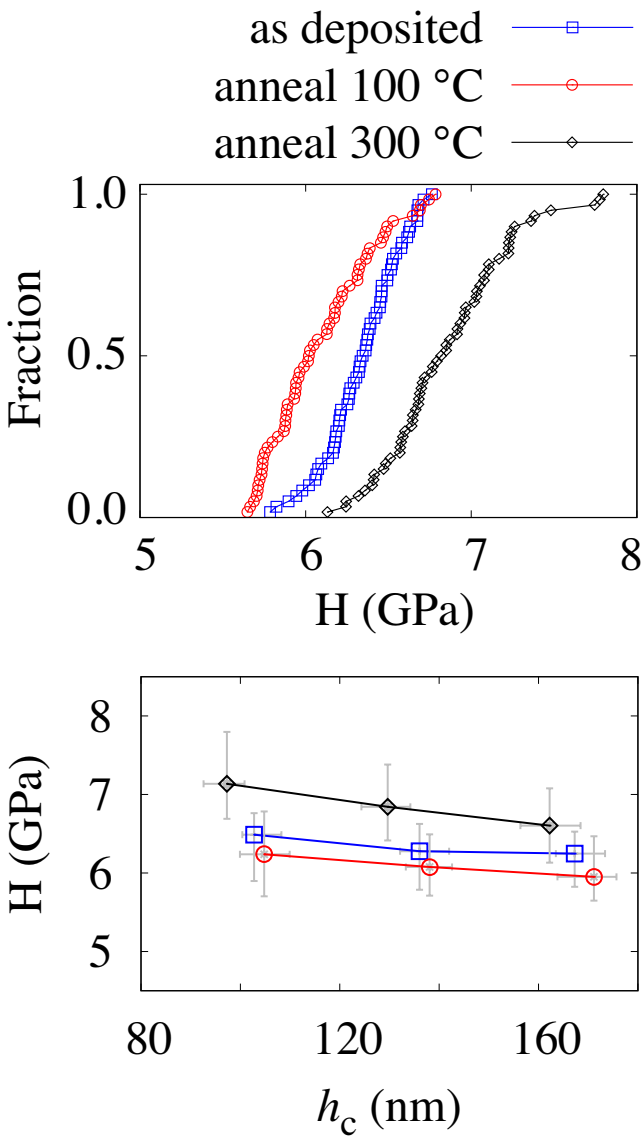

Fig. 4.4. Hardness of Cr 30nm / Cu (Cr 3.4 at.%) NMM. The fractional distribution shows the entire range of measured hardness between depths of 90-170 nm, while the hardness as a function of depth shows only a minor size effect and no significant influence of the substrate.

structure identifies that Cr transfers valence electron charge to the Cu matrix, and precipitation allows Cr to recover the depleted valance charge filling the Cr 3d states. Cr in a Cu matrix experiences a higher diffusion barrier than the self-diffusion of Cu. The hardness of a 1000 nm thick NMM with layer thicknesses of 30 nm of alternating

Cr/Cu-3.4%Cr decreased when annealed at 373 K, but increased when annealed at 573 K. This is attributed to low temperature annealing softening the film due to likely changes such as dislocation annihilation, but higher temperature annealing results in strengthening due to precipitation of Cr.

5. SYNTHESIS, MICROSTRUCTURE, AND MECHANICAL PROPERTIES OF POLYCRYSTALLINE COPPER NANO-FOAM

*The contents of this chapter is appeared on the journal MRS Advances (Kim et al., *MRS Adv.* **3**, 469 (2018))

A polycrystalline Cu foam with sub-micron ligament sizes was formed by creating a non-woven fabric via electrospinning with a homogeneous mixture of polyvinyl alcohol(PVA)-and copper acetate($Cu(Ac)_2$). Thermogravimetric measurement of the electrospun fabric of the precursor solution is reported. Oxidizing the precursor fabric at 773K formed an oxide nano-foam; subsequent heating at 573K with a reducing gas transformed the CuO nano-foam to Cu with a similar ligament and meso-scale pore size morphology. A cross-section prepared by focused ion beam lift-out shows the polycrystalline structure with multi-scale porosity. The mechanical property of the Cu nano-foam is measured by nano-indentation. The load-depth curves and deduced mechanical properties suggest that additional intra-ligament pores lead to unique structure-property relations in this non-conventional form of metal.

5.1 Introduction

Metallic nano-foams are attractive materials for catalysis due to their extremely low density and high specific surface area. Dealloying precious metals has been widely used to study porous metal phases, [127] however, this method has several limitations. Dealloying limits exist in the choice of metal phase, the accessible density domain, and the microstructure of the resulting ligaments. The fact that the crystal structure of the host metal prior to deposition remains in the porous structure means the vast majority of dealloyed films consist of single crystal ligaments. [128] Two physical aspects

that made the dealloying method particularly useful in studying low-density metal foams are: (i) spatially confined diffusion and coalescence of the alloy components, and (ii) removal of the unnecessary frame material, e.g. by using chemical etchant in the case of conventional dealloying process. In the present work, we report a synthesis of low-density nanoscale metallic foams that can facilitate further exploration of the strength-density relation of porous materials. Using an electrospun non-woven polymer fabric as a sacrificial template enables the confined diffusion and coalescence of the metal nuclei. In this templated synthesis route, the choice of constituent metal species is determined by the solubility of precursor in the electrospinning process instead of an elements reduction potential, as in the dealloying method. Electrospinning provides scalability to the synthesis of nanoscale metal foams. [129] Removal of the polymer template is achieved by pyrolysis instead of using chemical etchants. In the present approach, the metal precursors decompose and nucleate inside the polymer template. Further coalescence proceeds as the polymer network undergoes thermal decomposition and shrinkage, in short, the nucleation-diffusion mechanism dictates the microstructure of the nano-foam in the present approach. In comparison the microstructure from the dealloying method is not dictated by nucleation mechanism. As a result the templated synthesis method creates a fundamentally different microstructure distinct from that of dealloying method.

5.2 Methodology

The electrospinning of PVA-$Cu(Ac)_2$ fiber was carried out by using a Spellman SL300 high voltage controller. The external voltage was set to 15kV, the target was placed 12 cm away from the syringe tip, and the current limit was set as 2 mA. The deposition was carried out for 30 minutes. The PVA-$Cu(Ac)_2$ electrospinning solution was prepared by mixing deionized water, polyvinyl alcohol (MW=124k-186k, Aldrich, 87-89% hydrolyzed), and copper(II) acetate monohydrate (Fisher Scientific Acros, ACS Reagent grade) in $8.4 : 0.6 : 0.84$ by mass ratio at room temperature.

The syringe pump speed was 0.17mL/h. Commercially available aluminum foil (24 m thickness) was placed on a target holder made of 3D-printed poly-lactic acid to collect the fibers. Once collected on Al foil, the sample was dried in ambient atmosphere for 30 minutes, mechanically detached from the foil, and then processed with subsequent thermal treatments. The first heat treatment was carried out to burn-off the PVA. The temperature was increased from room temperature to 500 °C at 5 °C/min, held for 2 hours, and then cooled to room temperature at approximately 5 °C/min. The electrospun PVA/$Cu(Ac)_2$ fibers undergo thermal decomposition, leaving a CuO nano-foam behind. A substantial macroscopic shrinkage of the electrospun fabric was observed, likely why a distinct foam structure was obtained instead of a fused wire network observed in previous studies. [130] The thermal decomposition profile was obtained by thermogravimetric scanning from 25 °C to 500 °C by a ramping rate of 5 °C/min, using TGA-Q50 (TA instruments Inc.). The CuO nano-foam specimens were thermally processed in a reducing gas atmosphere (95% Ar, 5% H2). The CuO nano-foam was placed at the center of a quartz tube furnace that is equipped with optical radiate heater. The forming gas was flushed for 30 minutes at 40 sccm. The temperature was then increased to 300 °C using the optical heater at 30 °C/min. The heat treatment lasted for 30 minutes. After the heat source was turned off, the specimen cooled to room temperature while the reducing gas kept flowing. The overall shape of the final specimen is largely determined by the shape of electrospun template. A macroscopic fabric on the order of 70-80 mm in diameter reduces to a metal nanofoam about 20 mm in diameter, and the foam is on the order of 5-10 m thick using the process described here. We used scanning electron microscopy (SEM) in a dual beam Quanta 650 Focused Ion Beam (FIB) to characterize the morphology of the nano-foams. Secondary electron images were used to determine the microscopic morphology of the nano-foam. Samples for transmission electron microscopy (TEM) were prepared using the FIB and an Omniprobe 200 (Oxford instruments Inc.) nanoscale manipulator to lift-out a Cu nano-foam section, which was subsequently attached to a Mo grid post. X-ray diffraction, with a Bruker D8 with Cu K- (=

1.5406) radiation, was used to identify the crystalline phases of the nano-foams over the range of 2 = 25° to 55° at a scanning rate of 10 °/min. The TEM diffraction and imaging was carried out using a Tecnai T20 (FEI) equipped with a LaB6 thermionic source and a Gatan 4 megapixel camera. Selected area electron diffraction (SAED), bright field (BF) imaging and centered dark field (cDF) imaging were used to determine the polycrystalline structure of the Cu nano-foam from the cross-section. The mechanical property of the Cu nano-foam was measured by nanoindentation using a Hysitron Triboindenter 950 equipped with a flat cylindrical diamond tip with a diameter of 100 m, [131,132]. The flat-punch tip was used due to substantially variable microstructure of the nano-foam.

5.3 Results and discussion

The morphology and thermogravimetric analysis (TGA) of the electrospun fiber fabric are shown in Figure 5.1. With increasing temperature, the total weight of the fiber sample decreases due to decomposition and evaporation of the $Cu(Ac)_2$ metal precursor and the pyrolysis of the polymer template. Thermogravimetric analyses for each component are reported elsewhere. [133–135] The characteristic decomposition peaks are significantly shifted to lower temperatures (by 80°C for electrospun PVA, and about 30-50°C for $Cu(Ac)_2$) than previously reported, suggesting the thermal decomposition of the $Cu(Ac)_2$-PVA mixture follows a different kinetic pathway than those of each individual component. The strong interaction between precursor-template has not been further investigated in this work.

After pyrolysis of the electrospun fiber at 500°C, a polycrystalline nanoscale foam structure made of nano-sized CuO grains is obtained, as shown in Figure 5.3. A notable difference is this structure no longer has the geometry of a non-woven fabric, but appears more three-dimensionally interconnected. A previous study by Lin et al. has shown the $Cu(Ac)_2$ almost completely transforms to CuO when heated above 500°C. [134] Because the nucleation occurs within the confined geometry set by the

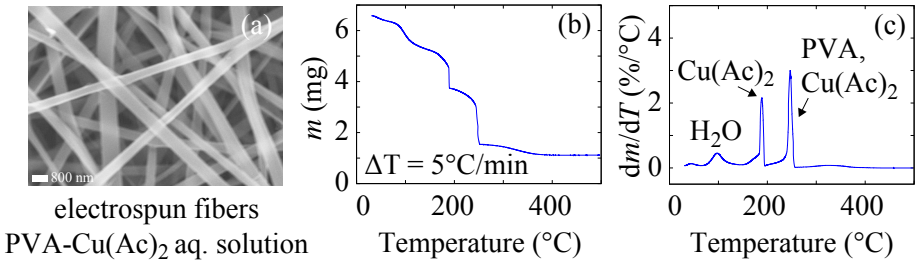

Fig. 5.1. (a) Scanning electron microscopy image of the electrospun PVA-$Cu(Ac)_2$ fibers (scale bar = 800 nm) (b) Thermogravimetric analyses, and (c) dm/dT curve indicating characterestic peaks of the thermal decomposition of the metal acetate precursor and polymer template.

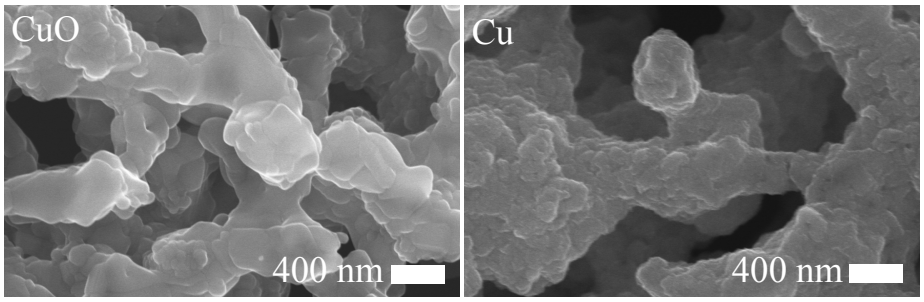

Fig. 5.2. Scanning electron microscopy images of the CuO nano-foam after thermal process at 500C, and Cu nano-foam after reducing process.

electrospun fiber, the short-range diffusion of the metal nuclei appears to lead to a conformative ligament structure. The polycrystalline morphology may be a result of reducing the surface area, form equilibrium crystalline shape, and minimize the grain boundary interface energy of the nanoscale fine grain system. This CuO nano-foam is almost completely reduced to a Cu nano-foam under the reducing gas heat treatment. Since the size of the CuO ligament is on the order of 500 nm, penetration of reducing gas species appears to be efficient. After reduction the Cu nano-foam shows increased surface porosity.

The nodular morphology of the nano-foam is somewhat misleading, as the grain size seems to be similar to the size of each oxide nodule, however, a cross-section TEM analysis (Figure 5.2) shows the polycrystalline structure of the Cu nano-foam is finer than the oxide grain size. The cross-section shows two different types of pore structures that might be caused by different mechanisms. Figure 5.2(b) shows a typical pore that is also visible in SEM images, which originate from the initial separation between adjacent electrospun fibers. There are also substantially smaller scale pores, as shown in Figure 5.2(e), where the pore size is less than the metal grain size. This small pore is located at a triple point. We suggest this (and other) pores may be created during the reduction process with different oxygen and copper diffusivities. This fine pore structure is unexpected, and the presence of such fine pores reduce the density of each ligament, creating a notable deviation from the basic assumption of Gibson-Ashby model that will be discussed in the following section.

The elastic modulus and hardness of the Cu nano-foam was measured by flat punch nanoindentation (Figure 5.4). The load-depth curves, carried out in depth control, show significant point-to-point variations (Figure 5.4(a)). The variation in load-depth curves is due to spatial variations in density of the foam and the flatness of the initial surface contact; a protruding ligament can lead to an initially soft contact (the blue curve in Figure 5.4(a)), while other regions of the film show contact with more ligaments (the green and orange curves in Figure 5.4(a), respectively). Using the constant contact area of the 100 m diameter tip and the unloading stiffness with the Sneddons approximation as described by Oliver and Pharr, the elastic modulus and hardness of nano-foam were calculated and are shown in Figure 5.4(b,c). The perceived modulus varies between 0.1 and 6 MPa, while the hardness varies between 1 and 60 kPa orders of magnitude lower than one would expect for copper [136]. The residual impression of the flat-punch tip on the foam, Figure 5.4(d), shows both densification near the periphery of the indentation while the center of the indent site deformed into a sparse net geometry, showing that several strong ligaments connections remained after the indentation, suggesting lateral, in-plane tensile stretching

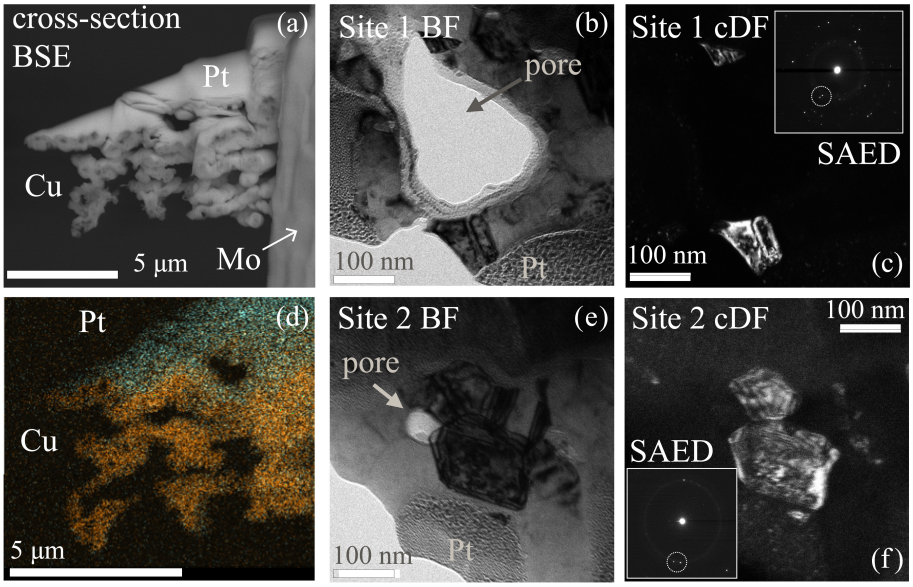

Fig. 5.3. Electron microscopy images of the nano-foams. (a) Back scattered electron (BSE) images of the cross-section of Cu nano-foam mounted on Mo grid. (b) Bright field TEM image of Cu nano-foam featuring an inter-ligament pore, (c) TEM centered dark field (cDF) image from the selected g reflections shown inset, (d) energy dispersive mapping of the sample, and (e,f) TEM BF image capturing a small pore between multiple grains, and the corresponding cDF image.

of these ligaments, rather than the out-of-plane elastic recovery of a conventional solid, may dominate the unloading response of the load-depth curve. However, other indentation measurements on porous metals (at higher relative densities of $\approx 30\%$) have observed the hardness or porous gold is on the order of 10-100 MPa, not kPa, and noted that the strength of a given ligament may be tied to the size of said ligament. [137] The Gibson-Ashby model is widely used to predict the mechanical properties of porous materials based on the properties of the bulk material.[12, 13] Since the literature suggests the strength of a ligament may be dependent on size the elastic modulus may be more robust in relating the macroscopic density of a foam to the density of the solid material,

$$\rho_{\mathrm{f}} = \rho_{\mathrm{s}} \sqrt[n]{\frac{1}{C}\frac{E_{\mathrm{f}}}{E_{\mathrm{s}}}} \tag{5.1}$$

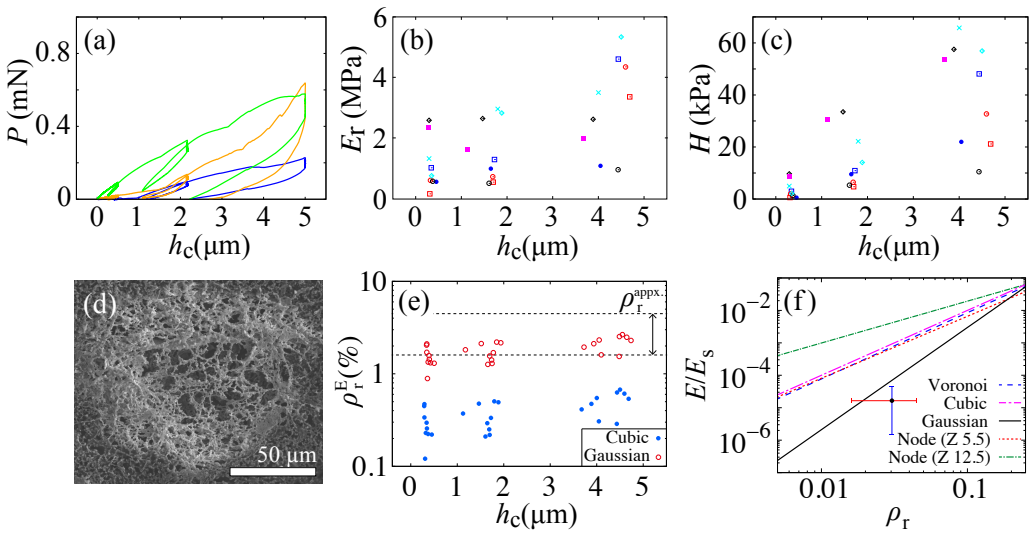

Fig. 5.4. (a) Representative load-depth curves of Cu nano-foam, (b,c) reduced elastic modulus and hardness from load-depth curves using Oliver-Pharr method. (d) SEM image of a typical residual indentation impression, (e) relative density of the Cu nano-foam, where 100% corresponds to Cu bulk phase, as calculated by the cubic open cell model by Gibson-Ashby using the measured elastic modulus. The estimated density with range in order to give comparison. Notable deviation from the Gibson-Ashby model is due to porous ligand structure of the Cu nano-foam. (f) Relative scale modulus versus density plot according to several variations of the Gibson-Ashby model. The nano-indentation measurements are shown as a black circle with error-bars. For the node network model, Z denotes the average coordination number of the network structure.

where ρ_f, ρ_s, E_f and E_s denote the density of the foam and bulk material, and the measured elastic modulus of the foam, and the bulk material respectively. For the case of cubic bending model in the original derivation of Gibson and Ashby, [138] the parameters in the equations can be approximated as C=1.0, and n=2, respectively. While this classic open cell cubic model has been widely accepted, however, the nano-foam presented in this work does not follow its general trend. The estimated macroscopic density of the foam in this study (mass divided by nominal external dimensions) was approximately 0.3 g/cm^3 (a relative density of 3%). However using the measured modulus and hardness of the foam related to that of bulk copper (a

modulus of ≈100 GPa and a hardness of ≈0.5 GPa), would lead to an estimated density shown in Figure 5.4(e), an order of magnitude lower than one would expect from the standard cubic open cell model calculation. Three possible explanations of this surprisingly low value are (1) that the foam contains significant non-connected ligaments and protrusions on ligaments (which cannot carry load) (2) the porosity within the ligaments is leading to substantially more compliant and softer foams than if the ligaments were solid or (3) the 3% relative density means ligament stretching, not node bending, may be dominating the performance and different foam models are appropriate. When compared to different kinds of random cell models, [139] the nano-foam in the present work best matches to the least regular geometry among the five different models (Figure 5.4(f)). Still, the Gaussian random model does not address the multi-scale nature of the porous ligament. In this work, we present a synthesis of a low-density (≈3%) Cu foam with nano-scale ligaments, followed by thermal, microstructural and mechanical analyses. The fine grain, multi-scale porous structure of Cu nano-foam uniform over large area may be useful for many applications, but requires further exploration of our fundamental understanding of the domain of the strength and relative density. As an example, the mechanical property of the Cu nano-foam exhibits substantial deviation from the isomorphic cellular model, which may be caused by the hierarchical porosity present (the ligaments in the porous sample themselves are porous).

A Cu nano-foam was synthesized using electrospun polyvinyl alcohol non-woven fibers as templates. As a result of thermal treatment, the polymeric fibers transform to CuO nano-foams which are then subsequently reduced to a Cu nano-foam. This resulted in a notable increase of surface roughness of the nano-foam. The fine-grained porous structure of Cu was observed with TEM cross-section imaging. The strength and stiffness of the Cu nano-foam was measured by flat punch nanoindentation, and the low values of perceived modulus and hardness suggest that the fine porous and rough structure of ligament may be responsible for the observed decreases both the stiffness and hardness of the foam.

5.4 Thermal stability of the Cu nano-foam

Metallic nano-foam has a great potential for solid-state chemistry applications due to its large surface area. Here we report the measured surface area of Cu nano-foam, and its thermal stability. Compared to metal foams created by the dealloying process, the Cu nano-foam created by electrospinning template method retained its surface area and morphology upon heating up to 400°C for 2 hours, a condition where previously reported dealloyed nano-foam showed considerable degradation. The morphology and Brunauer-Emmett-Teller (BET) surface area of the Cu nano-foam are characterized and reported. The BET surface area of the annealed Cu nano-foam is found to be 29.5 m^2/g.

The nano-porous material has expanded our understanding of the structure-property relations of material in an extremely low-density area. [140,141] Low-density metallic materials that have very high specific surface area are also of great interest in the field of solid-state chemistry as well as extreme materials physics. We previously reported a new synthesis route of Cu nano-foam. [140] Several metallic nano-foam syntheses are known to date, such as dealloying method [142], polymer templating [143], sol-gel method [144], hybrid aero-gel [145], and combustion method [146]. The present work use the electrospinning template method we reported in previous work. [140] This approach has both benefits of the polymer templating and the combustion method. The polymer templating method enables to control the morphology of final product, and the combustion method is known to retain less impurity while dealloying method suffers significant presence of the impurity coming from the template material that is not fully dissolved out.

As a first step to understand the thermal stability of the metallic nano-foam, we take the previously reported Cu nano-foam and investigate its thermal stability at T=400°C, a temperature which resulted in complete destruction of the nano-foam structure for the case of dealloyed Au nano-foams. [147] We show later that the Cu nano-foam does not exhibit notable morphology change when annealed at T=400°C

for 2 hours, in a reducing gas (5% H2, 95% Ar) condition in order to get rid of influence of any surface oxide. To understand where the superior thermal stability originates from, it is important to understand how the void spaces in both dealloyed and electrospinning templated approaches are created. Note that Cu nano-foam created by dealloying method (by dissolving Al from annealed Al-Cu fine powder mixture) shows it is prone to destruction of the porous structure. [148] In the following sections, we show the morphology of Cu nano-foam after annealing, and explain the origin of the thermal stability using schematics. The Brunauer-Emmett-Teller (BET) surface area of the heat-treated Cu nano-foam is found to be comparable to the Raney Nickel catalyst [149] or nano-foam pieces created by the combustion synthesis of metal bis-tetrazolamine (MBTA).[2, 7]

We used scanning electron microscopy (SEM) using FEI Quanta 650 (Thermo Fisher Scientific). The Brunauer-Emmett-Teller (BET) surface area is measured with Tristar II surface area analyzer, by measuring the adsorption isotherm over six points in the relative pressure range of 0.05 - 0.32. The slope and intersect of the linear fit of isotherm data are used to calculate the mass-normalized surface area of the sample. The degassing process is carried out by placing the sample under high purity nitrogen gas flow for 96 hours in room temperature.

The SEM images of the Cu nano-foam before and after the heat treatment are shown in 5.5. It is notable that the foam structure is not degraded after the annealing. It is an important advantage compared to nano-foams created by dealloying method, where significant destruction of foam structure is observed at high temperature. [147] However, from the high magnification views (5.5), we can see the small pinholes on the surface of Cu nano-foam get smoothened after the annealing. These observations suggest that the current Cu nano-foam still undergoes active surface diffusion, however the overall foam morphology was not affected.

Using standard 6-point BET measurement, we find the BET surface area of Cu nano-foam is 6.5 m^2/g before annealing, and increase to 29.5 m^2/g after annealing. Such increase of BET surface area after annealing in H2 gas condition was previously

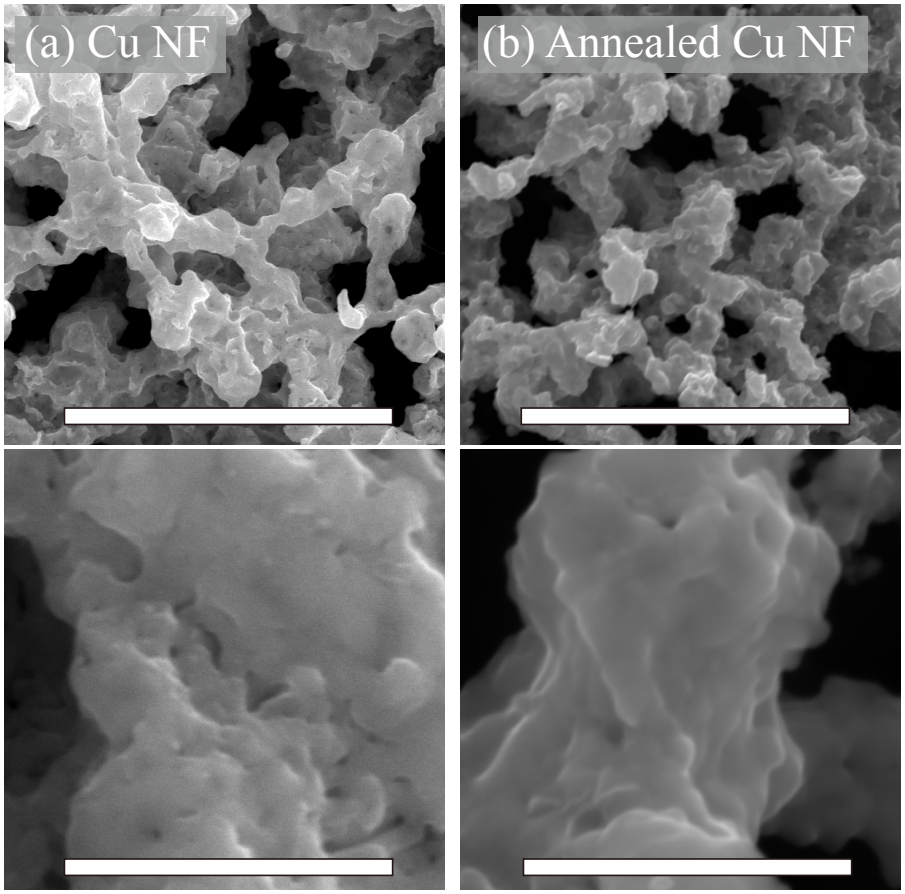

Fig. 5.5. Scanning electron microscopy images of the (a) as prepared and (b) annealed Cu nano-foams. Scale bars are 6.5 μm (top row) and 850 nm (bottom row), respectively.

observed from the combustion synthesized Fe nano-foam, [146] where a substantial increase from 20 m^2/g to 120 m^2/g was reported.

We use a pair of schematics to explain why the electrospinning templated synthesis can create a metallic nano-foam that has superior thermal stability than those made by dealloying method. The Cu nano-foam did not lose nano-porous microstructure even after annealing at 400°C for 2 hours, while previously reported Au nano-foam was substantially degraded at the same condition.

We attribute the considerably improved thermal stability to the multiscale nature of the ligament structure in the Cu nano-foam. The idea is schematically shown in

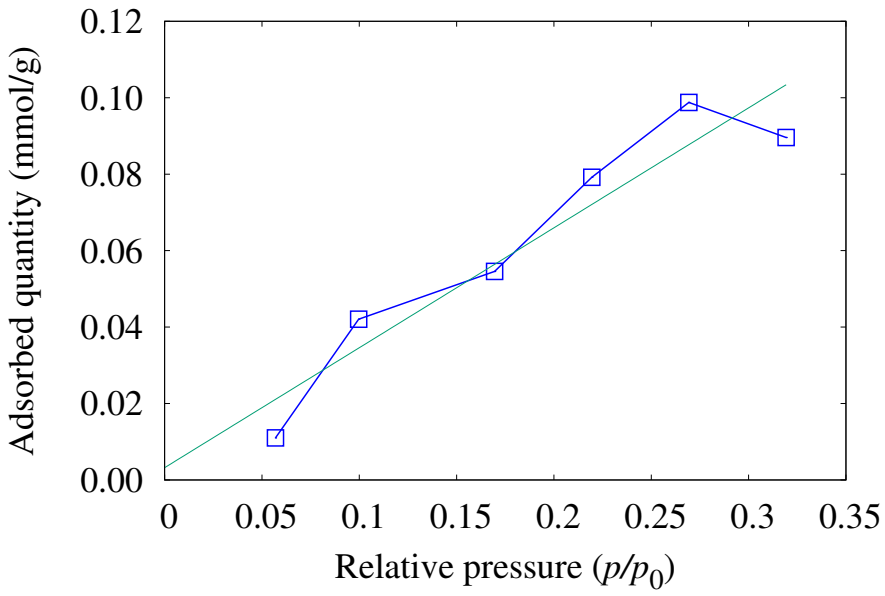

Fig. 5.6. Nitrogen gas adsorption isotherm (T=77K) of the annealed Cu nano-foam sample (annealing at T=300°C for 2 hours).

5.7. For the case of nano-foams created by dealloying process, the inter-ligament spacing is dictated by the size of the fine particle used to create the initial mixture phase. To create empty space in the mixture phase, chemical etchant is used to dissolve more vulnerable species from the mixture. Because the empty voids of the final foam is the volume that was occupied by the dissolving component. In this case the inter-ligament spacing of the dealloyed nano-foam is comparable to the size of the ligament, which can be seen from cross-section images of previous studies. [150] On the other hand, in the present work the inter-ligament spacing is not constrained by the morphology of the metallic component. Instead, it is more relevant to attribute the inter-ligament spacing to the electrospinning process control. Recent advances in creating an ordered electrospun fibers suggest an interesting possibility to create spacing-controlled metallic nano-foams.

Thermal stability of Cu nano-foam is examined by characterizing the morphology and surface area after annealing at 400 °C for 2 hours. SEM images show the pinholes

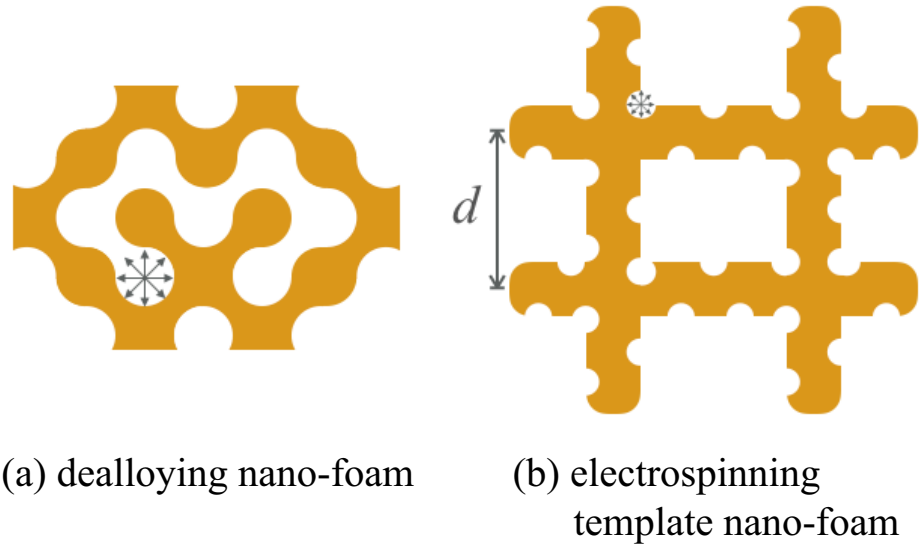

Fig. 5.7. Schematics of the metallic nano-foams synthesized by (a) dealloying method and (b) electrospinning template method. The concentric arrows represent the diffusion length of the metal species. The schematics emphasize the inter-ligament spacing of the case (b) is considerably larger than the diffusion length of the metal, which contribute to enhanced thermal stability.

of the Cu nano-foam ligaments are smoothened after the annealing, but the overall nano-foam structure has not been degraded, which is in contrast to conventional nano-foams created by dealloying approach. BET surface area of an annealed Cu nano-foam sample is measured to be in a range of 5 - 30 m^2/g. Enhanced thermal stability of the nano-foams created by electrospinning template method is attributed to large inter-ligament spacing.

6. SYNTHESIS, MICROSTRUCTURE, AND MECHANICAL PROPERTIES OF COPPER-NICKEL ALLOY NANO-FOAM

* The contents of this chapter is in preparation to be submitted to peer reviewed journals.

A polycrystalline Cu-Ni alloy nano-foam is synthesized. A previously reported electrospinning template method is used to create the random network consisting of ligaments that have diameter in a range of 200-300 nm. Scanning and transmission electron microscopies are used to characterize the morphology and microstructure of the nano-foam. Thermogravimetric analysis shows the electrospun fibers decompose in a narrow reaction temperature of about T=195°C. After the first thermal decomposition, an intermediate CuO-NiO oxide phase is created, showing phase separation of the two oxides. By reducing the mixed oxide foam in reducing gas condition, the Cu-Ni alloy nano-foam is created. The phase separation found in the oxide phase disappeared, leaving notable Kirkendall patterns, indicating intermetallic diffusion between Cu and Ni. No distinguishable segregation is observed by energy dispersive spectrum mapping. However, significant dispersion is observed from the selected area electron diffraction pattern, indicating the nanoscale grains may have significant variations in the lattice spacing, maybe due to local variation of the alloy composition. The alloy nano-foam showed higher mechanical strength compared to pure Cu nano-foam reported previously, as characterized by nano-indentation.

6.1 Introduction

We report the synthesis of a Cu-Ni alloy nano-foam. The nano-foam has unique porous structure made out of three-dimensionally connected ligaments. The ligaments have approximately $Cu_{50}Ni_{50}$ alloy composition that is determined by the amount of precursor mixed into the template. We use the electrospinning template method reported earlier. There are several known syntheses to create metallic nano-foams, such as dealloying [142], polymer templating [143], and metal salt combustion method [146] and so on. For more details about various syntheses we recommend the cited reference. [141]

The dealloying method has been widely used to pioneer metallic nano-foam studies. Typical dealloying method uses a mixture of fine metal powders followed by annealing and chemical etching. After the chemical etching, more reactive metal component dissolves away, leaving more noble metal parts behind with the porous network created by the connected metal powders. For the method relies on the differ-

ence in electrochemical potential, it is not easy to create an alloy nano-foam, unless the alloying means the residual metal component that is not washed away.

The polymer template method utilizes uniform polymer shapes such as polystyrene spheres. [143] Typically metal coating is introduced to the template by electroless deposition. After the metal coating, the template is burnt away in furnace. Metal foam created by this method retains the shape of the template. The combustion method utilizes metal precursors such as bistetrazolamine [146], which decomposes at high temperature resulting in fine polycrystalline structure with the grain size on the order of tenths of nanometers. The combustion method is known to create more thermally stable and high purity metallic foams compared to dealloying method. [141, 146]

The electrospinning template method we reported previously [140], combines the merits of both template method and the combustion method, although the chemical mechanism works differently. This method does not rely on electroless deposition nor electrochemical etching, which substantially broadens the available choices of metal elements. The electrospinning template method also creates fine polycrystalline metal ligaments, but the morphology is not completely random instead it conforms to the shape of the electrospun fibers, which means the shape parameters such as inter-ligament spacing or ligament diameter, can be controlled by using manipulating electrospinning conditions. We emphasize that the types of metal element it creates are not limited by the intrinsic chemical property of the metal as in the dealloying method, instead it is limited by controllable properties such as solubility of the metal precursors. It is also possible to use a mixture of multiple precursors in the electrospinning feedstock.

In this work, we demonstrate that a Cu-Ni alloy polycrystalline nano-foam can be created by using the electrospinning template method. The morphology and microstructure of this new form of alloy nano-foam are characterized by electron microscopies. The mechanical strength of this nano-foam is evaluated by nano-indentation and compared to previously reported pure Cu nano-foam.

6.2 Methodology

The $Cu_{50}Ni_{50}$ alloy nano-foam is synthesized by the thermal synthesis using the electrospun non-woven fabric of polyvinyl alcohol (PVA) as the template. The template electrospun fabric was created by using Spellman SL300 high voltage controller along with a syringe and syringe pump setup. The external voltage was 15kV, the target distance was set to about 12 cm from the syringe tip to the target surface. The deposition was carried out for 90 minutes. The PVA/$Cu(Ac)_2$/$Ni(Ac)_2$ electrospinning solution was prepared by mixing deionized water 16.8 g, polyvinyl alcohol (MW=124k-186k, Aldrich, 87-89% hydrolyzed) 1.68 g, copper(II) acetate monohydrate (Fisher Scientific Acros, ACS Reagent grade) 1.2 g and nickel(II) acetate tetrahydrate (Sigma-Aldrich, 99.998% trace metal basis) 1.5 g at room temperature. The syringe pump speed was 0.17mL/h. A copper plate (0.5 mm thickness) wrapped

around plastic 3D-printed mold was used as a target to collect the fibers. Once finished deposition, the electrospun fabric was dried in ambient atmosphere for 30 minutes, mechanically detached from the foil, followed by subsequent two-step thermal treatments. The first heat treatment was carried out to burn-off the PVA, using initial ramping rate of 5 °C/min to reach 500 °C, dwell for 2 hours, followed by closed oven cooling. In this first heating process, the electrospun fabric that has the precursor mixture undergo thermal decomposition exhibiting an inflection point at 196.5°C as identified by thermogravimetric analysis. As a result of the first thermal process, an oxide nano-foam was created in which both copper oxide and nickel oxide were identified by x-ray diffraction (XRD). The thermal decomposition profile was obtained by thermogravimetric scanning from 25 °C to 500 °C by a ramping rate of 5 °C/min, using TGA-Q50 (TA instruments Inc.). The XRD analysis was carried out using Bruker D8 equipped with Cu K- (= 1.5406 Å) radiation source, by locked coupled scanning mode with a scanning rate of 5 °/min. The CuO-NiO nano-foam underwent subsequent heating in reducing gas (95% Ar, 5% H_2) flow through a transparent quartz tube surrounded by optical radiation heater. The temperature was measured by thermocouple located close to the sample. Before heating up to 330 °C, the forming gas flushed for 30 minutes at 40 sccm. The temperature is slightly above the point where complete miscibility of Cu-Ni binary alloy was found. [151] The heating lasted for 45 minutes, and then the specimen cooled to room temperature while the reducing gas kept flowing. The resulting metallic nano-foam retains the original shape of the mixed oxide nano-foam with additional shrinkage. When flat, the dimension of the nano-foam is about an inch in diameter and 5-10 μm thick. The morphology of the $Cu_{50}Ni_{50}$ alloy nano-foam is examined by using Quanta 650 electron microscope that is also equipped with focused ion beam (FIB) column and lift-out probe (Omniprobe 200, Oxford instrument Inc.). A specimen for transmission electron microscopy (TEM) was prepared by using the FIB and lift-out probe. A 10μm $\times$ 0.3μm $\times$ 5μm slice of the metallic nano-foam was cut from the sample and implanted to a Mo grid post. The implanted sample underwent additional thinning down to about 100 nm in thickness. The transmission electron microscopy was carried out by using FEI Talos 200X TEM/STEM microscope equipped with ChemiSTEM (X-FEG and four silicon drift EDS detectors), operated at 200 kV.

6.3 Results and discussion

The morphology of the nano-foam changes through the thermal processes. The SEM images of the oxide foam and the reduced metallic foam are shown in Figure 6.1. The spherical features along the fabric structure are interesting, because it is later shown that these particulate features are copper-rich oxide. After the second heat treatment in reducing gas condition, the foam undergoes significant shrinkage again. It is later shown by x-ray diffraction that they are CuO and NiO, meaning that the reducing process will create oxygen vacancies as many as the number of metal

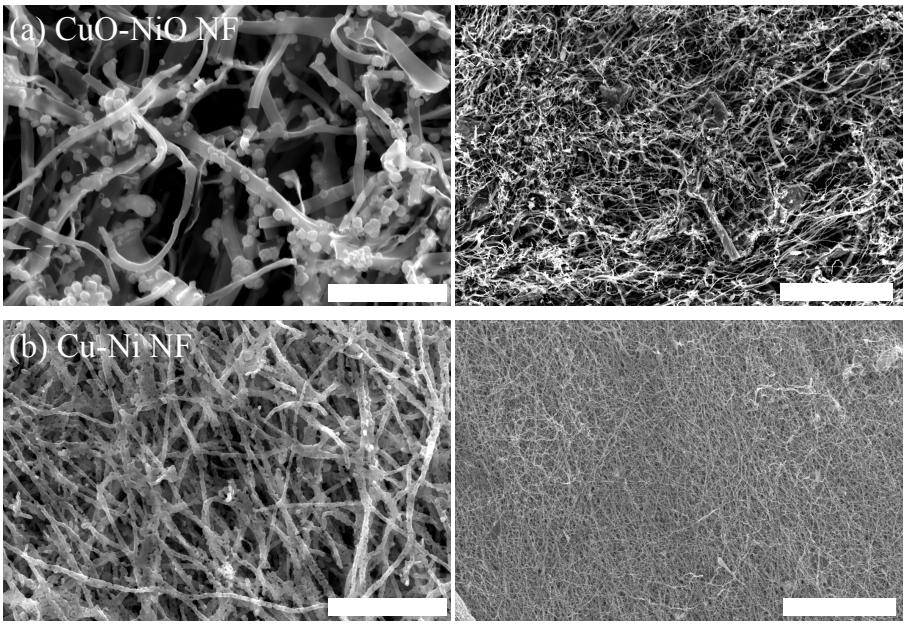

Fig. 6.1. (above) SEM images of the CuO-NiO intermediate phase, and (below) the reduced metal nano-foam. The scale bars are 5 μm for high magnification (left column) and 50 μm for high magnification (right column). The spherical features of the oxide form are copper-rich oxide as confirmed by EDS mapping.

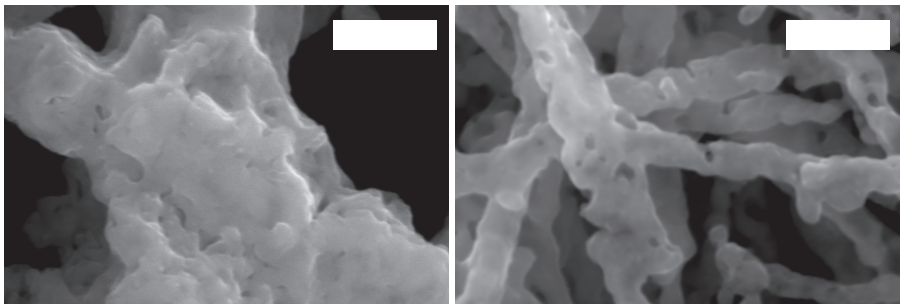

Fig. 6.2. SEM images of (left) Cu nano-foam and (right) Cu-Ni nano-foam. The scale bars are 500 nm.

atoms, which will promote active surface diffusion. It is clearly that the diameters of ligaments are reduced after the second heat treatment.

Detail morphology of the alloy nano-foam is compared to the previously reported pure Cu nano-foam (Figure 6.2). In both cases, the monoxide phase was reduced by heating in the reducing gas condition. The surfaces of both metallic foams indicate roughness and pinhole features due to creation and diffusion of oxygen vacan-

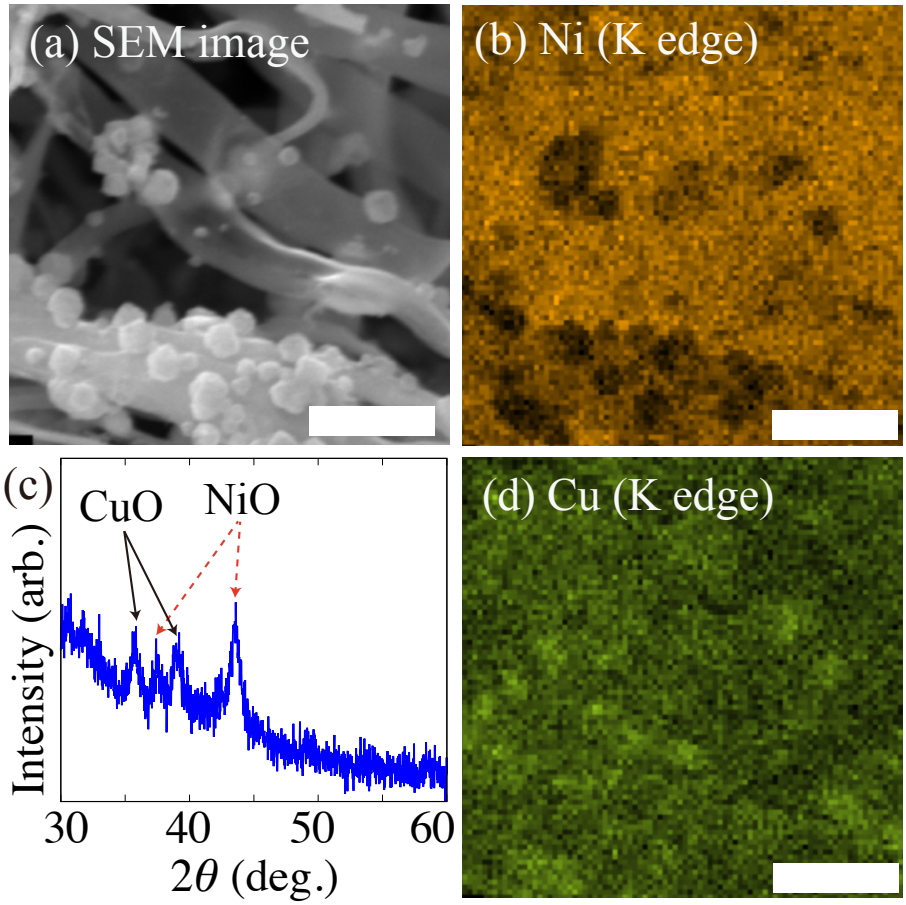

Fig. 6.3. SEM images of CuO-NiO phase, (b, d) energy dispersive spectrum mapping of Ni and Cu, respectively, (c) x-ray diffraction result of the CuO-NiO phase. The scale bars are 2 μm.

cies. For the case of Cu-Ni alloy nano-foams, each metal component has different diffusivity [152, 153], with the diffusion of Cu being more active than Ni. In such a case, unbalanced diffusion activity between two metal phases can create porous structure. [154,155], The size of pinholes in Cu-Ni nano-foam is relatively bigger than those of pure Cu nano-foam. The Kirkendall effect may be responsible for the pinhole structures as well as the creation of oxygen vacancy. It is later shown that there were significant segregation of Cu-rich (Ni-lean) oxide phase, which means the subsequent equilibration of alloy composition is facilitated by the intermetallic diffusion between Cu and Ni.

We use energy dispersive spectrum mapping to identify the nature of spherical oxide phase. It turns out they are Cu-rich (and Ni-lean) phase (see Figure 6.3). X-ray diffraction (XRD) shows that the CuO and NiO peaks are separately captured, supporting the idea of phase separation observed in SEM images. The Cu monoxide

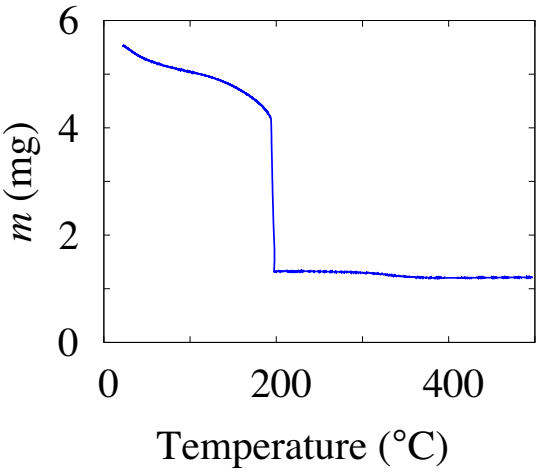

Fig. 6.4. Thermogravimetric analysis of the electrospun fabric of PVA-$Cu(Ac)_2$-$Ni(Ac)_2$ mixture. Ramping rate of 5 °C/min is used. It is peculiar to find only one steep reaction point at about T=195 °C, given that at least three different chemical reactants are present.

takes monoclinic lattice structure, while Ni monoxide takes rocksalt structure. Such lattice mismatch may have played a role in phase separation. The EDS mapping showed the particulate features are Cu-rich and Ni-lean, however, it did not provide useful information about the chemical composition of ligament. Also, the signal-to-noise ratio of the XRD result is not high enough to exclude presence of other possible alloy oxides. But one thing is clear that when it comes to reducing process, there exist numerous Cu-rich region that will need to diffuse out in order to achieve complete equilibration of Cu-Ni alloy phase.

Considering how complex the thermochemical reactions of this three chemicals poly vinyl alcohol, $Cu(Ac)_2$, and $Ni(Ac)_2$ can be, it is surprising to find from the thermogravimetric analysis that the major decomposition was completed at a singular reaction point at T=195 °C (see Figure 6.4). It is known that the $Ni(Ac)_2$ decomposes at T=350 °C to form NiO [156]. Such absence of major peak suggest the $Ni(Ac)_2$ may have developed organic-inorganic hybrid complex with other two chemicals during the homogenization. The nature of this complex consisting of the polymeric basis and the two metal precursors poses an interesting and challenging problem that may necessitate in-depth analysis of the vibronic spectrum and group symmetry. In the present work we did not further investigated the nature of this new organic-inorganic hybrid complex.

After the second thermal process in reducing gas condition, the EDS map and XRD result are shown in Figure 6.5. The observed spherical Cu-rich phases are completely disappeared. The EDS map no longer detects any distinguishable segregation in this scale. However, due to the delocalized nature of x-ray interaction volume, the

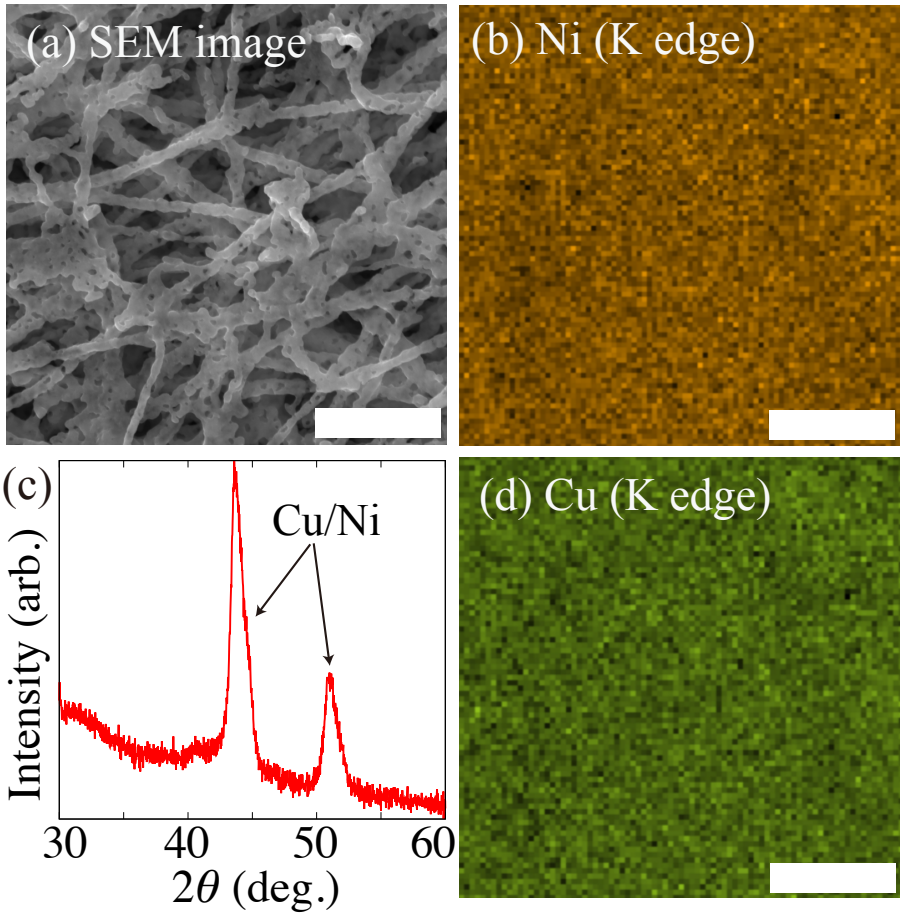

Fig. 6.5. (a, b, d) SEM image and EDS mapping of the Cu-Ni nano-foam after the reduction thermal process. (c) x-ray diffraction result confirms the oxide phases are reduced to metallic alloy phase. The scale bars are 2 μm.

EDS mapping alone does not confirm the full homogeneity of the alloy phase. Later we show more convincing characterization using transmission electron microscopy. It is notable that the diameter of ligaments are significantly reduced. Both CuO and NiO have the oxygen-to-metal ratio of 1:1, which resulted in significant loss of ligament volume that was occupied by lattice oxygens. The XRD no longer captures any presence of oxide phase, but two peaks that matches to Cu-Ni alloy phase are determined. [157] Cu and Ni share the same lattice structure of face centered cubic, with Ni having slightly smaller lattice spacing by about 0.1 Å, which means slightly larger Braggs angle. For this reason, formation of alloy phase resulted in broadening of the XRD peaks.

The disappearance of the Cu-rich phase tells there has to be intermetallic diffusion in order to achieve equilibrated alloy nano-foam. The diffusivity of Cu is considerably

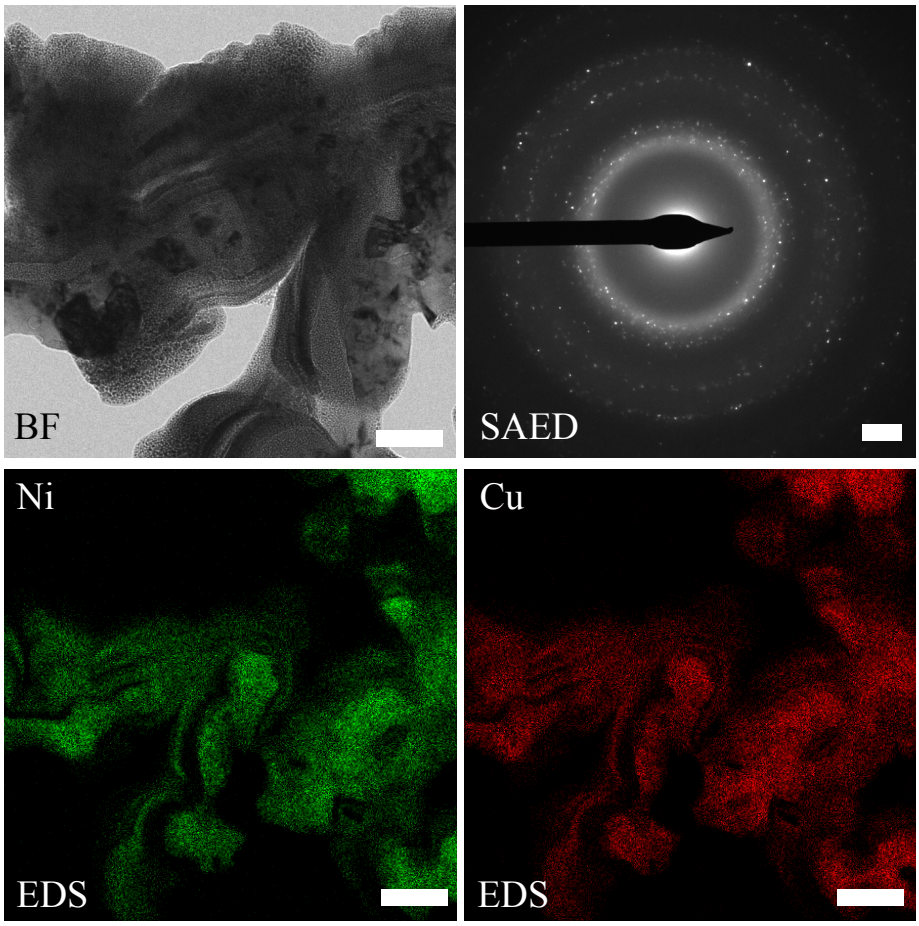

Fig. 6.6. Transmission electron microscopy result of the Cu-Ni nano-foam. The bright field (BF) image and selected area electron diffraction (SAED) show the nano-foam consists of fine crystallites. The energy dispersive spectrum (EDS) mapping below shows the Cu and Ni form alloy throughout the ligament, showing no significant segregation. The scale bars are 100 nm for the BF, 2 nm-1 for the SAED, and 200 nm for the EDS maps.

higher than Ni [152, 153], and it is previously shown that Cu-Ni multilayer creates Kirkendall pore formation in Cu layer when annealed to high temperature. The same physics maybe responsible to creation of pinhole features of the nanoscale ligaments (Figure 6.2) [155].

The transmission electron microscopy shown in Figure 6.6 provides more detail look into the microstructure of this alloy nano-foam. The bright field (BF) image shows a number of diffracted grains. The selected area electron diffraction (SAED) shows the electron diffraction pattern from the area shown in the BF image, indicating there are numerous fine crystallites diffract to variable g vectors. These very fine grain

Table 6.1.
Measured interlayer spacings with respect to various hkl. The reference d-spacings are taken from Refs [158, 159]. Δd values are calculated by $(d-d^{\mathrm{ref}})/d^{\mathrm{ref}}$. The range is determined by drawing concentric circles, bounding minimum and maximum peaks of each d reflections.

d	$d^{\mathrm{ref}}_{\mathrm{Cu}}$	$\Delta d_{\mathrm{Cu}}(\%)$	$d^{\mathrm{ref}}_{\mathrm{Ni}}$	$\Delta d_{\mathrm{Ni}}(\%)$	(hkl)
2.066 ($\pm$ 0.21)	2.088	-1.08	2.034	+1.45	111
1.787 ($\pm$ 0.06)	1.808	-1.15	1.763	+1.37	200
1.272 ($\pm$ 0.03)	1.278	-0.46	1.246	+2.09	220
1.080 ($\pm$ 0.05)	1.090	-0.88	1.063	+1.66	311
0.825 ($\pm$ 0.01)	0.829	-0.50	0.808	+2.05	331

structure is similar to the microstructure of the iron foam synthesized by combustion method [146]. In the SAED, significant variation is found from the 1st and 2nd order g peaks in accordance with the broad spectrum found in XRD. This shows that the alloy composition of individual grain can be slightly different to each other, although the overall alloy ligament is well equilibrated.

As listed in Table 6.1, the d-spacings of the specimen shows compressive strain against Cu reference, and expansive strain against Ni reference, indicating their alloyed lattice structure in average. The cloud pattern of SAED indicates amorphization of the specimen, which may be caused by the ion beam machining process. Unlike a standard thin film samples, some part of the nano-foam is not fully protected by the platinum cap during the ion beam lift-out process. For this reason, those parts of the foam that are exposed to vacuum show more amorphization than the middle part. The energy dispersive spectrum (EDS) mapping shows the x-ray signals of both Ni and Cu are comparably found throughout the specimen, showing that the alloy ligament is well equilibrated as characterized by the micrometers scale (Figure 6.5), as well as in the nanometers scale.

The EDS mapping shows uniformly dispersed Ni and Cu, however, we can further analyze the relative accumulation of one component against the other. For this purpose, an excessive accumulation map is calculated by using the following formula after applying Gaussian filter ($\sigma = 5$) to the original EDS maps.

$$\Delta C_{\mathrm{Ni}} = C_{\mathrm{Ni}} - C_{\mathrm{Cu}}$$

Where the C_{Ni} and C_{Cu} denotes the concentration profile from EDS map of Ni and Cu, respectively. The result is shown in Figure 6.7. The positive values of ΔC is considered as excessive accumulation. Compared to the outlines of the foam geometry, the Ni accumulation is relatively concentrated along the center of the ligaments, while Cu shows less accumulation with more concentration at the surface of the ligaments.

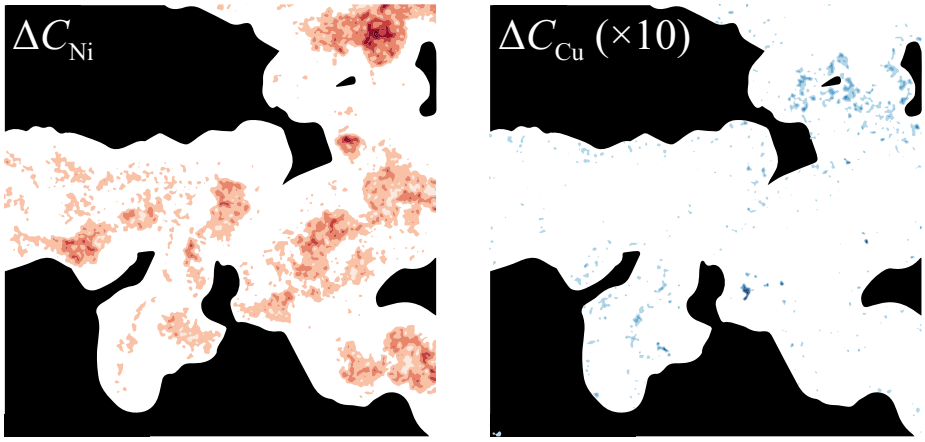

Fig. 6.7. The excessive accumulation of (left) Ni, and (right) Cu. The Ni accumulates at the core of ligaments, and Cu show an order of magnitude less accumulation around the surface of ligament. The dark shade is used to assist to locate relative location with respect to the ligament geometry.

Additional analysis on the SAED patterns from Figure 6.6 reveals the dispersion of the alloy composition of each fine grain. The analysis shown in Figure 6.8 indicates there can be compositional variations in the fine polycrystalline Cu-Ni alloy nano-foam. The analysis is performed by manually counting identifiable points in the vicinity of the d_{311} reflections. The average alloy composition is consistent with the mole fraction of the metal precursors, however, a notable peaks at Ni-rich side indicate there can be Ni segregation, in agreement with the qualitative analysis of the EDS mapping.

Combining the experimental observations so far, we can find more clearer picture of the synthesis and microstructure of this Cu-Ni alloy nano-foam. In the oxide formation stage, the Ni decomposition peak was not clearly captured from the TGA result. Pure $Ni(Ac)_2$ powder decompose at T=350°, but no distinguishable peak was observed above T=200° from the TGA result. It is unclear at this point, whether the Ni precursors formed a new form of complex compound with Cu precursors, or they remained until the second heat treatment stage. The latter is certainly a possibility, considering the sizable shrinkage after the second heat treatment, which was not observed in Cu nano-foam synthesis discussed in chapter 5. Clearly the Cu oxide phase particulate out from the ligament, and diffuse into ligament again during the second heat treatment. The grain structure of this alloy nano-foam resembles the combustion-synthesized nano-foams, [146] exhibiting fine grain structure. In a sub-micrometer scale, the cross-section TEM shows good homogenization of the alloy, however, we can still observe relative accumulation of Ni at the core of ligament, but Cu at the surface of ligament, which is consistent with the phase segregation found

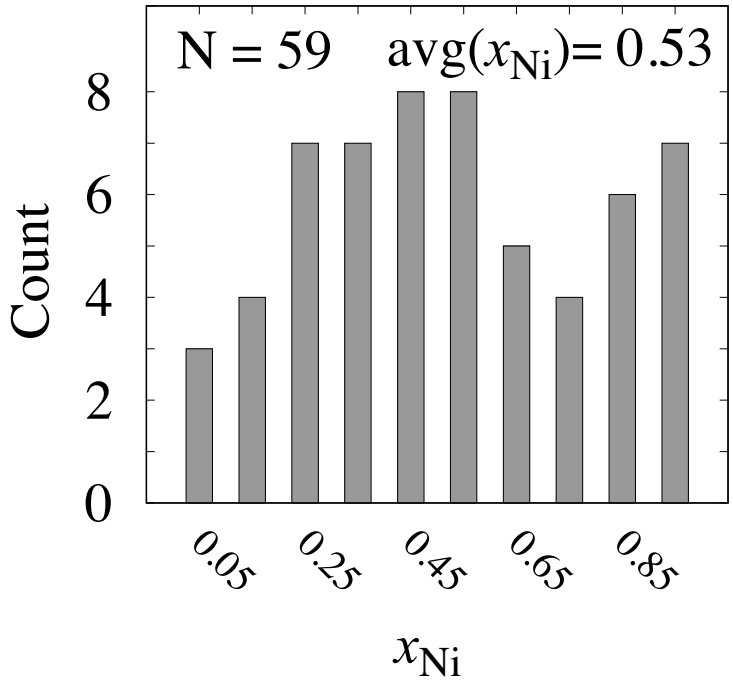

Fig. 6.8. The distribution of alloy composition in terms of x_{Ni}, obtained from the 311 reflection plane of the SAED of Figure 6.6. The composition was determined by the Vegard's law, using the measured d_{311}.

after the first heat treatment where spherical Cu-rich phase segregated out from the Ni-rich ligament cores. As a consequence of this ligament structure, we can expect the mechanical property of this complex alloy foam can be significantly different to the pure Cu nano-foam.

The nano-indentation result in Figure 6.9 shows the mechanical property of this Cu-Ni nano-foam is considerably stronger than the Cu nano-foam. When 50% addition of Ni to Cu nano-foam saw about 4 times increase of the strength, the alloy strengthening effect alone does not explain such drastic strengthening. The finer grain structure of Cu-Ni alloy may have contributed to the strengthening as well as the relative accumulation of Ni at the core of ligaments, may have affected the measured strength. More critically, the number of ligaments involved in deformation under the nano-indentation tip can be greater for the case of Cu-Ni alloy nano-foam, as the diameter of ligaments is about 3-4 times smaller in Cu-Ni alloy nano-foam. The combined effect of the chemical, microstructural, and geometrical variations foresee more in-depth analyses for the better understanding of this unique form of extremely low density phase of metal alloy.

After a series of morphological and microstructural analysis, we conclude that the Cu-Ni alloy nano-foam has a nanoscale porous ligament network, where the ligaments

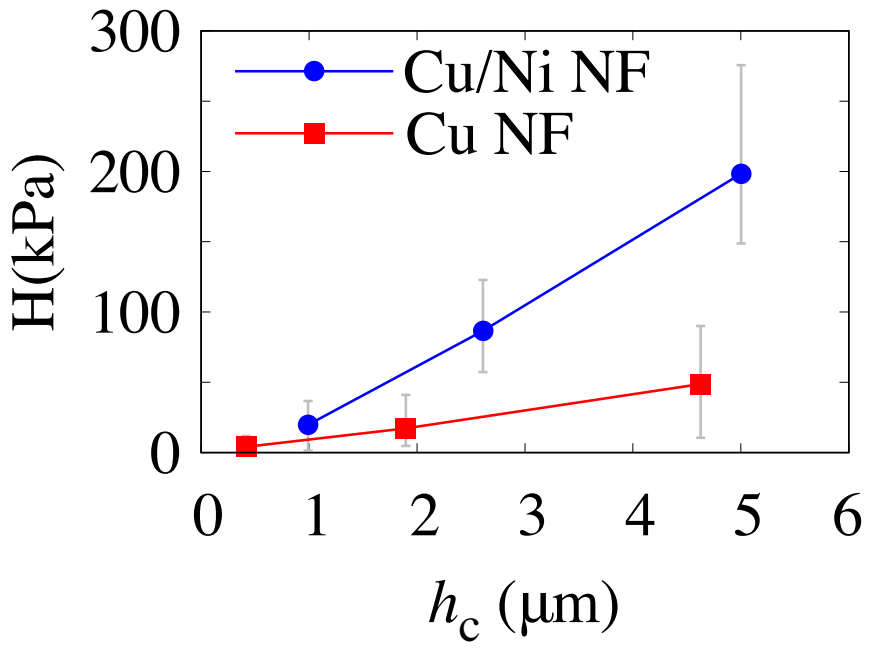

Fig. 6.9. Mechanical strength of the Cu-Ni nano-foam measured by nano-indentation, compared to the same property of the pure Cu nano-foam reported in previous study. Hardness (H) is shown with respect to the contact depth (h_c) of the indenter tip. Linearly increasing hardness of the nano-foams indicate densification of the nano-foam as the tip indented deeper. The errorbars correspond to the maximum and minimum values of the measured data points, and the markers point the average value of the data from each partial unloading segment.

comprise of well-equilibrated Cu and Ni alloy that has fine polycrystalline grain structure. These observations present new and convincing idea of the alloy nano-foam and its synthesis. At the same time, this pioneering work present numerous unsolved interesting problems, such as why the Ni precursor did not show decomposition peak in the TGA, if they formed an unknown organic-inorganic hybrid complex in the electrospun fiber; what happens between segregated oxide foam phase and the fully reduced metallic foam phase; how does the diffusivity of component influence the overall design of alloy nano-foam. The current work showed that a synthesis of alloy metallic nano-foam is feasible using the electrospinning template method, and related the microstructure of the metallic foam to the chemical design of the electrospinning feedstock.

We report the synthesis of a Cu-Ni alloy nano-foam that has random network of metallic ligament. The electrospun PVA-$Cu(Ac)_2$-$Ni(Ac)_2$ mixture decompose at about T=195 °C resulting in mixed oxide phase. Segregation of Cu-rich oxide phase

is confirmed. Subsequent reduction results in an intermetallic alloy Cu-Ni nano-foam. The initial phase separation and subsequent reduction process at elevated temperature led to obvious Kirkendall effect and pinhole features of the metallic ligaments. The cross-section TEM shows the ligaments are fine polycrystalline. Mechanical property of the Cu-Ni alloy nano-foam is measured by nano-indentaion and compared to the previously reported Cu nano-foam. Significant strengthening of the mechanical property is observed that exceeds what one would expect from solid solution hardening.

7. SUMMARY AND CONCLUSIONS

In this thesis, the possibilities of using the density functional theory (DFT) to support experimental microscale characterizations are explored. The application of the theory in phase stability problem of Sb_2O_4 identified the theoretical ground state of the antimony tetroxide to be orthorhombic α phase, explaining why in some experiments the β phase show the abnormal stability. The surface instability of the $MgB_2(0001)$ is explored to report a new prediction on the surface reconstruction mode of the partially filled surface of the binary compound, using a variety of DFT-based tools to approach to harness more convincing observations. The interesting modulation of the mechanical strength of Cu-Cr nanoscale multilayers have been investigated, where the low temperature annealing saw decrease of the strength, while high temperature annealing saw increase of the strength instead. The transition state energy of dilute Cr alloy component in Cu matrix is calculated by the nudged elastic band method coupled with DFT, yielding a reasonable rationale to the experimental observation. The latest progress of the synthesis of metallic nano-foam opened create new opportunities to use quantum mechanical tools to solve microscopic problems related to the presence of surface vacancies and potential lattice defects from the heat treatment processes.

In conclusion, the result exemplified a series of microscopic materials science research in which the theoretical approach plays a critical role in understanding the experimentally observed phenomena, predict new phase of materials, and further explained the origin of experimental observations that could be challenging to address otherwise.

REFERENCES

[1] R. M. Martin, *Electronic structure*. Cambridge university press, 2004.

[2] J. Neugebauer and M. Scheffler, "Adsorbate-substrate and adsorbate-adsorbate interactions of na and k adlayers on al (111)," *Phys. Rev. B*, vol. 46, p. 16067, 1992.

[3] A. K. Mishra, A. Roldan, and N. H. de Leeuw, "Cuo surfaces and co2 activation," *J. Phys. Chem. C*, vol. 120, p. 2198, 2016.

[4] R. P. Feynman, "Forces in molecules," *Phys. Rev.*, vol. 56, p. 340, 1939.

[5] H. Hellmann, *Einführung in die quantenchemie*. F. Deuticke, 1937.

[6] D. M. Ceperley and B. J. Alder, "Ground state of the electron gas by a stochastic method," *Phys. Rev. Lett.*, vol. 45, p. 566, 1980.

[7] J. P. Perdew, J. A. Chevary, S. H. Vosko, K. A. Jackson, M. R. Pederson, D. J. Singh, and C. Fiolhais, "Atoms, molecules, solids, and surfaces - applications of the generalized gradient approximation for exchange and correlation," *Phys. Rev. B*, vol. 46, p. 6671, 1992.

[8] ——, "Atoms, molecules, solids, and surfaces - applications of the generalized gradient approximation for exchange and correlation (vol 46, pg 6671, 1992)," *Phys. Rev. B*, vol. 48, p. 4978, 1993.

[9] J. P. Perdew, K. Burke, and M. Ernzerhof, "Generalized gradient approximation made simple," *Phys. Rev. Lett.*, vol. 77, p. 3865, 1996.

[10] J. P. Perdew, M. Ernzerhof, and K. Burke, "Rationale for mixing exact exchange with density functional approximations," *J. Chem. Phys.*, vol. 105, p. 9982, 1996.

[11] J. Heyd, G. E. Scuseria, and M. Ernzerhof, "Hybrid functionals based on a screened coulomb potential," *J. Chem. Phys.*, vol. 118, p. 8207, 2003.

[12] Z. P. Yin, A. Kutepov, and G. Kotliar, "Correlation-enhanced electron-phonon coupling," *Phys. Rev. X*, vol. 3, p. 021011, 2013.

[13] A. Dufrénoy, *Trait de mineralogie par A. Dufrnoy*. Carilian-Goeury et Dalmont, 1845.

[14] J. Amador, E. Gutierrez Puebla, M. A. Monge, I. Rasines, and C. Ruiz Valero, "Diantimony tetraoxides revisited," *Inorg. Chem.*, vol. 27, pp. 1367–1370, 1988.

[15] D. Rogers and A. C. Skapski, *Crystal structure of beta-Sb_2O_4: New polymorph*. Royal Society of Chemistry, Thomas Graham House, 1964, p. 400.

[16] P. S. Gopalakrishnan and H. Manohar, "Topotaxy in the oxidation of valentinite, Sb_2O_3, to cervantite, Sb_2O_4," *Pramana*, vol. 3, pp. 277–285, 1974.

[17] ——, "Topotactic oxidation of valentinite Sb_2O_3 to cervantite Sb_2O_4," *J. Solid State Chem.*, vol. 16, pp. 301–306, 1976.

[18] D. Orosel, P. Balog, H. Liu, J. Qian, and M. Jansen, "Sb_2O_4 at high pressures and high temperatures," *J. Solid State Chem.*, vol. 178, pp. 2602–2607, 2005.

[19] E. T. Keve and A. C. Skapski, "The crystal structure of triclinic β-$BiNbO_4$," *J. Solid State Chem.*, vol. 8, pp. 159–165, 1973.

[20] C.-E. Kim, J. M. Skelton, A. Walsh, and A. Soon, "Solid-state chemistry of glassy antimony oxides," *J. Mater. Chem. C*, vol. 3, pp. 11 349–11 356, 2015.

[21] J. P. Allen, J. J. Carey, A. Walsh, D. O. Scanlon, and G. W. Watson, "Electronic structures of antimony oxides," *J. Phys. Chem. C.*, vol. 117, pp. 14 759–14 769, 2013.

[22] Y. Lee, T. Lee, W. Jang, and A. Soon, "Unraveling the intercalation chemistry of hexagonal tungsten bronze and its optical responses," *Chem. Mater.*, vol. 28, pp. 4528–4535, 2016.

[23] T. Lee, Y. Lee, W. Jang, and A. Soon, "Understanding the advantage of hexagonal WO_3 as an efficient photoanode for solar water splitting: a first-principles perspective," *J. Mater. Chem. A*, vol. 4, pp. 11 498–11 506, 2016.

[24] G. Kresse and J. Furthmüller, "Efficient iterative schemes for ab initio total-energy calculations using a plane-wave basis set," *Phys. Rev. B*, vol. 54, pp. 11 169–11 186, 1996.

[25] ——, "Efficiency of ab-initio total energy calculations for metals and semiconductors using a plane-wave basis set," *Comp. Mater. Sci.*, vol. 6, pp. 15–50, 1996.

[26] P. E. Blöchl, "Projector augmented wave method," *Phys. Rev. B*, vol. 50, pp. 17 953–17 979, 1994.

[27] G. Kresse and D. Joubert, "From ultrasoft pseudopotentials to the projector augmented-wave method," *Phys. Rev. B*, vol. 59, pp. 1758–1775, 1999.

[28] J. Heyd, G. E. Scuseria, and M. Ernzerhof, "Hybrid functionals based on a screened Coulomb potential," *J. Chem. Phys.*, vol. 118, pp. 8207–8215, 2003.

[29] J. Heyd and G. E. Scuseria, "Efficient hybrid density functional calculations in solids," *J. Chem. Phys.*, vol. 121, pp. 1187–1192, 2004.

[30] J. Heyd, G. E. Scuseria, and M. Ernzerhof, "Erratum:Hybrid functionals based on a screened Coulomb potential [J. Chem. Phys. 118, 8207 (2003)]," *J. Chem. Phys.*, vol. 124, p. 219906, 2006.

[31] J. Paier, M. Marsman, K. Hummer, G. Kresse, I. C. Gerber, and J. G. Ángyán, "Screened hybrid density functionals applied to solids," *J. Chem. Phys.*, vol. 124, p. 154709, 2006.

[32] J. P. Perdew, K. Burke, and M. Ernzerhof, "Generalized gradient approximation made simple," *Phys. Rev. Lett.*, vol. 77, pp. 3865–3868, 1996.

[33] L. Schimka, J. Harl, A. Stroppa, A. Grneis, M. Marsman, F. Mittendorfer, and G. Kresse, "Accurate surface and adsorption energies from many-body perturbation theory," *Nat. Mater.*, vol. 9, pp. 741–744, 2010.

[34] J. Harl and G. Kresse, "Accurate bulk properties from approximate many-body techniques," *Phys. Rev. Lett.*, vol. 103, p. 056401, 2009.

[35] S. Grimme, "Semiempirical GGA-type density functional constructed with a long-range dispersion correction," *J. Comput. Chem.*, vol. 27, pp. 1787–1799, 2006.

[36] J. P. Perdew, A. Ruzsinszky, G. I. Csonka, O. A. Vydrov, G. E. Scuseria, L. A. Constantin, X. Zhou, and K. Burke, "Restoring the density-gradient expansion for exchange in solids and surfaces," *Phys. Rev. Lett.*, vol. 100, p. 136406, 2008.

[37] W. Kohn and L. J. Sham, "Self-consistent equations including exchange and correlation effects," *Phys. Rev.*, vol. 140, pp. A1133–A1138, 1965.

[38] H. J. Monkhorst and J. D. Pack, "Special points for Brillouin-zone integrations," *Phys. Rev. B*, vol. 13, pp. 5188–5192, 1976.

[39] S. Baroni, P. Giannozzi, and A. Testa, "Greens function approach to linear response in solids," *Phys. Rev. Lett.*, vol. 58, pp. 1861–1864, 1987.

[40] X. Gonze, "Perturbation expansion of variational principles at arbitrary order," *Phys. Rev. A*, vol. 52, pp. 1086–1095, 1995.

[41] ——, "Adiabatic density-functional perturbation theory," *Phys. Rev. A*, vol. 52, pp. 1096–1114, 1995.

[42] P. Jacobaeus, J. U. Madsen, F. Kragh, and R. M. J. Cotterill, "Triplet correlation in metallic glasses a field-ion microscopy study," *Philos. Mag. B*, vol. 41, pp. 11–20, 1980.

[43] B. Silvi and A. Savin, "Classification of chemical bonds based on topological analysis of electron localization functions," *Nature*, vol. 371, pp. 683–686, 1994.

[44] G. Thornton, "A neutron diffraction study of α-Sb_2O_4," *Acta. Crystallogr. Sect. B-Struct. Sci.*, vol. 33, p. 1271, 1977.

[45] A. Palenzona, "Clinocervantite,Sb_2O_4, the natural monoclinic polymorph of cervantite from the Cetine mine, Siena, Italy," *Eur. J. Mineral.*, vol. 11, p. 95, 1999.

[46] J. K. Burdett, "Use of the Jahn-Teller theorem in inorganic chemistry," *Inorg. Chem.*, vol. 20, pp. 1959–1962, 1981.

[47] J. J. Carey, J. P. Allen, D. O. Scanlon, and G. W. Watson, "The electronic structure of the antimony chalcogenide series," *J. Solid State Chem.*, vol. 213, pp. 116–125, 2014.

[48] F. Bouquet, R. A. Fisher, N. E. Phillips, D. G. Hinks, and J. D. Jorgensen, "Specific heat of mg 11 b 2," *Phys. Rev. Lett.*, vol. 87, p. 047001, 2001.

[49] Y. Wang, T. Plackowski, and A. Junod, "Specific heat in the superconducting and normal state (2300 k, 016 t), and magnetic susceptibility of the 38 k superconductor mgb 2," *Physica C Supercond.*, vol. 355, p. 179, 2001.

[50] B. F. Decker and J. S. Kasper, "The crystal structure of a simple rhombohedral form of boron," *Acta Crystallogr.*, vol. 12, p. 503, 1959.

[51] V. Moshchalkov, M. Menghini, T. Nishio, Q. H. Chen, A. V. Silhanek, V. H. Dao, L. F. Chibotaru, N. D. Zhigadlo, and J. Karpinski, "Type-1.5 superconductivity," *Phys. Rev. Lett.*, vol. 102, p. 117001, 2009.

[52] M. Xu, Y. Takano, T. Hatano, T. Kimura, and D. Fujita, "Auger electron spectroscopy study of mgb 2 surface," *Appl. Surf. Sci.*, vol. 205, p. 225, 2003.

[53] G. Karapetrov, M. Iavarone, W. K. Kwok, G. W. Crabtree, and D. G. Hinks, "Scanning tunneling spectroscopy in mgb 2," *Phys. Rev. Lett.*, vol. 86, p. 4374, 2001.

[54] G. Rubio-Bollinger, H. Suderow, and S. Vieira, "Tunneling spectroscopy in small grains of superconducting mgb 2," *Phys. Rev. Lett.*, vol. 86, p. 5582, 2001.

[55] P. Seneor, C. T. Chen, N. C. Yeh, R. P. Vasquez, L. D. Bell, C. U. Jung, M.-S. Park, H.-J. Kim, W. N. Kang, and S.-I. Lee, "Spectroscopic evidence for anisotropic s-wave pairing symmetry in mgb 2," *Phys. Rev. B*, vol. 65, p. 012505, 2001.

[56] H. Schmidt, J. F. Zasadzinski, K. E. Gray, and D. G. Hinks, "Energy gap from tunneling and metallic contacts onto mgb 2," *Phys. Rev. B*, vol. 63, p. 220504, 2001.

[57] A. Sharoni, I. Felner, and O. Millo, "Tunneling spectroscopy and magnetization measurements of the superconducting properties of mgb 2," *Phys. Rev. B*, vol. 63, p. 220508, 2001.

[58] R. K. Singh, Y. Shen, R. Gandikota, J. M. Rowell, and N. Newman, "Effect of stoichiometry on oxygen incorporation in mgb2 thin films," *Supercond. Sci. Technol.*, vol. 21, p. 015018, 2007.

[59] R. F. Klie, J. C. Idrobo, N. D. Browning, K. A. Regan, N. S. Rogado, and R. J. Cava, "Direct observation of nanometer-scale mg-and b-oxide phases at grain boundaries in mgb2," *Appl. Phys. Lett.*, vol. 79, p. 1837, 2001.

[60] W. Chen, W. Liu, C. Chen, R. Wang, and Q. Feng, "Single-crystal mgb2 hexagonal microprisms viahybrid physical-chemical vapor deposition," *CrystEngComm*, vol. 13, p. 3959, 2011.

[61] Y. Wang, K. Michel, Y. Zhang, and C. Wolverton, "Thermodynamic stability of transition metals on the mg-terminated mgb 2 (0001) surface and their effects on hydrogen dissociation and diffusion," *Phys. Rev. B*, vol. 91, p. 155431, 2015.

[62] T. A. Callcott, L. Lin, G. T. Woods, G. P. Zhang, J. R. Thompson, M. Paranthaman, and D. L. Ederer, "Soft-x-ray spectroscopy measurements of the p-like density of states of b in mgb 2 and evidence for surface boron oxides on exposed surfaces," *Phys. Rev. B*, vol. 64, p. 132504, 2001.

[63] B. H. Moeckly and W. S. Ruby, "Growth of high-quality large-area mgb2 thin films by reactive evaporation," *Supercond. Sci. Technol.*, vol. 19, p. L21, 2006.

[64] X. L. Chen, Q. Y. Tu, M. He, L. Dai, and L. Wu, "The bond ionicity of mb2 (m= mg, ti, v, cr, mn, zr, hf, ta, al and y)," *J. Phys.: Condens. Matter*, vol. 13, p. L723, 2001.

[65] A. Y. Liu, I. I. Mazin, and J. Kortus, "Beyond eliashberg superconductivity in mgb 2," *Phys. Rev. Lett.*, vol. 87, p. 087005, 2001.

[66] H. J. Choi, D. Roundy, H. Sun, M. L. Cohen, and S. G. Louie, "The origin of the anomalous superconducting properties of mgb2," *Nature*, vol. 418, p. 758, 2002.

[67] W. Kohn and L. J. Sham, "Self-consistent equations including exchange and correlation effects," *Phys. Rev.*, vol. 140, p. A1133, 1965.

[68] G. Kresse and J. Furthmüller, "Efficient iterative schemes for ab initio total-energy calculations using a plane-wave basis set," *Phys. Rev. B*, vol. 54, p. 11169, 1996.

[69] ——, "Efficiency of ab-initio total energy calculations for metals and semiconductors using a plane-wave basis set," *Comp. Mater. Sci.*, vol. 6, p. 15, 1996.

[70] P. E. Blöchl, "Projector augmented-wave method," *Phys. Rev. B*, vol. 50, p. 17953, 1994.

[71] G. Kresse and D. Joubert, "From ultrasoft pseudopotentials to the projector augmented-wave method," *Phys. Rev. B*, vol. 59, p. 1758, 1999.

[72] J. P. Perdew, K. Burke, and M. Ernzerhof, "Generalized gradient approximation made simple," *Phys. Rev. Lett.*, vol. 77, p. 3865, 1996.

[73] J. P. Perdew, A. Ruzsinszky, G. I. Csonka, O. A. Vydrov, G. E. Scuseria, L. A. Constantin, X. Zhou, and K. Burke, "Restoring the density-gradient expansion for exchange in solids and surfaces," *Phys. Rev. Lett.*, vol. 100, p. 136406, 2008.

[74] B. Hammer, L. B. Hansen, and J. K. Nørskov, "Improved adsorption energetics within density-functional theory using revised perdew-burke-ernzerhof functionals," *Phys. Rev. B*, vol. 59, p. 7413, 1999.

[75] J. Heyd, G. E. Scuseria, and M. Ernzerhof, "Hybrid functionals based on a screened coulomb potential," *J. Chem. Phys.*, vol. 118, p. 8207, 2003.

[76] J. Heyd and G. E. Scuseria, "Efficient hybrid density functional calculations in solids," *J. Chem. Phys.*, vol. 121, p. 1187, 2004.

[77] J. Heyd, G. E. Scuseria, and M. Ernzerhof, "Erratum:hybrid functionals based on a screened coulomb potential[j. chem. phys. 118, 8207 (2003)]," *J. Chem. Phys.*, vol. 124, p. 219906, 2006.

[78] J. Paier, M. Marsman, K. Hummer, G. Kresse, I. C. Gerber, and J. G. ngyn, "Screened hybrid density functionals applied to solids," *J. Chem. Phys.*, vol. 124, p. 154709, 2006.

[79] S. Grimme, J. Antony, S. Ehrlich, and H. Krieg, "A consistent and accurate ab initio parametrization of density functional dispersion correction (dft-d) for the 94 elements h-pu," *J. Chem. Phys.*, vol. 132, p. 154104, 2010.

[80] H. Lun-hua, H. Gui-qing, Z. Pan-lin, and Y. Qi-wei, "Structure analysis of new superconductor mgb2," *Chin. Phys. Soc.*, vol. 10, p. 343, 2001.

[81] S. Klüpfel, P. Klüpfel, and H. Jónsson, "The effect of the perdew-zunger self-interaction correction to density functionals on the energetics of small molecules," *J. Chem. Phys.*, vol. 137, p. 124102, 2012.

[82] G. Kresse and J. Hafner, "Ab-initio molecular-dynamics simulation of the liquid-metal amorphous-semiconductor transition in germanium," *Phys. Rev. B*, vol. 49, p. 14251, 1994.

[83] S. Nosé, "A unified formulation of the constant temperature molecular dynamics methods," *J. Chem. Phys.*, vol. 81, p. 511, 1984.

[84] A. K. Geim and I. V. Grigorieva, "Van der waals heterostructures," *Nature*, vol. 499, p. 419, 2013.

[85] Z. Li, J. Yang, J. G. Hou, and Q. Zhu, "First-principles study of mgb 2 0001 surfaces," *Phys. Rev. B*, vol. 65, p. 100507, 2002.

[86] J. D. Jorgensen, D. G. Hinks, and S. Short, "Lattice properties of mgb 2 versus temperature and pressure," *Phys. Rev. B*, vol. 63, p. 224522, 2001.

[87] W. Tang, E. Sanville, and G. Henkelman, "A grid-based bader analysis algorithm without lattice bias," *J. Phys-Condens. Mat.*, vol. 21, p. 084204, 2009.

[88] R. F. W. Bader, *Atoms in Molecules*. Clarendon Press, 1990.

[89] D. M. Collins, "Electron density images from imperfect data by iterative entropy maximization," *Nature*, vol. 298, p. 49, 1982.

[90] E. Nishibori, M. Takata, M. Sakata, H. Tanaka, T. Muranaka, and J. Akimitsu, "Bonding nature in mgb2," *J. Phys. Soc. Jpn.*, vol. 70, p. 2252, 2001.

[91] J. M. An and W. E. Pickett, "Superconductivity of mgb 2," *Phys. Rev. Lett.*, vol. 86, p. 4366, 2001.

[92] J. A. Silva-Guillén, Y. Noat, T. Cren, W. Sacks, E. Canadell, and P. Ordejón, "Tunneling and electronic structure of the two-gap superconductor mgb 2," *Phys. Rev. B*, vol. 92, p. 064514, 2015.

[93] K. D. Belashchenko, M. van Schilfgaarde, and V. P. Antropov, "Coexistence of covalent and metallic bonding in the boron intercalation superconductor mgb 2," *Phys. Rev. B*, vol. 64, p. 092503, 2001.

[94] K. A. Yates, Z. Lockman, A. Kursumovic, G. Burnell, N. A. Stelmashenko, J. L. MacManus Driscoll, and M. G. Blamire, "The effect of oxygenation on the superconducting properties of mg b 2 thin films," *Appl. Phys. Lett.*, vol. 86, p. 022502, 2005.

[95] T. Ogitsu, F. Gygi, J. Reed, M. Udagawa, Y. Motome, E. Schwegler, and G. Galli, "Geometrical frustration in an elemental solid," *Phys. Rev. B*, vol. 81, p. 020102, 2010.

[96] T. Ogitsu, E. Schwegler, and G. Galli, "-rhombohedral boron," *Chem. Rev.*, vol. 113, p. 3425, 2013.

[97] K. Momma and F. Izumi, "Vesta 3 for three-dimensional visualization of crystal, volumetric and morphology data," *J. Appl. Crystallogr.*, vol. 44, p. 1272, 2011.

[98] T. Ogitsu, F. Gygi, J. Reed, Y. Motome, E. Schwegler, and G. Galli, "Imperfect crystal and unusual semiconductor," *J. Am. Chem. Soc.*, vol. 131, p. 1903, 2009.

[99] M. Widom and M. Mihalkovič, "Symmetry-broken crystal structure of elemental boron at low temperature," *Phys. Rev. B*, vol. 77, p. 064113, 2008.

[100] F. Bobba, D. Roditchev, R. Lamy, E. M. Choi, H. J. Kim, W. N. Kang, V. Ferrando, C. Ferdeghini, F. Giubileo, and W. Sacks, "Quasiparticle state density on the surface of superconducting thin films of mgb2," *Supercond. Sci. Technol.*, vol. 16, p. 167, 2002.

[101] Y. Zhang, Z. Lin, Q. Dai, D. Li, Y. Wang, Y. Zhang, Y. Wang, and Q. Feng, "Ultrathin mgb2 films fabricated on al2o3 substrate by hybrid physicalchemical vapor deposition with high tc and jc," *Supercond. Sci. Technol.*, vol. 24, p. 015013, 2010.

[102] V. Despoja, D. J. Mowbray, and V. M. Silkin, "Tuning mgb 2 (0001) surface states through surface termination," *Phys. Rev. B*, vol. 84, p. 104514, 2011.

[103] V. M. Silkin, E. V. Chulkov, and P. M. Echenique, "Surface and image-potential states on mgb_2(0001) surfaces," *Phys. Rev. B*, vol. 64, p. 172512, 2001.

[104] G. Profeta, A. Continenza, F. Bernardini, and S. Massidda, "Electronic and dynamical properties of the mgb_2 surface," *Phys. Rev. B*, vol. 66, p. 184517, 2002.

[105] V. D. P. Servedio, S. L. Drechsler, and T. Mishonov, "Surface states and their possible role in the superconductivity of mgb_2," *Phys. Rev. B*, vol. 66, p. 140502, 2002.

[106] J. W. Martin, *Precipitation hardening: theory and applications*. Butterworth-Heinemann, 2012.

[107] P. C. Wo, N. Abdolrahim, Y. F. Zhu, I. N. Mastorakos, D. F. Bahr, and H. M. Zbib, "Precipitation strengthening in nanocomposite cr/cucr multilayer films," *Philos. Mag.*, vol. 95, p. 1780, 2015.

[108] H. Okamoto, "Cr-cu(chromium-copper)," *J. Phase Equilibria(USA)*, vol. 22, p. 691, 2001.

[109] A. Misra, M. Verdier, Y. C. Lu, H. Kung, T. E. Mitchell, M. Nastasi, and J. D. Embury, "Structure and mechanical properties of cu-x (x nb, cr, ni) nanolayered composites," *Scripta Mater.*, vol. 39, p. 555, 1998.

[110] R. G. Hoagland, J. P. Hirth, and A. Misra, "On the role of weak interfaces in blocking slip in nanoscale layered composites," *Philos. Mag.*, vol. 86, p. 3537, 2006.

[111] C. A. Volkert, A. Donohue, and F. Spaepen, "Effect of sample size on deformation in amorphous metals," *Jpn. J. Appl. Phys.*, vol. 103, p. 3539, 2008.

[112] Z. Yang and J. Wang, "Coupled annealing temperature and layer thickness effect on strengthening mechanisms of ti/ni multilayer thin films," *J. Mech. Phys. Solids*, vol. 88, p. 72, 2016.

[113] R. L. Schoeppner, N. Abdolrahim, I. Salehinia, H. M. Zbib, and D. F. Bahr, "Elevated temperature dependence of hardness in tri-metallic nano-scale metallic multilayer systems," *Thin Solid Films*, vol. 571,, p. 247, 2014.

[114] W. Kohn and L. J. Sham, "Self-consistent equations including exchange and correlation effects," *Phys. Rev.*, vol. 140, p. A1133, 1965.

[115] G. Kresse and J. Furthmüller, "Efficient iterative schemes for ab initio total-energy calculations using a plane-wave basis set," *Phys. Rev. B*, vol. 54, p. 11169, 1996.

[116] ——, "Efficiency of ab-initio total energy calculations for metals and semiconductors using a plane-wave basis set," *Comp. Mater. Sci.*, vol. 6, p. 15, 1996.

[117] P. E. Blöchl, "Projector augmented-wave method," *Phys. Rev. B*, vol. 50, p. 17953, 1994.

[118] G. Kresse and D. Joubert, "From ultrasoft pseudopotentials to the projector augmented-wave method," *Phys. Rev. B*, vol. 59, p. 1758, 1999.

[119] T. P. Harzer, S. Djaziri, R. Raghavan, and G. Dehm, "Nanostructure and mechanical behavior of metastable cucr thin films grown by molecular beam epitaxy," *Acta. Mater.*, vol. 83, p. 318, 2015.

[120] G. Henkelman, B. P. Uberuaga, and H. Jónsson, "A climbing image nudged elastic band method for finding saddle points and minimum energy paths," *J. Chem. Phys.*, vol. 113, p. 9901, 2000.

[121] M. R. Maughan, H. M. Zbib, and D. F. Bahr, "Variation in the nanoindentation hardness of platinum," *J. Mater. Res.*, vol. 28, p. 2819, 2013.

[122] W. Tang, E. Sanville, and G. Henkelman, "A grid-based bader analysis algorithm without lattice bias," *J. Phys-Condens. Mat.*, vol. 21, p. 084204, 2009.

[123] C. L. Fu, "Origin of ordering in b2-type transition-metal aluminides: comparative study of the defect properties of pdal, nial, and feal," *Phys. Rev. B*, vol. 52, p. 3151, 1995.

[124] C. H. Liebscher, C. Freysoldt, T. Dennenwaldt, T. P. Harzer, and G. Dehm, "Electronic structure of metastable bcc cucr alloy thin films: Comparison of electron energy-loss spectroscopy and first-principles calculations," *Ultramicroscopy*, vol. 178, p. 96, 2017.

[125] D. E. Jiang and E. A. Carter, "Carbon dissolution and diffusion in ferrite and austenite from first principles," *Phys. Rev. B*, vol. 67, p. 214103, 2003.

[126] R. Raghavan, J. M. Wheeler, T. P. Harzer, V. Chawla, S. Djaziri, K. Thomas, B. Philippi, C. Kirchlechner, B. N. Jaya, J. Wehrs, J. Michler, and G. Dehm, "Transition from shear to stress-assisted diffusion of copperchromium nanolayered thin films at elevated temperatures," *Acta. Mater.*, vol. 100, p. 73, 2015.

[127] M. Hakamada and M. Mabuchi, "Fabrication, microstructure, and properties of nanoporous pd, ni, and their alloys by dealloying," *Crit. Rev. Solid State Mater. Sci.*, vol. 38, p. 262, 2013.

[128] I. McCue, E. Benn, B. Gaskey, and J. Erlebacher, "Dealloying and dealloyed materials," *Ann. Rev. Mater. Res.*, vol. 46, p. 263, 2016.

[129] A. Greiner and J. H. Wendorff, "Electrospinning: a fascinating method for the preparation of ultrathin fibers," *Angew. Chem. Int. Ed.*, vol. 46, p. 5670, 2007.

[130] H. Wu, L. Hu, M. W. Rowell, D. Kong, J. J. Cha, J. R. McDonough, J. Zhu, Y. Yang, M. D. McGehee, and Y. Cui, "Electrospun metal nanofiber webs as high-performance transparent electrode," *Nano Lett.*, vol. 10, p. 4242, 2010.

[131] D. F. Bahr and D. J. Morris, *Nanoindentation: Localized probes of mechanical behavior of materials*. Springer, 2008.

[132] W. C. Oliver and G. M. Pharr, "Measurement of hardness and elastic modulus by instrumented indentation: Advances in understanding and refinements to methodology," *J. Mater. Res.*, vol. 19, p. 3, 2004.

[133] M. D. Judd, B. A. Plunkett, and M. I. Pope, "The thermal decomposition of calcium, sodium, silver and copper (ii) acetates," *J. Therm. Anal. Calorim*, vol. 6, p. 555, 1974.

[134] Z. Lin, D. Han, and S. Li, "Study on thermal decomposition of copper (ii) acetate monohydrate in air," *J. Therm. Anal. Calorim*, vol. 107, p. 471, 2012.

[135] J. Liu, M. J. Chang, and H. L. Du, "Facile preparation of cross-linked porous poly(vinyl alcohol) nanofibers by electrospinning," *Mater. Lett.*, vol. 183, p. 318, 2016.

[136] T.-H. Fang and W.-J. Chang, "Nanomechanical properties of copper thin films on different substrates using the nanoindentation technique," *Microelectron. Eng.*, vol. 65, p. 231, 2003.

[137] J. Biener, A. M. Hodge, J. R. Hayes, C. A. Volkert, L. A. Zepeda-Ruiz, A. V. Hamza, and F. F. Abraham, "Size effects on the mechanical behavior of nanoporous au," *Nano. Lett.*, vol. 6, p. 2379, 2006.

[138] M. F. Ashby and L. J. Gibson, *Cellular solids: structure and properties*. Cambridge New York, 1997.

[139] A. P. Roberts and E. J. Garboczi, "Elastic properties of model random three-dimensional open-cell solids," *J. Mech. Phys. Solids*, vol. 50, p. 33, 2002.

[140] C. E. Kim, R. M. Rahimi, N. Hightower, I. Mastorakos, and D. F. Bahr, "Synthesis, microstructure, and mechanical properties of polycrystalline cu nanofoam," *MRS Adv.*, vol. 3, p. 466, 2018.

[141] B. C. Tappan, S. A. Steiner, and E. P. Luther, "Nanoporous metal foams," *Angew. Chem. Int. Ed.*, vol. 49, p. 4544, 2010.

[142] J. Erlebacher, "An atomistic description of dealloying porosity evolution, the critical potential, and rate-limiting behavior," *J. Electrochem. Soc.*, vol. 151, p. C614, 2004.

[143] G. W. Nyce, J. R. Hayes, A. V. Hamza, and J. H. Satcher, "Synthesis and characterization of hierarchical porous gold materials," *Chem. Mater.*, vol. 19, p. 344, 2007.

[144] J. L. Mohanan, I. U. Arachchige, and S. L. Brock, "Porous semiconductor chalcogenide aerogels," *Science*, vol. 307, p. 397, 2005.

[145] N. Leventis, N. Chandrasekaran, A. G. Sadekar, C. Sotiriou-Leventis, and H. Lu, "One-pot synthesis of interpenetrating inorganic/organic networks of cuo/resorcinol-formaldehyde aerogels," *J. Am. Chem. Soc.*, vol. 131, p. 4576, 2009.

[146] B. C. Tappan, M. H. Huynh, M. A. Hiskey, D. E. Chavez, E. P. Luther, J. T. Mang, and S. F. Son, "Ultralow-density nanostructured metal foams," *J. Am. Chem. Soc.*, vol. 128, p. 6589, 2006.

[147] Y. H. Tan, J. A. Davis, K. Fujikawa, N. V. Ganesh, A. V. Demchenko, and K. J. Stine, "Surface area and pore size characteristics of nanoporous gold subjected to thermal, mechanical, or surface modification studied using gas adsorption isotherms, cyclic voltammetry, thermogravimetric analysis, and scanning electron microscopy," *J. Mater. Chem.*, vol. 22, p. 6733, 2012.

[148] L. Chen, J. Yu, T. Fujita, and M. Chen, "Nanoporous copper with tunable nanoporosity for sers applications," *Adv. Funct. Mater.*, vol. 19, p. 1221, 2009.

[149] J. Freel, W. J. M. Pieters, and R. B. Anderson, "The structure of raney nickel," *J. Catal.*, vol. 14, p. 247, 1969.

[150] J. Erlebacher, M. J. Aziz, A. Karma, N. Dimitrov, and K. Sieradzki, "Evolution of nanoporosity in dealloying," *Nature*, vol. 410, p. 450, 2001.

[151] P. J. Spencer and W. Slough, "Applied and experimental chemical thermodynamics at high temperatures," *High Temp High Press.*, vol. 2, p. 123, 1970.

[152] A. Kuper, H. Letaw, L. Slifkin, E. Sonder, and C. T. Tomizuka, "Self-diffusion in copper," *Phys. Rev.*, vol. 96, p. 1224, 1954.

[153] J. R. Macewan, J. U. Macewan, and L. Yaffe, "Self-diffusion in polycrystalline nickel," *Can. J. Chem.*, vol. 37, p. 1623, 1959.

[154] H.-Y. Hsiao, C.-M. Liu, H.-w. Lin, T.-C. Liu, C.-L. Lu, Y.-S. Huang, C. Chen, and K. N. Tu, "Unidirectional growth of microbumps on (111)-oriented and nanotwinned copper," *Science*, vol. 336, p. 1007, 2012.

[155] I. D. Choi, D. K. Matlock, and D. L. Olson, "An analysis of diffusion-induced porosity in cu-ni laminate composites," *Mater. Sci. Eng. A Struct. Mater.*, vol. 124, p. L15, 1990.

[156] J. C. De Jesus, I. Gonzlez, A. Quevedo, and T. Puerta, "Thermal decomposition of nickel acetate tetrahydrate," *J. Mol. Catal. A Chem.*, vol. 228, p. 283, 2005.

[157] H. M. Otte, "Lattice parameter determinations with an xray spectrogoniometer by the debyescherrer method and the effect of specimen condition," *Jpn. J. Appl. Phys.*, vol. 32, p. 1536, 1961.

[158] H. E. Swanson, E. Tatge, and R. K. Fuyat, *Standard X-ray diffraction powder patterns*. US Government Printing Office, 1953.

[159] F. W. Von Batchelder and R. F. Raeuchle, "Re-examination of the symmetries of iron and nickel by the powder method," *Acta Crystallogr.*, vol. 7, p. 464, 1954.

VITA

Changeun Kim (C.-E. Kim)

EDUCATION

Purdue University (West lafayette, USA) Mater. Sci. Eng. Ph.D. (Aug 2018)
Yonsei University (Seoul, South Korea) Mater. Sci. Eng. M.S. (Aug 2015)
Yonsei University (Seoul, South Korea) Mater. Sci. Eng. B.S. (Mar 2013)

EMPLOYMENT

Research assistant Purdue University 08/21/2015 - 07/31/2018
Research internship Lawrence Livermore Nat'l Lab. 06/05/2017 - 08/11/2017
Research internship Lawrence Livermore Nat'l Lab. 06/06/2016 - 08/12/2016
Teaching assistant Purdue University 08/26/2016 - 12/23/2016
Teaching assistant Yonsei University 09/01/2013 - 12/23/2013
Teaching assistant Yonsei University 09/01/2014 - 12/23/2014
Research internship Korea Inst. Sci. Tech. 09/01/2013 - 08/10/2015
Research assistant Yonsei University 03/01/2013 - 06/30/2015
Undergraduate research intern Yonsei University 04/10/2010 - 02/28/2013

PUBLICATIONS

C.-E. Kim, R.M. Rahimi, N. Hightower, I. Mastorakos, and D.F. Bahr, Synthesis, microstructure, and mechanical properties of polycrystalline Cu nano-foam, *MRS Adv.*, **3**, 469 (2018)

C.-E. Kim, K.G. Ray, D.F. Bahr, and V. Lordi, Electronic structure and surface properties of MgB2(0001) upon oxygen adsorption, *Phys. Rev. B*, **97**, 195416 (2018)

C.-E. Kim, R.M. Rahimi, T.L. Maxwell, T.J. Balk, and D.F. Bahr, Age-hardening in a two component immiscible nanolaminate metal system, *Scripta Mater.*, **136**, 33 (2017)

C.-E. Kim, S.-H. Yoo, D.F. Bahr, C. Stampfl, and A. Soon, Uncovering the Thermo-Kinetic Origins of Phase Ordering in Mixed-Valence Antimony Tetroxide by First-Principles Modeling, *Inorg. Chem.*, **56**, 6545 (2017)

A. Yermembetova, R.M. Rahimi, **C.-E. Kim**, J.L. Skinner, J.M. Andriolo, J.P. Murphy, and D.F. Bahr, Nanomechanics and Testing of Core-Shell Composite Ligaments for High Strength, Light Weight Foams, *MRS Adv.*, **2**, 3577 (2017)

C.-E. Kim, A. Soon, and C. Stampfl, Unraveling the origins of conduction band valley degeneracies in Mg 2 Si 1- x Sn x thermoelectrics, *Phys. Chem. Chem. Phys.*, **18**, 939 (2016)

J.M. Skelton, L.A. Burton, S.C. Parker, A. Walsh, **C.-E. Kim**, A. Soon, J. Buckeridge, A.A. Sokol, C.R.A. Catlow, and A. Togo, Anharmonicity in the high-temperature Cmcm phase of SnSe: soft modes and three-phonon interactions, *Phys. Rev. Lett.*, **117**, 075502 (2016)

C.-E. Kim, D.-H. Lim, J.H. Jang, H.J. Kim, S.P. Yoon, J. Han, S.W. Nam, S.-A. Hong, A. Soon, and H.C. Ham, Effect of gold subsurface layer on the surface activity and segregation in Pt/Au/Pt3M (where M= 3 d transition metals) alloy catalyst from first-principles, *J. Chem. Phys.*, **142**, 034707 (2015)

C.-E. Kim, Y.-J. Tak, K.T. Butler, A. Walsh, and A. Soon, Lattice-mismatched heteroepitaxy of IV-VI thin films on PbTe (001): An ab initio study, *Phys. Rev. B*, **91**, 085307 (2015)

J. Kwak, **C.-E. Kim**, Y. Min, J.-H. Lee, A. Soon, and U. Jeong, The effect of Se doping on the growth of Te nanorods, *CrystEngComm*, **17**, 5734 (2015)

C.-E. Kim, J.M. Skelton, A. Walsh, and A. Soon, Solid-state chemistry of glassy antimony oxides, *J. Mater. Chem.*, **3**, 11349 (2015)

H. Yang, **C.-E. Kim**, A. Giri, A. Soon, and U. Jeong, Synthesis of surfactant-free SnS nanoplates in an aqueous solution, *RSC Adv.*, **5**, 94796 (2015)

K. Lim, C. Kim, Y. Yun, W. Kim, A. Soon, and D. Kim, Remarkably stable amorphous metal oxide grown on Zr-Cu-Be metallic glass, *Sci. Rep.*, **5**, 18196 (2015)

Y. Min, G.D. Moon, **C.-E. Kim**, J.-H. Lee, H. Yang, A. Soon, and U. Jeong, Solution-based synthesis of anisotropic metal chalcogenide nanocrystals and their applications, *J. Mater. Chem.*, **2**, 6222 (2014)

N.A. Richter, **C.-E. Kim**, C. Stampfl, and A. Soon, Re-visiting the O/Cu (111) system–when metastable surface oxides could become an issue!, *Phys. Chem. Chem. Phys.*, **16**, 26735 (2014)

R. Zhang, **C.-E. Kim**, B.-D. Yu, C. Stampfl, and A. Soon, Mitigation of CO poisoning on functionalized Pt–TiN surfaces, *Phys. Chem. Chem. Phys.*, **15**, 19450 (2013)

R.-Q. Zhang, **C.-E. Kim**, B. Delley, C. Stampfl, and A. Soon, A first-principles study of ultrathin nanofilms of MgO-supported TiN, *Phys. Chem. Chem. Phys.*, **14**, 2462 (2012)

CONFERENCE

ASM International Indianapolis chapter, West Lafayette IN, USA, (2017)
Synthesis, microstructure, and mechanical properties of polycrystalline Cu nano-foam
C.-E. Kim, R.M. Rahimi, N. Hightower, I. Mastorakos, and D.F. Bahr

Materials Research Society (MRS) Fall meeting, Boston MA, USA, (2017)
Mechanical properties of polycrystalline Cu nano-foams: extending experimental observations to computer modeling
C.-E. Kim and R.M. Rahimi, N. Hightower, I. Mastorakos, and D.F. Bahr

Materials Research Society (MRS) Fall meeting, Boston MA, USA, (2016)
Determination of strengthening effect interactions in multilayer thin films using nanoindentation and molecular dynamics
C.-E. Kim, T.M. Maxwell, T.J. Balk, and D.F. Bahr

Materials Research Society (MRS) Fall meeting, Boston MA, USA, (2013)
A first principles study on the crystalline and amorphous phases of antimony oxide
C.-E. Kim and A. Soon

Korean Institute of Metals and Materials (KIMS) Fall Meeting, Gwang-Ju, Korea, (2013)
A first-principles study on SbxOy crystalline and amorphous phase
C.-E. Kim , S.-H. Yoo, and A. Soon

Korean Materials Research Society (MRS) Spring Meeting, Yeosu, Korea, (2013)
A first-principles study on SbxOy polymorphs
C.-E. Kim and A. Soon

Korean Institute of Metals and Materials (KIMS) Fall Meeting, Changwon, Korea, (2010)
Ultrathin nanofilms of MgO-supported TiN: a first-principles investigation
C.-E. Kim, B. Delley, C. Stampfl, and A. Soon

Asian Workshop on First-Principles Electronic Structure Calculations, Pohang, Korea, (2010)
Ultrathin nanofilms of MgO-supported TiN: a first-principles investigation
C.-E. Kim, B. Delley, C. Stampfl, and A. Soon

WORKSHOP

Patent writing workshop series, IP-academy, Seoul, South Korea, (2011)
School on Numerical Methods for Materials Science Related to Renewable Energy Applications, ICTP, Trieste, Italy, (2012)
Hybrid CPU-GPU parallel computing workshop, KISTI, Daejeon, South Korea, (2013)
Heterogeneous parallel computing winter school, KISTI, Yong-in, South Korea, (2013)
Single crystal x-ray diffraction analysis, Bruker, Seoul, South Korea, (2014)
Computational Chemistry and Materials Science (CCMS) Summer Institute, Lawrence Livermore Nat'l Lab., Livermore CA, USA, (2016,2017)